NANYANG
TECHNOLOGICAL
UNIVERSITY
SINGAPORE

SPINEL OXIDE FOR OXYGEN ELECTROCATALYSIS

ZHOU YE

SCHOOL OF MATERIALS SCIENCE AND ENGINEERING

2019

SPINEL OXIDE FOR OXYGEN ELECTROCATALYSIS

ZHOU YE

SCHOOL OF MATERIALS SCIENCE AND ENGINEERING

A thesis submitted to the Nanyang Technological University
in partial fulfillment of the requirement for the degree of
Doctor of Philosophy

2019

Statement of Originality

I hereby certify that the work embodied in this thesis is the result of original research and has not been submitted for a higher degree to any other University or Institution.

Input Date Here

. . . 21-Jan-2019. . . . .
Date

Input Signature Here

. . . . ZHOU YE . . . .
Input Name Here

Supervisor Declaration Statement

I have reviewed the content and presentation style of this thesis and declare it is free of plagiarism and of sufficient grammatical clarity to be examined. To the best of my knowledge, the research and writing are those of the candidate except as acknowledged in the Author Attribution Statement. I confirm that the investigations were conducted in accord with the ethics policies and integrity standards of Nanyang Technological University and that the research data are presented honestly and without prejudice.

Input Date Here

. . . 21-Jan-2019. . . .
Date

Input Supervisor Signature

. . . Assoc Prof Jason Xu Zhichuan. . .
Input Supervisor Name Here

Authorship Attribution Statement

This thesis contains material from papers published in the following peer-reviewed journals where I was the first author.

Chapter 5 is published as Y. Zhou, S. Sun, S. Xi, Y. Duan, T. Sritharan, Y. Du, Z. J. Xu. Superexchange effects on oxygen reduction activity of edge-sharing [$Co_xMn_{1-x}O_6$] octahedra in spinel oxide. *Adv. Mater*. **30**, 1705407 (2018). DOI: 10.1002/adma.201705407.

The contributions of the co-authors are as follows:

- Assoc. Prof Z. J. Xu，Dr S. Sun and I conceived the idea and Assoc. Prof Z. J. Xu supervised the entire project.
- I prepared the manuscript drafts. Assoc. Prof Z. J. Xu discussed and analyzed the measured data with me. Assoc. Prof Z. J. Xu revised the manuscript and provided valuable suggestions which helped in polishing the manuscript further.
- I performed all the electrochemical measurements and analyzed the data.
- S. Sun synthesized the materials, collected the X-ray diffraction patterns and Brunauer-Emmett-Teller data in the Facility for Analysis, Characterization, Testing and Simulation.
- Dr Y. Du and Dr S. Xi assisted in the collection of the X-ray absorption fine structure data in Singapore Synchrotron Light Source. I analyzed the data.

Chapter 6 is published as Y. Zhou, S. Xi, J. Wang, S. Sun, C. Wei, Z. Feng, Y. Du, Z. J. Xu. Revealing the Dominant Chemistry for Oxygen Reduction Reaction on Small Oxide Nanoparticles. *ACS Catal*. **8**, 673−677 (2017).

The contributions of the co-authors are as follows:

- Assoc. Prof Z. J. Xu and I conceived the idea and Assoc. Prof Z. J. Xu supervised the entire project.

- Assoc. Prof Z. J. Xu discussed and analyzed the measured data with me. I wrote the draft of the manuscript. The manuscript was revised together with Assoc. Prof Z. J. Xu and Assoc. Prof Z. J. Xu gave insightful suggestions for further improvement.
- I synthesized the materials, performed the electrochemical measurements, collected X-ray diffraction patterns, X-ray photoelectron spectroscopy, and conducted all the related data analysis.
- Dr. Y. Du and Dr. S. Xi assisted in the collection of the X-ray absorption fine structure data in Singapore Synchrotron Light Source. Dr. Y. Du did the curve fitting for the Extended X-Ray Absorption Fine Structure data. I also analyzed the data.
- Dr. J. Wang assisted in the collection of high-resolution Transmission Electron Microscopy.

Chapter 7 is published as Y. Zhou, S. Sun, J. Song, S. Xi, B. Chen, Y. Du, A. Fisher, F. Cheng, X. Wang, H. Zhang, Z. J. Xu. Enlarged Co-O covalency in octahedral sites leading to highly efficient spinel oxides for oxygen evolution reaction. *Adv. Mater*. 1802912 (2018).

The contributions of the co-authors are as follows:

- Assoc. Prof Z. J. Xu, Dr S. Sun and I conceived the idea and Assoc. Prof Z. J. Xu supervised the entire project.
- I prepared the manuscript drafts. Assoc. Prof Z. J. Xu discussed and analyzed the data with me. Assoc. Prof Z. J. Xu revised the manuscript and provided valuable suggestions which helped in polishing the manuscript further.
- I performed all the electrochemical measurements and analyzed the data.
- S. Sun synthesized the materials, collected the X-ray diffraction patterns and Brunauer-Emmett-Teller data in the Facility for Analysis, Characterization, Testing and Simulation.
- J. Song assisted in the collection of Density Functional Theory computation data.
- B. Chen collected the high-resolution Transmission Electron Microscopy in the Facility for Analysis, Characterization, Testing and Simulation.

- Dr Y. Du and Dr S. Xi assisted in the collection of the X-ray absorption fine structure data in Singapore Synchrotron Light Source. I analyzed the data.

Input Date Here

. . 21-Jan-2019 . . . .
Date

Input Signature Here

. . . . .ZHOU YE . . . . . .
Input Name Here

Abstract

The development of efficient ORR and OER oxide electrocatalysts has become the major challenge in sustainable clean energy technologies, for example, metal-air batteries, electrolyzers, and fuel cells. Gaining fundamental understandings on oxide towards electrocatalysis is a critical component in guiding the efficient design of highly active electrocatalysts. Special attention has been given to the spinel oxide family in this thesis.

This dissertation first addresses the effect of transition metal coordination in spinel oxide on electrocatalysis. By tuning the occupation ratio of Co in the tetrahedral and octahedral site, a positive correlation between the OER activities of $CoAl_2O_4$ and the octahedral occupancy of Co has been built, demonstrating the leading role of octahedral geometry in oxygen electrocatalysis. Second, the underlying origin of the composition-dependent ORR of Mn-Co containing spinel oxides is examined. Given a fair comparison of the catalyst intrinsic activity, it is found that the distinctive ORR of $ZnCo_xMn_{2-x}O_4$ is strongly correlated to the e_g electron of active Mn that resulting from the superexchange interactions ($Mn_{[Oh]}$-O-$Co_{[Oh]}$) through the edge-sharing [$Co_xMn_{1-x}O_6$] octahedra. Third, ultra-small size ferrite nanoparticles are examined as ORR catalyst to check whether the bulk descriptor is applicable to nanoparticle systems. Instead of bulk chemistry, the surface chemistry is identified as the dominating parameter for ORR of nanoparticle oxides. The high surface/bulk ratio of nanoparticles gives a totally different surface composition and the near-surface Mn density revealed from an electrochemical approach strongly correlates to the distinctive ORR activity given by the various ferrite oxide catalysts. Fourth, following the fundamental studies on composition-dependent ORR, a series of $ZnFe_xCo_{2-x}O_4$ ($x=0\sim2$) oxides were studied as OER catalysts to reveal the underlying origin for the composition dependent OER. It is revealed that the Co-O covalency dominates the distinctive OER of $ZnFe_xCo_{2-x}O_4$ and an enlarged Co-O covalency by 10 ~ 30 at% Fe substitution gives rise to the activity promotion. Unlike the oxygen-deficient perovskite oxides, the lattice oxygen-mediated OER is not considered as a favorable route for the best-performing $ZnFe_{0.4}Co_{1.6}O_4$ catalyst owing to its cation-deficient nature (give a wide energy gap between the O p-band and Fermi level).

Lay Summary

The use of catalyst aims to accelerate a given electrochemical reaction. That means in the presence of catalyst, a given reaction can be triggered by applying at much lower energy. The current clean energy storage/conversion devices (e.g. hydrogen fuel cells, water electrolyzer) involves two half-reactions at the anode and cathode. Generally, the overall efficiency of such device is limited by the more sluggish reaction on one side. The slow reaction rate of oxygen reduction reaction (ORR) and oxygen evolution reaction (OER) in the above mentioned clean energy devices has stimulated efforts in screening or designing highly active ORR/OER catalysts. Seeking cheap oxide electrocatalysts emerges as an important direction because cost-efficiency and environmental friendless are the key for future commercialization. This dissertation touches on the intriguing crystal family: spinel oxide (AB_2O_4). Special attention has been given to identifying the fundamental origin of the distinctive ORR/OER performance produced by spinel oxides. That means not only the phenomenon but also what's behind the phenomenon is carefully examined. Through a fair comparison of catalyst performance, the key component or the catalytic-critical parameter for a good catalyst is extracted in this thesis. This research work is important because the identified catalytic-critical parameter is essential to the knowledge-guided design of active oxide catalysts. With the information provided, one knows exactly what the design principles for efficient oxide catalysts are. By knowing the design principles, time-consuming screening time can be saved.

This research work is novel due to the following two aspects. First, most existing studies on spinel oxide only focused on reporting the phenomenon. It is common for researchers to employ different strategies to regulate the oxide catalytic activity. Some strategies work, some are not. Further analysis probing the underlying origin of the activity promotion or demotion is missing. In contrast, this dissertation work presents readers the catalytic-critical component for a good catalyst, thus the most proper engineering strategies can be targeted. In addition, this thesis provides new mechanism understanding on the OER of spinel oxide. It is known that transition metal oxides consist of metal and oxygen elements. Traditional understanding on OER considers the metal site as the active center, which means the reactants are attached to the transition metal sites. More recently, researchers found experimental evidences in oxygen-deficient perovskite oxides ($ABO_{3-\delta}$, another crystal family) showing that the lattice oxygen can also participate during OER (i.e. the oxygen in the oxide lattice can exchange with the reactant). This dissertation first demonstrates that the oxygen in spinel lattice is unlikely to participate during OER due to the cation-deficient surface defect chemistry of spinel oxide.

Acknowledgments

This research would not have been possible without the financial support from the Singapore Ministry of Education Tier 1 Grant, Tier 2 Grant and the Singapore National Research Foundation under its Campus for Research Excellence And Technological Enterprise (CREATE) programme.

Special appreciation must be conveyed to my supervisor, Associate Professor Zhichuan J. Xu, for the professional guidance and encouragement he has provided during my PhD period.

I would like to thank all the technical staff in Facilities for Analysis, Characterization, Testing & Simulation (FACTS) lab and inorganic lab for providing the equipment and safety training.

This research project largely benefited from the input of Dr. Yonghua Du and Dr. Shibo Xi for the XAFS data collection in the Singapore Synchrotron Light Source.

I am grateful to my group members, whom I've had the great pleasure to work with, for the kind assistance and support.

Table of Contents

Table Captions

Table 4.1 Deconvolution of Al 2p XPS spectra. XPS peak position, area distribution and chemical bonding, percentage of Al in tetrahedral site and octahedral site.

Table 5.1 ORR onset potentials of $ZnCo_xMn_{2-x}O_4$ oxides (defined as the potential to drive a current density of 1 mA $cm^{-2}{}_{disk}$).

Table 5.2 ORR activities of $ZnCo_{1.4}Mn_{0.6}O_4$ and various Co-Mn based spinel catalysts reported in literature (Co-Mn spinel oxide are physically mixed with conductive additive).

Table 6.1 Theoretical density (ρ), mean ferrite particle diameters (d) obtained from TEM images and calculated surface area of the various $Mn_xFe_{3-x}O_4$ nanoparticles.

Table 6.2 Summary of the EXAFS fitting results for $Mn_xFe_{3-x}O_4$ (x=0.5~2.5). Bond length (Mn-O_4 and Mn-O_6), Coordination number (N) and Mn occupancy (x_{Mn}) in tetrahedral site and octahedral site obtained by fitting the experimental EXAFS spectra.

Table 6.3 Mn oxidation state obtained from XPS, faradaic charge associated with the reduction of surface Mn, determined effective Mn density at the oxide surface.

Table 7.1 The defect formation enthalpies ΔH_f under oxygen rich chemical potentials ($\mu_0 = 0$ eV). As a result of oxygen rich condition ($\mu_0 = 0$ eV), $\mu_{Zn} = -3.754$ eV.

Table 7.2 ICP-OES (Inductively coupled plasma-optical emission spectrometry) analysis results of spinel $ZnFe_{0.4}Co_{1.6}O_4$ and $ZnFe_{0.6}Co_{1.4}O_4$.

Table 7.3 Computing results of the Bader charge analysis.

Table 7.4 The determined Co d, O p band center, Co-O band center distance and Fermi level energy from the DOS calculation.

Figure Captions

Figure 2.1 (a) Hydrogen and oxygen-based energy storage/conversion. (b) Illustration of the overpotentials of oxygen electrocatalysis (OER, ORR) and hydrogen electrocatalysis (hydrogen evolution reaction (HER), hydrogen oxidation reaction (HOR)).

Figure 2.2 Catalyst OER activity comparison by overpotentials required to drive a current density of 10 mA cm^{-2}.

Figure 2.3 (a) OER activity comparisons of the various oxide catalysts by the specific current density at a potential of 1.60 V vs. RHE. (b) Specific current density as a function of E-iR.

Figure 2.4 (a) Double layer capacitance measurements of NiO_x at different scan rates (5 mV s^{-1}, 10 mV s^{-1}, 25 mV s^{-1}, 50 mV s^{-1}, 100 mV s^{-1}, 200 mV s^{-1} and 400 mV s^{-1}). (b) The plotting of cathodic and anodic currents at 0.25 V vs SCE versus scan rate.

Figure 2.5 (a) Comparison of non-Faradaic capacitance of NiFe and NiFe/NiFe:Pi electrodes (200 mV s^{-1}); (b) Electrochemical impedance spectra (EIS); Contact angle measurements of (c) NiFe and (d) NiFe/NiFe:Pi electrode.

Figure 2.6 (a) The ORR polarization curves of Pt/C, N-rmGO, Co_3O_4/N-rmGO hybrid, $MnCo_2O_4$ + N-rmGO mixture, and $MnCo_2O_4$/N-rmGO hybrid in O_2-saturated 1 M KOH at a rotating speed of1600 rpm. (b) OER polarization curves of $MnCo_2O_4$ + CB mixture, $MnCo_2O_4$ + N-rmGO mixture, $MnCo_2O_4$, Co_3O_4/N-rmGO hybrid, and $MnCo_2O_4$/N-rmGO hybrid in 1 M KOH.

Figure 2.7 OER activity as a function of Sc content.

Figure 2.8 (a) CV curves of PC-18-950 specimen in 0.1 M KOH electrolyte. (b) ORR negative scans of XC-72, PC-18-950 and Pt/C catalysts at rotating speed of 1600 rpm.

a facile chemical method.

Figure 3.3 Illustration of drop-casting method and uniform thin film on the RDE.

Figure 3.4 (a) Schematic of rotating disk electrode system (b) Set up of the three-electrode system.

Figure 3.5 (a) Representative ORR polarization curve (negative-going scan) at different rotating speed. (b) The Koutecky-Levich plot.

Figure 3.6 Schematic illustration of a rotating ring-disk electrode.

Figure 3.7 Linear sweep voltammetry curves recorded on RRDE in O_2-free 1.0 M KNO_3 + 0.01 M $[Fe(III)(CN)_6]^{3-}$ aqueous solution at a scan rate of 50 mV s^{-1} with applying a ring potential of 0.361 vs. SHE.

Figure 3.8 Diffraction of X-rays by crystalline matter.

Figure 3.9 Essential component of typical diffractometer.

Figure 3.10 (a) Illustration of XAFS measurements. A beam of X-rays (intensity I_0) passes through a homogeneous sample (thickness x) and loses certain intensity due to the interaction. The transmitted X-ray intensity is measured to give the absorption coefficient μ.

Figure 3.11 Illustration of representative X-ray absorption spectroscopy. Three absorption edges can be observed (K, L, and M edges), corresponding to the electron emission from K, L, M shells, respectively.

Figure 3.12 Illustration of the single scattering. The photoelectron emitted from the absorbing atom (A) is back-scattered by a single scattering atom (S). The final-state wave function at the absorber is modified by the back-scattered wave. If the out-going and back-scattered waves are in phase, there will be constructive interference and the wave function increases. If the out-going and back-scattered waves are out of phase, it gives destructive interference and decreased wave function. R_{as} is the distance between the absorbing and scattering atom.

Figure 3.13 Illustration of photoelectron generations.

Figure 3.14 The binding energies and ionization cross-section of Uranium.

Figure 3.15 BET model of multilayer adsorption.

Figure 3.16 Five representative adsorption isotherms given by solid materials with different pore size distribution and surface features.

Figure 3.17 (a) Signals emitted from the sample-electron interaction. (b) Mechanism of emission of secondary electron (SE), backscattered electron (BSE) and characteristic X-ray.

Figure 4.1 (a) XRD patterns and (b) BET surface area of $CoAl_2O_4$ oxides prepared at different temperatures ranging from 400°C to 800°C. SEM images of $CoAl_2O_4$ prepared at (c) 400°C (d) 500°C (e) 600°C and (f) 800°C.

Figure 4.2 (a) Co K-edge XANES spectra and (b) the determined absorption edge positions and valence states of Co in the various $CoAl_2O_4$ oxides. (c) XPS spectra (grey dots) and deconvoluted XPS spectra (solid color lines) of Co 2p for $CoAl_2O_4$ oxides.

Figure 4.3 (a) OER CV curves and (b) OER Tafel plots of the various $CoAl_2O_4$ oxides.

Figure 4.4 (a) EXAFS spectra of $CoAl_2O_4$ oxides at Co K-edge. (b) XPS spectra and peak deconvolution of Al 2p in $CoAl_2O_4$ oxides. (c) Tetrahedral and octahedral site-occupancy of Co in $CoAl_2O_4$, determined by peak deconvolution of Al 2p XPS spectra.

Figure 4.5 Images of synthesized $CoAl_2O_4$ at (a) 400°C (b) 500°C (c) 600°C and (d) 800°C.

Figure 4.6 OER specific activity as a function of Co occupancy in octahedral sites.

Figure 5.1 (a) Crystal structure of spinel oxide. (b) XRD pattern and (c) BET surface area of the synthesized $ZnCo_xMn_{2-x}O_4$ oxides.

Figure 5.2 Normalized XANES spectra at (a) Co, (b) Mn and (c) Zn K-edge. (d) The quantified Mn and Co valence state obtained from XANES analysis.

Figure 5.3 (a) Charge redistribution via $Mn^{3+} + Co^{3+} \rightarrow Mn^{4+} + Co^{2+}$. (b) EXAFS k^3 $\chi(R)$ spectra at Zn, Co and Mn K-edge for $ZnCo_xMn_{2-x}O_4$.

Figure 5.4 (a) Representative background CV scanned in Ar-saturated electrolyte and ORR polarization curves at different rotating speeds in O_2-saturated 0.1 M KOH electrolyte ($ZnCo_{1.4}Mn_{0.6}O_4$). (b) ORR polarization curves of $ZnCo_xMn_{2-x}O_4$ at a rotating speed of 1600 rpm, inset is the Koutecky-Levich plots at applied potential of 0.4 V. (c) Specific activities of $ZnCo_xMn_{2-x}O_4$, compared with those reported in the landmark literature: Pt/C and $LaMnO_{3+\delta}$. (d) Potentials at 25 μA cm^{-2}_{ox} for the various $ZnCo_xMn_{2-x}O_4$ catalysts.

Figure 5.5 SEM images of $ZnCo_xMn_{2-x}O_4$ oxides with a Co substitution amount of (a) 0, (b) 0.2, (c) 0.6, (d) 1.0, (e) 1.4, (f) 1.8, and (g) 2.0.

Figure 5.6 (a) Correlation between Mn valence state and ORR potentials at 25 μA cm^{-2}_{ox}. (b) ORR potentials at 25 μA cm^{-2}_{ox} as a function of e_g electron in $ZnCo_xMn_{2-x}O_4$. Dash line is the established volcano map (e_g theory) in Yang's work regarding perovskite group.

Figure 6.1 TEM images of $Mn_xFe_{3-x}O_4$/C and corresponding size distribution of

Abbreviations

XAFS	X-ray absorption fine structure
XANES	X-ray absorption near edge structure
EXAFS	Extended X-Ray Absorption Fine Structure
HRTEM	High-Resolution Transmission Electron Microscopy
TEM	Transmission Electron Microscopy
SAED	Selected Area Electron Diffraction
FFT	Fast Fourier Transform
SEM	Scanning Electron Microscopy
EDS	Energy Dispersive X-ray Spectroscopy
XRD	X-ray Diffraction
XPS	X-ray photoelectron spectroscopy
DFT	Density functional theory
BET	Brunauer-Emmett-Teller
ORR	Oxygen reduction reaction
OER	Oxygen evolution reaction
RDE	Rotating disk electrode

Chapter 1

Introduction

The development of efficient ORR and OER oxide electrocatalysts has become the major challenge in sustainable clean energy technologies (e.g. metal-air batteries, fuel cells and electrolyzers). Spinel is an intriguing crystal family to work on. In chapter 1, the unsolved problems regarding the geometric factor in spinel oxide, fundamental origin of the composition-dependent ORR and OER activity by Mn- and Co-based spinel oxides and the untouched lattice oxygen activity towards OER in spinel oxides are analyzed, which rationalizes the selection of spinel electrocatalyst and corresponding experimental design in the thesis.

1.1 Hypothesis

The increasing consumption of fossil fuels has created daunting environmental issues across the globe. To break this vicious cycle, a clean energy infrastructure is needed. Energy storage/conversion devices that rely on oxygen and hydrogen electrocatalysis (e.g. rechargeable metal-air batteries, electrolyzers and fuel cells) are promising sustainable energy infrastructures[1] that human beings should put considerable efforts on. In fact, the two electrochemical reactions (i.e. oxygen reduction reaction and oxygen evolution reaction) remains the key to the whole energy system owing to their sluggish kinetics.[2] Developing efficient ORR/OER electrocatalysts with low cost is of paramount importance. Transition metal oxides are promising candidates because they are cost-effective and show great tenability in electronic structure.[2-3] Perovskite oxide family has been considered as promising oxygen electrocatalysts, and it is worth noting that the octahedral [TMO_6] unit is the only contributor in perovskite oxide towards electrocatalysis.[3-6] Since spinel also contains such octahedral units, it is thus inspiring to examine spinel oxides as ORR/OER electrocatalyst. More importantly, it is necessary to develop fundamental understandings to guide the efficient design of highly active electrocatalysts.

In addition to the octahedral sites, spinel oxide also contains four oxygen-coordinated tetrahedral site where transition metals can occupy. Which geometric site is more catalytically critical in the spinel oxide remains unanswered. By regulating the occupation ratio of active elements between the two geometric sites, the catalytic-critical geometry might be identified. The thesis tests the hypothesis in chapter 4 that the octahedral geometry, instead of tetrahedral, plays a leading role towards oxygen electrocatalysis.

The oxide electrocatalysts that have been identified active for ORR are mainly Mn-based oxides.[7-11] According to literature reports, the developed $MnCo_2O_4$/N-doped-rmGO and $MnFe_2O_4$/C [10-11] show great ORR activity approaches that of state-of-the-art Pt/C catalyst. It is found that the foreign metal-substituted Mn spinel oxides show distinctive ORR activities, depending strongly on the composition.[7, 10] For example, $Mn_xCo_{3-x}O_4$ spinel oxide gives the highest ORR activity with an optimum Mn/Co ratio varying from 0.15~2.0 based on earlier studies.[8, 12-13] The fundamental understanding on the composition-dependent ORR activity remains elusive mainly due to a lack of analysis by catalyst intrinsic/specific activity. In addition, the design of hybrid structure (e.g. $MnCo_2O_4$/N-doped-rmGO[11]) impedes the evaluation of oxides' true catalytic contribution due to the positive synergistic effect between the carbon and oxide. Given a fair comparison of catalyst intrinsic activity, the thesis tests the hypothesis in chapter 5 that there exists a dominating parameter governing the composition-dependent ORR of substituted Mn spinel oxides.

A scaling relationship between the surface and bulk energetics has been built in perovskite oxides AMO_3 (A represents La or Sr, M represents metal element from Sc to Ge) by researchers, consolidating the theory that the bulk thermochemistry act as a good descriptor for transition metal oxides' electrocatalytic activity.[14] It is known that the perovskite oxides are generally of micro-scale size,[4, 6] while ultra-small (< 10 nm) spinel oxide particles can be prepared by versatile approaches.[10] For ultra-small size nanoparticles, the surface might be totally different with respect to their bulk and the scaling relationship between the surface and the bulk might no longer exist. Thus, ultra-small size manganese ferrite particles can be prepared by a well-established facile chemical method and studied as ORR catalysts. The thesis tests the hypothesis in chapter 6 that when oxide particles are developed into nano-size scale, the bulk descriptor is not sufficient to explain the distinctive ORR activity and near-surface properties become more catalytic-critical.

The Co-containing oxides are among the most active OER oxide catalysts reported.[15-16] Substituting foreign transition metals elements for Co in spinel oxide has been found to be an effective approach in tuning the OER. Substituted cobaltites (e.g. $Zn_xCo_{3-x}O_4$,[17] $Ni_xCo_{3-x}O_4$[18]) have shown promoted OER activities relative to that of pure Co_3O_4. The activity enhancement has been attributed to markedly changed morphologies with large roughness factor and high active site density.[17-18] More fundamental understanding of the intrinsic origins remains limited. The thesis tests the hypothesis in chapter 7 that there exists a dominating parameter governing the composition-dependent ORR of Fe-substituted Co spinel oxides.

Recently, the traditional OER mechanism understanding—centered on the redox chemistry of the metal cation— has been challenged. It is suggested that the anion-redox also plays an important part in oxygen electrocatalysis.[19-22] The groundbreaking vision that lattice oxygen act as active centers in oxygen-deficient perovskite oxides has been supported as researchers recently found incontrovertible evidence of lattice oxygen oxidation during OER by in-situ mass spectrometry.[20] The increased covalency of TM-O bond has been considered critical in triggering the lattice oxygen participation.[20, 23] The lattice oxygen-mediated OER reaction pathways has been proposed by different research groups.[20, 22] However, most existing mechanism studies touching the lattice oxygen involvement have been focus on oxygen deficient perovskite oxides, e.g. BSCF82, $Pr_{0.5}Ba_{0.5}CoO_{3-\delta}$, $La_{1-x}Sr_xCoO_{3-\delta}$, and etc.[20, 22] It is worth noting that the oxygen vacancy concentration on the surface could be orders of magnitude higher than that in the bulk. Therefore, the surface defect chemistry might play an influencing role on catalytic reaction pathways. While for spinel oxide, it tends to form cation deficiencies (an oxygen-excess nonstoichiometry) and exhibit p-type conductivity.[24-25] This could actually make a difference to the mechanistic understanding of OER by spinel materials. Cation-deficient Co-containing spinel oxides can be prepared and studies as OER catalyst. It is known the Zn spinels are generally categorized as p-type semiconductor,[25] thus the introduction of Zn could help produce spinel oxides with cation deficiency. By investigating the cation-deficient spinel oxides as OER electrocatalyst, the thesis tests the hypothesis in chapter 7 that when oxides with cation deficiency, instead of oxygen deficiency, the lattice oxygen participated OER is not favorable.

1.2 Objectives and Scope

The overall objective of this dissertation is to develop fundamental understanding on the ORR by Mn-based spinel oxides as well as OER by Co-based spinel oxide. Such fundamental studies could facilitate knowledge-guided design of efficient oxide electrocatalyst in the future. It is known that spinel contains two geometry site, i.e. tetrahedral site and octahedral site. To identify the catalytic-critical geometry, various spinel $CoAl_2O_4$ oxides with different cation distribution (i.e. $(Co_{0.33}Al_{0.67})_{Td}[Co_{0.67}Al_{1.33}]_{Oct}O_4$, $(Co_{0.42}Al_{0.58})_{Td}[Co_{0.58}Al_{1.42}]_{Oct}O_4$, $(Co_{0.81}Al_{0.19})_{Td}[Co_{0.19}Al_{1.81}]_{Oct}O_4$ and $(Co_{0.85}Al_{0.15})_{Td}[Co_{0.15}Al_{1.85}]_{Oct}O_4$) are studied as OER catalysts. A correlation between the OER activity and the octahedral occupation of Co has been established. As Mn-based oxides are generally considered as promising ORR catalyst,[10-11] the Mn-based spinel oxides, i.e. micro-size $ZnCo_xMn_{2-x}O_4$ and nano-size $Mn_xFe_{3-x}O_4$, are investigated as ORR catalysts. Assisted by the X-ray absorption fine structure (XAFS) technique, the catalytic-critical parameter that dominates the ORR of micro-size $ZnCo_xMn_{2-x}O_4$ spinel catalysts is revealed first. To check if the established bulk descriptor in micro-size $ZnCo_xMn_{2-x}O_4$ is applicable to the nano-size system, spinel $Mn_xFe_{3-x}O_4$ (x=0.5~2.5) oxides with particle sizes ranging from 5~15 nm are synthesized by a facile wet chemical method and examined as ORR catalysts. Unlike the micro-size particles, the surface of nano-size particles differs greatly from the bulk. Therefore, some surface sensitive techniques are employed in helping the understanding of ORR catalyzed by small-size spinel oxides. Since OER is also a key electrochemical reaction in clean energy infrastructure and Co-based oxides have been identified as active towards OER,[15-16] efforts are extended to the investigation of Co-based spinel oxide as OER electrocatalyst. Specifically, Fe-substituted Co spinel oxides ($ZnFe_xCo_{2-x}O_4$ (x= 0~2.0)) are synthesized via a sol-gel combustion method. Mechanism understanding are assisted by density functional theory (DFT) computation and XAFS characterization.

1.3 Dissertation Overview

The thesis addresses the transition metal geometric role in spinel oxide and the fundamental origin of the composition dependent ORR and OER by spinel structured oxide materials (more specifically, Mn-based spinel oxides for ORR and Co-based spinel oxides for OER).

Chapter 1 provides a rationale for the fundamental research on ORR and OER oxide electrocatalyst and outlines the goals and scope.

Chapter 2 reviews the literature concerning the catalyst performance evaluation, the existing strategies in engineering oxides' catalytic OER/ORR activity and the significant importance of identifying catalytically critical parameters and developing mechanism understanding to provide knowledge-guided design of efficient oxide electrocatalysts.

Chapter 3 discusses the principles underlying the experimental methodology, synthesis approach and material characterization techniques employed. Rationale for the selection of various techniques, electrode fabrication, and electrochemical data analysis are also included.

Chapter 4 elaborates the leading role of octahedral geometry in spinel oxides towards oxygen electrocatalysis.

Chapter 5 elaborates the role of superexchange interaction in the electronic structure change of Mn and Co in octahedra [$Co_xMn_{1-x}O_6$]. The dominating parameter for the distinctive ORR by spinel $ZnCo_xMn_{2-x}O_4$ oxides has been successfully identified.

Chapter 6 elaborates the interplay between Mn valence state and surface Mn density in the ORR of ultra-small size spinel $Mn_xFe_{3-x}O_4$ oxides.

Chapter 7 elaborates the role of Co-O covalency in the OER of substituted Co spinel oxides. Mechanism understanding on the cation-deficient spinel oxide has been revealed and the activity of lattice oxygen in spinel oxide towards OER has been discussed.

Chapter 8 draws together the threads of the thesis. To what extent the hypotheses have been validated and the recommended future work are presented.

1.4 Findings and Outcomes

This research led to several novel outcomes by:

1. Identifying the critical role of octahedral geometry in spinel oxide towards oxygen electrocatalysis.
2. Correlating the superexchange interaction between the edge-sharing [$Co_xMn_{1-x}O_6$] octahedra to the valence state evolution of the octahedral cations.
3. Elucidating the physical origin of the distinctive ORR performance of Mn-Co containing spinel oxides.
4. Revealing the dominant chemistry for ORR on small oxide nanoparticles.

5. Uncovering the unique advantage of electrochemical method in approaching the near-surface information of Mn-containing oxide nanoparticles.
6. Identifying the critical role of Co-O covalency in the OER performance of spinel $ZnFe_xCo_{2-x}O_4$ (x= 0~2.0).
7. Demonstrating the low probability of lattice-oxygen participation OER in cation-deficient spinel oxides.

References

[1] I. Katsounaros, S. Cherevko, A. R. Zeradjanin, K. J. Mayrhofer, *Angew Chem Int Ed Engl* **2014**, 53, 102-121.

[2] W. T. Hong, M. Risch, K. A. Stoerzinger, A. Grimaud, J. Suntivichb, Y. Shao-Horn, *Energy Environ. Sci* **2015**, 8, 1404-1427.

[3] J. Hwang, R. R. Rao, L. Giordano, Y. Katayama, Y. Yu, Y. Shao-Horn, *Science* **2017**, 358, 751-756.

[4] J. Suntivich, K. J. May, H. A.Gasteiger, J. B. Goodenough, Y. Shao-Horn, *Science* **2011**, 334, 1383-1385.

[5] W. T. Hong, K. A. Stoerzinger, Y.-L. Lee, L. Giordano, A. Grimaud, A. M. Johnson, J. Hwang, E. J. Crumlin, W. Yang, Y. Shao-Horn, *Energy Environ. Sci.* **2017**, 10, 2190-2200.

[6] K. J. May, C. E. Carlton, K. A. Stoerzinger, M. Risch, J. Suntivich, Y.-L. Lee, A. Grimaud, Y. Shao-Horn, *J. Phys. Chem. Lett.* **2012**, 3, 3264-3270.

[7] C. Li, X. Han, F. Cheng, Y. Hu, C. Chen, J. Chen, *Nat. Commun.* **2015**, 6, 7345.

[8] F. Cheng, J. Shen, B. Peng, Y. Pan, Z. Tao, J. Chen, *Nat. Chem.* **2011**, 3, 79-84.

[9] J. Du, C. Chen, F. Cheng, J. Chen, *Inorg Chem* **2015**, 54, 5467-5474.

[10] H. Zhu, S. Zhang, Y. X. Huang, L. Wu, S. Sun, *Nano Lett.* **2013**, 13, 2947-2951.

[11] Y. Liang, H. Wang, J. Zhou, Y. Li, J. Wang, T. Regier, H. Dai, *J. Am. Chem. Soc.* **2012**, 134, 3517-3523.

[12] E. Lee, J.-H. Jang, Y.-U. Kwon, *J. Power Sources* **2015**, 273, 735-741.

[13] A. Restovic, E. Rıos, S. Barbato, J. Ortiz, J. Gautier, *J Electroanal Chem* **2002**, 522, 141-151.

[14] F. Calle-Vallejo, O. A. Díaz-Morales, M. J. Kolb, M. T. M. Koper, *ACS Catal.* **2015**, 5, 869-873.

[15] T. Maiyalagan, K. A. Jarvis, S. Therese, P. J. Ferreira, A. Manthiram, *Nat. Commun.* **2014**, 5, 1.

[16] Y. P. Zhu, T. Y. Ma, M. Jaroniec, S. Z. Qiao, *Angew. Chem. Int. Ed.* **2017**, 56, 1324-1328.

[17] X. Liu, Z. Chang, L. Luo, T. Xu, X. Lei, J. Liu, X. Sun, *Chem. Mater.* **2014**, 26, 1889-1895.

[18] Y. Li, P. Hasin, Y. Wu, *Adv. Mater.* **2010**, 22, 1926-1929.

[19] D. N. Mueller, M. L. Machala, H. Bluhm, W. C. Chueh, *Nat Commun* **2015**, 6, 6097.

[20] A. Grimaud, O. Diaz-Morales, B. Han, W. T. Hong, Y.-L. Lee, L. Giordano, K. A. Stoerzinger, M. T. Koper, Y. Shao-Horn, *Nat. Chem.* **2017**, 9, 457-465.

[21] C. Yang, A. Grimaud, *Catalysts* **2017**, 7, 149.

[22] J. T. Mefford, X. Rong, A. M. Abakumov, W. G. Hardin, S. Dai, A. M. Kolpak, K. P. Johnston, K. J. Stevenson, *Nat Commun* **2016**, 7, 11053.

[23] X. Rong, J. Parolin, A. M. Kolpak, *ACS Catal.* **2016**, 6, 1153-1158.

[24] C. Wei, Z. Feng, G. G. Scherer, J. Barber, Y. Shao-Horn, Z. J. Xu, *Adv. Mater.* **2017**, 1606800.

[25] M. N. Amini, H. Dixit, R. Saniz, D. Lamoen, B. Partoens, *Phys. Chem. Chem. Phys.* **2014**, 16, 2588-2596.

Chapter 2

Literature Review

The depletion of fossil fuels and a desperate need to advance clean energy revolution have stimulated investigations on the design of efficient oxide catalysts towards oxygen electrocatalysis (ORR and OER). A knowledge-guided design requires a fundamental understanding of the physicochemical principles behind the catalytic phenomenon. In this chapter, the different benchmarking methodologies are evaluated and the current efforts in designing efficient ORR/OER transition metal oxide catalysts are reviewed. In addition, the existing mechanism understanding centered on the redox of metallic center and lattice oxygen towards oxygen electrocatalysis is elaborated.

2.1 Transition metal oxide in energy storage and conversion

The dominating consumption of fossil fuels has created daunting environmental issues across the globe and there is a desperate need for clean energy resources to alleviate this crisis. Energy storage and conversion devices that rely on oxygen and hydrogen electrocatalysis like rechargeable metal-air batteries, electrolyzers, and fuel cells have received tremendous attention. As shown by Figure 2.1, the hydrogen fuel cells suffer from tremendous energy losses owing to the sluggish oxygen reduction reaction (ORR).[1] The metal-air batteries and electrolyzer are mostly challenged by the low kinetics of oxygen evolution reaction (OER) at the anode.[1]

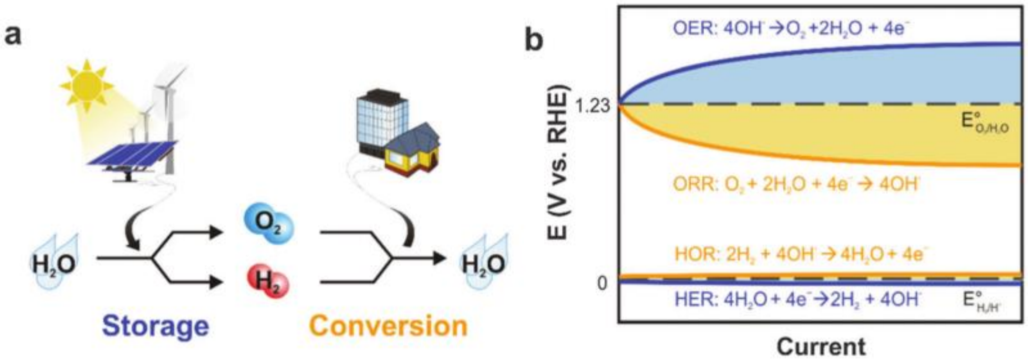

Figure 2.1 (a) Hydrogen and oxygen-based energy storage/conversion. (b) Illustration of the overpotentials of oxygen electrocatalysis (OER, ORR) and hydrogen electrocatalysis (hydrogen evolution reaction (HER), hydrogen oxidation reaction (HOR)).[1]

Some precious ORR or OER catalysts, e.g. Pt (ORR catalyst), IrO_2 and RuO_2 (OER catalysts), could offer decent catalytic efficiency, but are not sustainable choices.[2] Transition metal oxides, with their tunable electronic structures by versatile strategies, have emerging as promising alternatives. Significant progress has been made on perovskite, spinel, layered-oxides, and etc. towards electrocatalysis.[1]

2.2 Catalyst benchmarking methodology

Robust benchmarking systems are required to facilitate a straightforward comparison of catalysts' performance.[3] The reported key parameters include: (a) Overpotentials required to drive a fixed geometric current density, e.g. 10 mA cm^{-2} for OER (Figure 2.2);[4] (b) Mass activity; (c) Specific activity based on the surface area of the catalysts (Figure 2.3).[5-7]

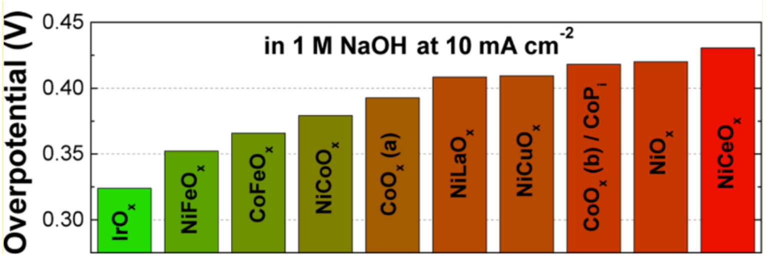

Figure 2.2 Catalyst OER activity comparison by overpotentials required to drive a current density of 10 mA cm^{-2}.[4]

Geometric current density, e.g. 10 mA cm^{-2}, defines the current per unit geometric area of electrode. This kind of activity assessment makes engineering sense because a high geometric current density is expected in commercial devices. When precious metal or metal oxide are employed as electrocatalysts, the mass activity becomes important because boosting the geometric activity by an increase of the catalyst mass loading is no longer an economically efficient way. In fact, both the geometric activity and mass activity of electrocatalysts can be maximized by increasing catalysts' specific surface area and specific/intrinsic activity.[3] The significant role of catalysts' specific surface is easy to understand because an increase of specific surface area produces more accessible reaction sites (note that electrocatalytic reactions only involve the surface). The specific activity is critical and fair in judging whether a material is intrinsically active for a reaction or not.[3, 5, 8] Specific activity refers to the activity that is normalized with respect to the catalyst surface area (Figure 2.3).[5] It is known that a solid electrode surface is not smooth and the real surface area involved in a catalytic reaction might far exceed the geometric disk area. The geometric benchmarking standard cannot exclude the artificial influence of the surface area and mass loading of catalysts. Benchmarking the catalytic activity of electrocatalysts by this parameter (e.g. overpotentials required to deliver a fixed geometric current density) is problematic. Strategies, like increasing the catalysts' mass loading, reducing the particle size, designing porous/hierarchical structures and depositing catalyst onto porous substrate, can all help attain a much lower overpotential at a fixed disk current density. The mass activity standard is also not fair to judge the intrinsic activity of a given catalyst. This is because the electrocatalytic reactions only involve the surface atom.

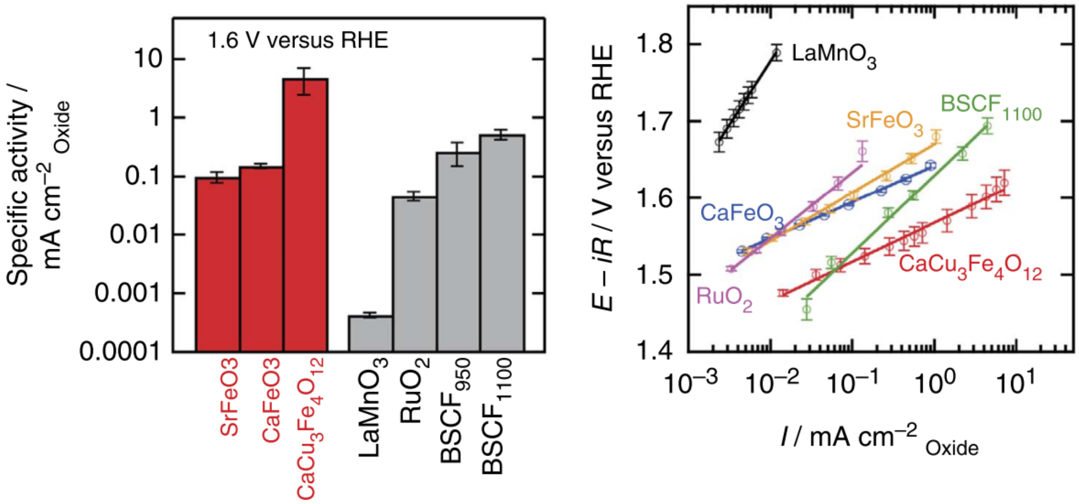

Figure 2.3 (a) OER activity comparisons of the various oxide catalysts by the specific current density at a potential of 1.60 V vs. RHE. (b) Specific current density as a function of E-iR.[5]

A relatively accurate assessment of catalysts' surface area is a prerequisite for determining the intrinsic catalytic nature of candidate catalyst materials. The electrochemically active surface area (ECSA) of noble metal electrodes, for example, Rh, Pt, Ir, can be determined by surface limited adsorption reactions.[9] A well-established standard for Pt ECSA determination is through integrating the hydrogen adsorption/desorption charges from the CV profiles.[9]

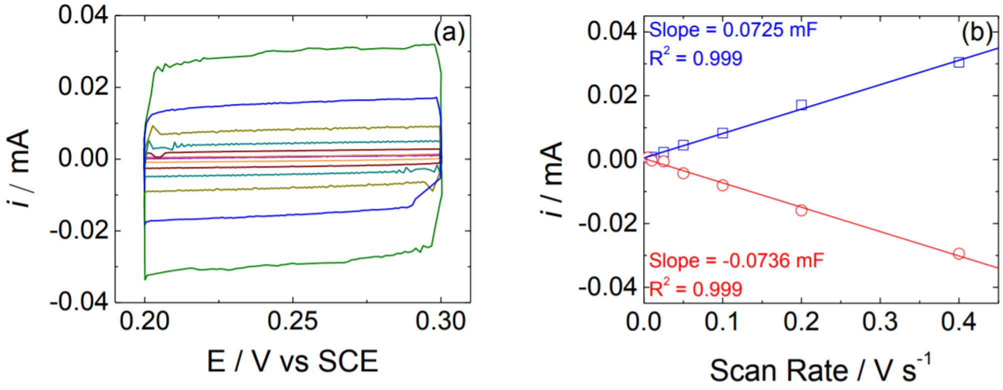

Figure 2.4 (a) Double layer capacitance measurements of NiO_x at different scan rates (5 mV s^{-1}, 10 mV s^{-1}, 25 mV s^{-1}, 50 mV s^{-1}, 100 mV s^{-1}, 200 mV s^{-1} and 400 mV s^{-1}). (b) The plotting of cathodic and anodic currents at 0.25 V vs SCE versus scan rate.[4]

For oxide materials, such surface adsorption reaction that allows the assessment of oxide ECSA is not quite available. An alternative method which utilizes the double layer capacitance region to help determine the ECSA of transition metal oxide is so far the most popular.[4, 9] As shown in Figure 2.4 a, the double layer CV loops are recorded at different scan rates.[4] The capacitive currents (both anodic and cathodic) at a given potential are plotted as a function of the scan rate (Figure 2.4 b) and the linear slope is obtained, which is equivalent to twice of the double layer capacity C_{dl}. The ECSA of the oxide can be calculated by referring the C_{dl} to the reference value of capacitance per unit area C_{ref}, as illustrated by the follow equation:[4, 9]

$$ECSA = C_{dl}/C_{ref}$$

For example, the ECSA of the various oxides (CoO_x, CoPi, $CoFeO_x$, NiO_x, $NiCeO_x$, $NiCoO_x$, $NiCuO_x$, $NiFeO_x$, and $NiLaO_x$) electrodeposited on the glassy carbon disk were determined through the double layer capacitance method.[4] A specific capacitance C_{ref} of 40 µF cm^{-2} was chosen to solve the ECSA values in 1M NaOH.[4] However, it is concerned that such ECSA determination method might produce significant errors and not applicable to catalysts in powder forms. As some of the oxide powders were mixed with conductive carbon in electrode preparation, solving the exact ECSA of oxide catalyst is problematic because it is difficult to differentiate between the oxide double-layer capacitance and the capacitance from carbon.[8] It is convinced that the unknown capacitive behavior of catalyst and carbon additive/substrate make the resulted ECSA value not that reliable.[4] In addition, it is known that the ECSA is calculated by referring the obtained double-layer capacity (C_{dl}) to the reference value of capacity per unit area (C_{ref}). However, to get the precise value of C_{ref} remains a challenge. According to literature reports, the C_{ref} values range from 0.022-0.130 mF cm^{-2} in alkaline solution and such discrepancy may lead to 100% errors.[9] For oxides in powder form, BET has been widely employed as the benchmark approach due to the lack of better alternatives.[8, 10]

2.3 Rational design of oxygen electrocatalyst

The current efforts toward the design of efficient oxygen electrocatalysts mainly focused on two aspects. One of the aspects is developing rational strategies to engineering the geometric or mass activity of electrocatalyst. Related attempts include increasing the accessible surface area,[11] designing hybrid structures (to induce positive synergistic coupling effect),[12] engineering catalyst composition[13] and manipulating or deliberately introducing defects.[14] Revealing the reaction mechanisms[15] and catalytically critical parameters[16] are the other important aspect researchers are now working on. The catalytically critical parameters are parameters that play an influencing role on the catalyst performance. Generally, the identified dominating parameters/descriptors are based on a fair analysis of catalyst intrinsic/specific activity. The descriptor and mechanism studies are of particular importance in directing the efficient design of highly active electrocatalysts.

2.3.1 Engineering catalyst geometric activity

2.3.1.1 Electrochemically accessible surface area

Hierarchical porous structure. The design of hierarchical porous structure aims to produce a high specific surface area and at the same time facilitate a fast mass transport, electron-transfer within the electrode. The hierarchical Mo–N/C@MoS_2,[17] Sulfur-Nitrogen Co-doped three-dimension carbon foams,[18] all give a high geometric current density. The geometric activity can be further promoted by depositing the catalyst materials onto porous electrode substrate. For example, the NiFe nanosheets decorated microporous Ni foam delivers a geometric current density of 500 $mAcm^{-2}{}_{disk}$ at an overpotentials of 240 mV.[11]

Wettability. It was reported that the adsorption of intermediate reactant molecules on the catalyst can be influenced by the catalyst surface wettability.[19-21] A recent study shows that the wettability of electrodeposited NiFe hydroxide can be modified by a phosphorylation process and such modification gives rise to an increased accessible surface area and OER geometric activity.[19] As shown in Figure 2.5, the wettability is indicated by the contact angles using sessile drop method. Through phosphorylation process, the contact angle was reduced to 44 ± 3° from 129 ± 5°.[19] The phosphorylation-induced distorted-tetrahedral cobalt geometry was proposed to be one of the potential reasons for such wettability modification.[19]

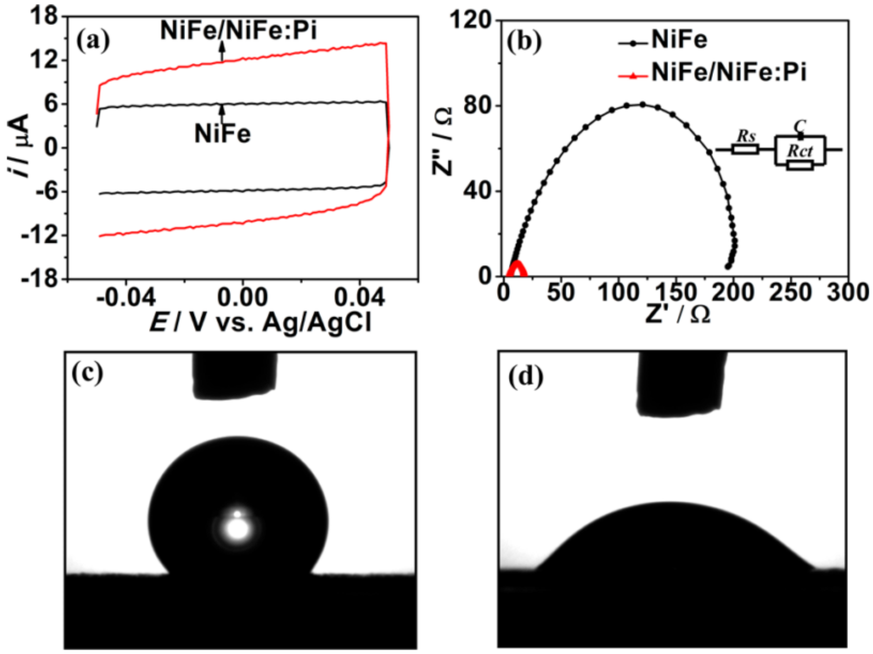

Figure 2.5 (a) Comparison of non-Faradaic capacitance of NiFe and NiFe/NiFe:Pi electrodes (200 mV s^{-1}); (b) Electrochemical impedance spectra (EIS); Contact angle measurements of (c) NiFe and (d) NiFe/NiFe:Pi electrode.[19]

Another study reported that the surface hydrophilicity of CoOOH nanosheet can be increased by designing a hybrid structure of CoOOH-graphene nanosheets.[21] According to the literature, the graphene has a strong electron affinity and could capture the Co 3d electrons, thereby effectively reduce the contact angle to 23°.[21] The increased wettability facilitate a fast proton-electron transfer at the catalyst-electrolyte interface, producing a promising OER performance. In addition to the design of hierarchical structure and the modification of surface wettability, reducing the particle size through new synthesis approach is also a feasible way to increase the geometric activity or mass activity.[22]

2.3.1.2 Design of hybrid structure

The hybrid structures, for example by in-situ growing of particles on the conductive carbon materials, generally yield a higher catalytic activity than the physical mixture of catalyst particles and carbon.[12, 23-24] According to literature report, the $MnCo_2O_4$/N-doped graphene hybrid shows a high geometric ORR current density of 151 mA cm^{-2} at an overpotential of 0.53 V, which is ~7 times the current afforded by the physical mixture of $MnCo_2O_4$ and N-doped graphene.[24] The synergistic effect between the $MnCo_2O_4$ and N-doped graphene was also indicated by the OER trend observed (Figure 2.6).[24]

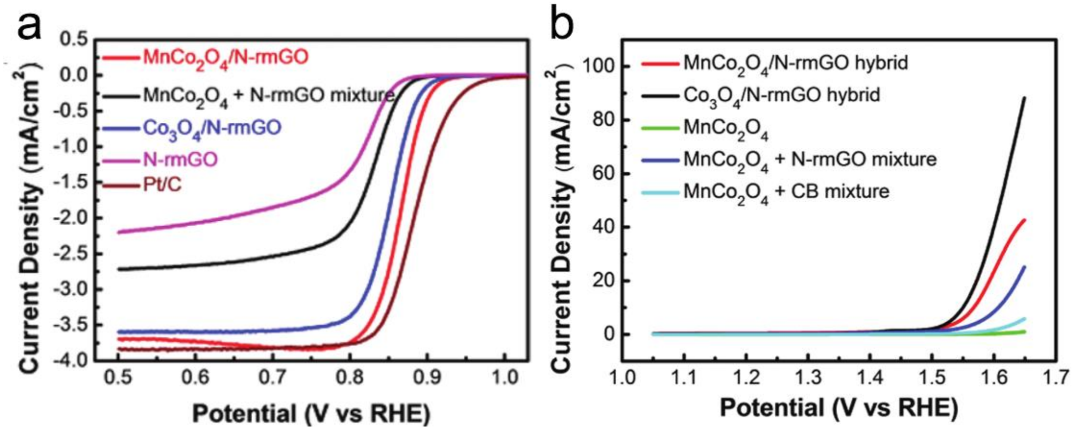

Figure 2.6 (a) The ORR polarization curves of Pt/C, N-rmGO, Co_3O_4/N-rmGO hybrid, $MnCo_2O_4$ + N-rmGO mixture, and $MnCo_2O_4$/N-rmGO hybrid in O_2-saturated 1 M KOH at a rotating speed of1600 rpm. (b) OER polarization curves of $MnCo_2O_4$ + CB mixture, $MnCo_2O_4$ + N-rmGO mixture, $MnCo_2O_4$, Co_3O_4/N-rmGO hybrid, and $MnCo_2O_4$/N-rmGO hybrid in 1 M KOH.[24]

The detection of such positive synergistic effect has advanced the progress on the fabrication of hybrid electrodes and the integration of intrinsic active electrocatalyst with carbon materials has become an effective strategy to push the electrocatalysts' activity further. As the NiFe layered double hydroxides (LDH) were identified as active OER catalysts, significant efforts have been devoted to the fabrication of NiFe LDH/nanocarbon hybrids.[12] Varies nanocarbon materials have been investigated, expanding from the zero-dimensional carbon to three- dimensional carbon (e.g. carbon nanotubes, graphene, porous graphene layers).[12] The strong interaction between the NiFe LDH and carbon via electron redistribution or formed covalent bond in between is critical in giving the enhanced positive synergistic effect.[12] The design of hybrid structures also facilitates the discovery of potential bi-functional electrocatalysts. For example, one might found that the Co_3O_4 is better at catalyzing OER than ORR. By integrating the Co_3O_4 oxide with N-doped graphene, it is found that the Co_3O_4/N-doped graphene hybrid delivers a high ORR activity approaches that of the Pt/C.[23] As the hybrid structure also produces enhanced OER activity, the Co_3O_4/N-doped graphene hybrid appears to be a promising non-precious bi-functional catalyst for OER and ORR in alkaline electrolyte.[23]

2.3.1.3 Compositional engineering

Foreign metal substitution or compositional tuning in mixed metal oxides has been proven to be an effective way to engineer the catalytic properties. The composition-dependent catalytic activity has been extensively reported. For example, the spinel $Mn_xCo_{3-x}O_4$, $M_xFe_{3-x}O_4$ (M = Fe, Cu, Co, Mn) nanoparticles[25] and perovskite $Ba_{0.5}Sr_{0.5}Co_xFe_{1-x}O_{3-\delta}$[26] all displayed distinctive ORR/OER activities depending on the composition. Specifically, B-site doping is a common practice for tuning the catalytic performance of perovskite materials. Perovskite materials show high composition and doping flexibility due to its high tolerance for oxygen non-stoichiometry and structure distortion.

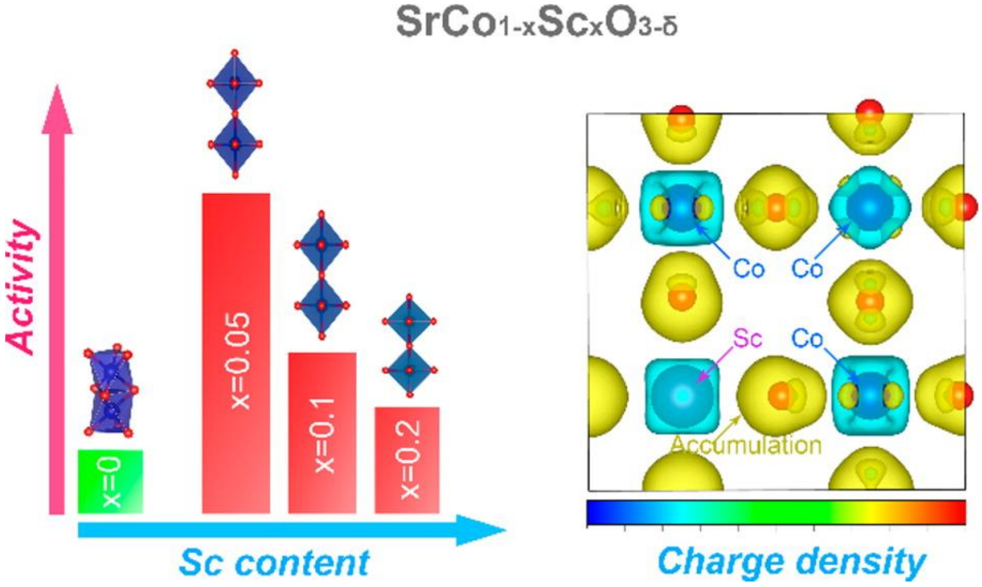

Figure 2.7 OER activity as a function of Sc content.[13]

Changing the composition could induce significant changes in the physical properties of perovskite, including the oxygen non-stoichiometry, cation valence state, structure, surface segregation and etc.[13] The B-site substitution of redox-inactive cation (Sc) in $SrCoO_{3-\delta}$ produces distinctive OER activities (as shown in Figure 2.7).[13] Such compositional engineering helps screen efficient electrocatalysts with an optimum composition.

2.3.1.4 Defect chemistry control

The generated defects in electrocatalysts have been revealed as an influential factor in manipulating the catalytic process and catalytic performance. The dominating defects-driven oxygen reduction has been substantiated in a “pure” carbon (without any elemental doping) catalyst.[14] As shown in Figure 2.8, the catalyst PC-18-950 is a non-nitrogen containing porous carbon prepared from carbonization and removal of the Zn atoms from a Zn metal-organic framework.[14] The porous carbon (PC-18-950) which only contains carbon and oxygen, exhibited a comparable ORR activity to Pt/C.[14] Such finding has pushed the design of defects-containing electrocatalysts.

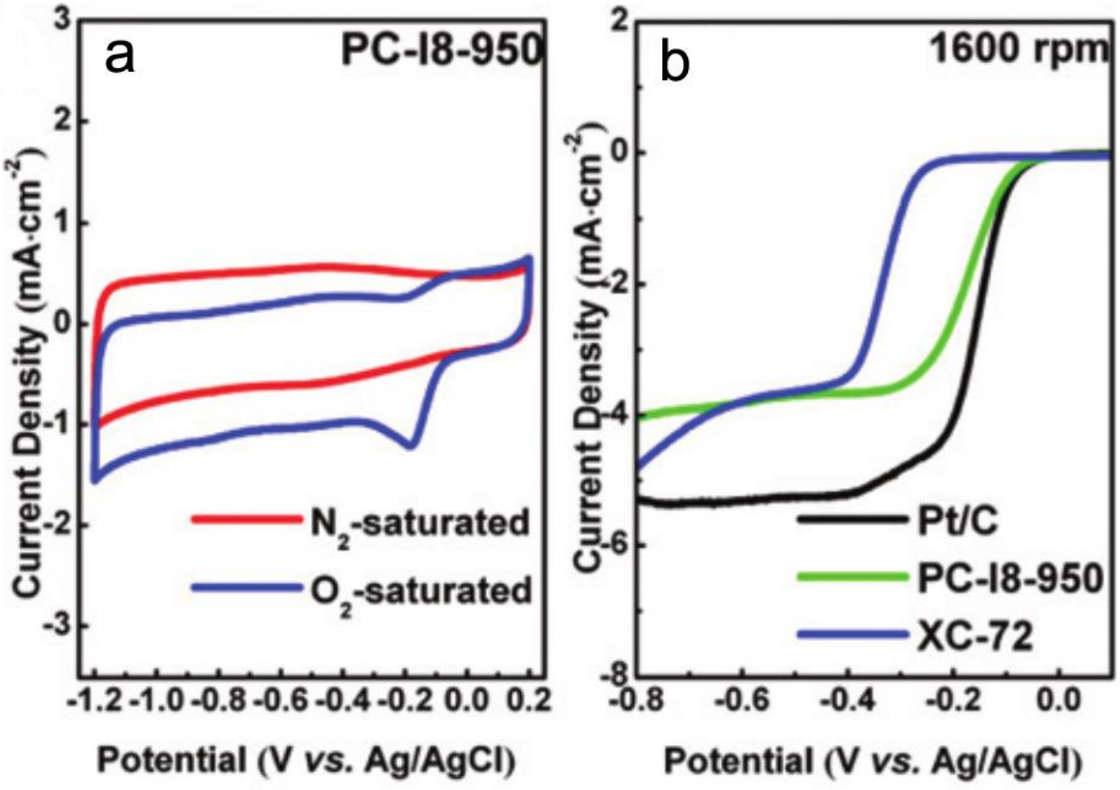

Figure 2.8 (a) CV curves of PC-18-950 specimen in 0.1 M KOH electrolyte. (b) ORR negative scans of XC-72, PC-18-950 and Pt/C catalysts at rotating speed of 1600 rpm.[14]

Deliberately introducing oxygen vacancies in oxide materials is a common practice to regulate oxide electrocatalytic activity and reaction mechanism. Through DFT+U calculation, it is found in MnO_2 that the existence of oxygen vacancy modifies the band gap, Femi level as well as O-O bond length, which in turn governs the kinetics of the catalysis reaction.[27] By tuning the concentration of oxygen vacancy, the oxide catalytic properties can be optimized.[27] There are also concerns over the stability of oxygen vacancies under high oxidative environment (e.g. under OER condition). The high OER activity might not be able to preserve with increasing reaction time owing to the instability of the catalytically critical oxygen vacancies.[28] Researchers found that filling these oxygen vacancies with phosphorus can produce a surprising OER activity.[28] To be specific, through a modified thermal coupled plasma method, a simultaneous filling of the generated oxygen vacancies with phosphorus in Co_3O_4 can be realized.[28] The design of Co_3O_4-based oxide with proper defects chemistry control (Co_3O_4 with oxygen vacancy defects: V_O-Co_3O_4; Co_3O_4 with oxygen vacancies filled by phosphorus: P-Co_3O_4) give significant HER and OER activity promotions (shown in Figure 2.9).[28]

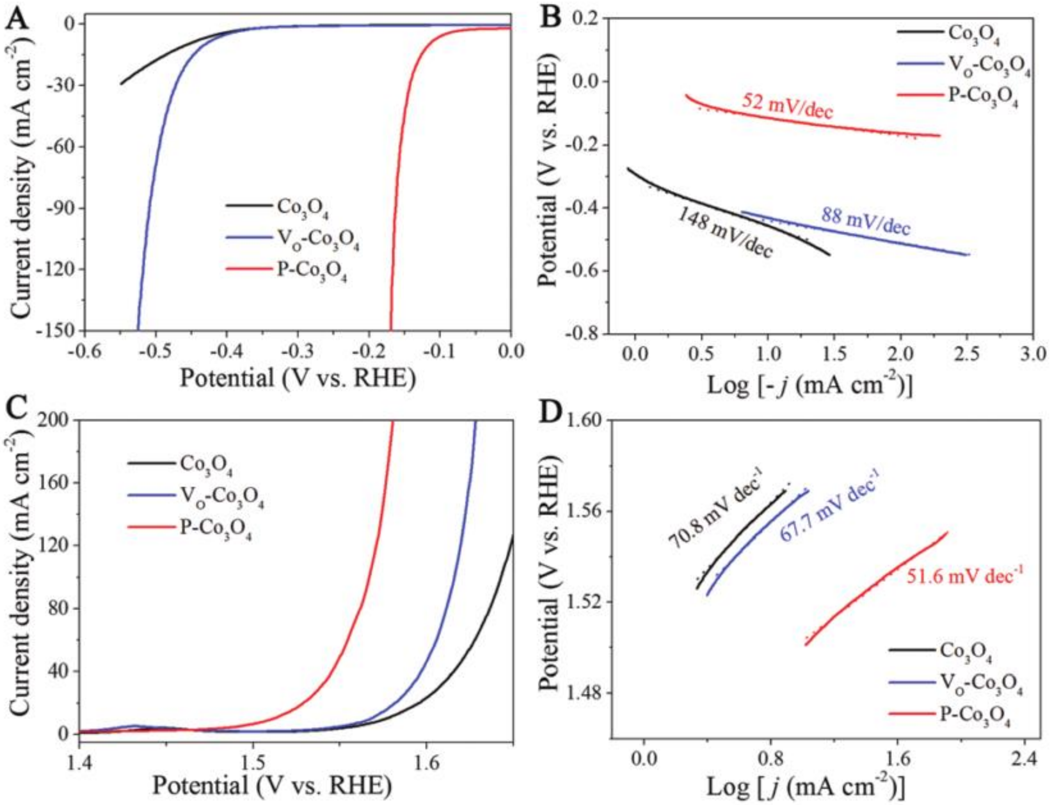

Figure 2.9 (a) The polarization curves and (b) Tafel plot of the pristine Co_3O_4, V_O-Co_3O_4, and the P-Co_3O_4 toward HER in 1 M KOH. (c) The polarization curves and (d) Tafel plot of the pristine Co_3O_4, V_O-Co_3O_4, and the P-Co_3O_4 toward OER in 1 M KOH.[28]

2.3.2 Identifying catalytically-critical parameters

2.3.2.1 Geometric factor

In essence, electrocatalytic reactions on transition metal oxides can be viewed as oxides' orbitals interacting with that of the intermediate oxygen species. Since the metal sites have long been considered as the active center, the transition metal coordination is one of the catalytically influencing factors. Different coordination environment could induce considerable changes to the orbital energy levels and electron filling of the transition metal ion, thereby affecting the activity and stability of the electrocatalysts.[29] The structural flexibility of perovskite allows the fabrication of oxide electrocatalysts with catalytic-active metals (e.g. Co and Mn) subjected to different coordination geometries. As shown in Figure 2.10, the OER of transition metal Co/Mn in tetrahedra (T_d), distorted prisms (P), face-sharing (f-s) octahedra, and corner-sharing (c-s) octahedra arrangements have been systematically investigated.[30] The findings confirm the critical role of transition metal electronic structure which is largely affected by their coordination environment.

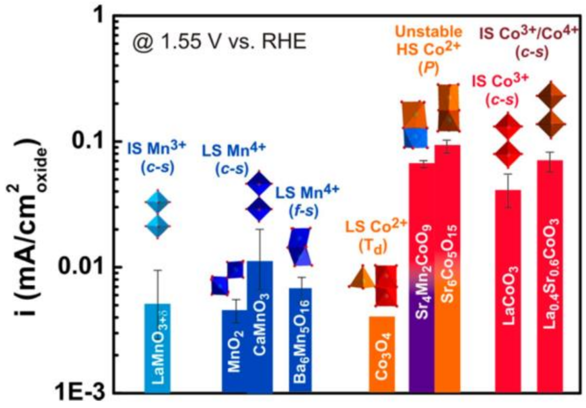

Figure 2.10 OER activity of the various manganese and cobalt oxides with different metal coordination environment.[30]

It is known that spinel oxide contains two different geometric sites: four-oxygen coordinated tetrahedral site (T_d) and six-oxygen coordinated edge-sharing octahedral site (O_h). Identifying the catalytically critical geometry in spinel oxides has generated great interests. It is a general practice to use foreign metal Zn and Al to occupy the tetrahedral site and octahedral site, respectively and to identify the catalytic contribution from each geometric site.[8, 31] The two elements Zn and Al facilitate the design of normal spinel structure and are catalytically inactive. According to literature reports, in spinel structure, the octahedral sites are the main contributor towards oxygen electrocatalysis.[8] In addition, it is found that the octahedral sites tend to expose on the spinel surface.[32]

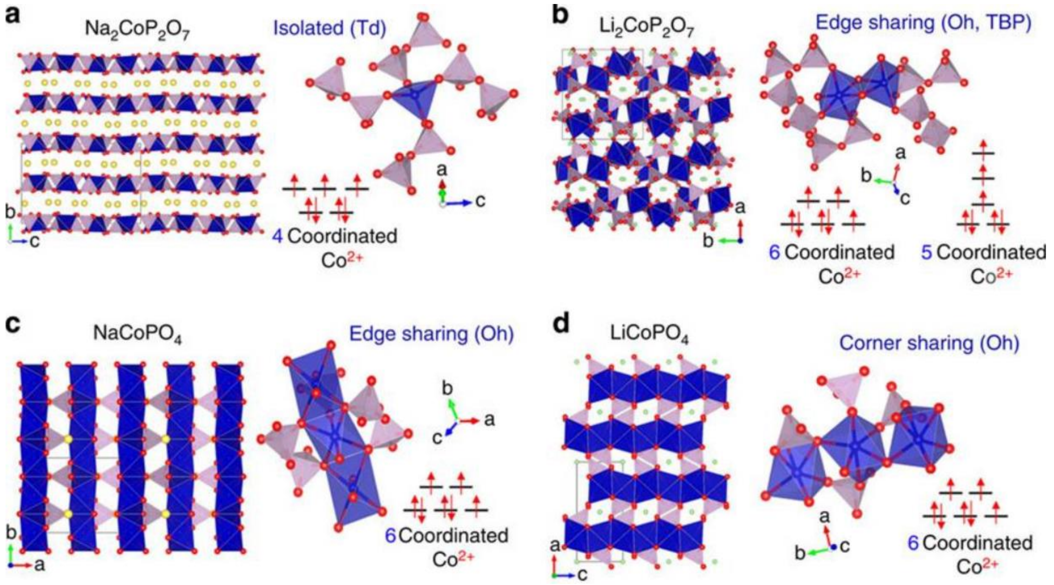

Figure 2.11 crystal structure and cobalt 3d orbital splitting of (a) $Na_2CoP_2O_7$, (b) $Li_2CoP_2O_7$, (c) $NaCoPO_4$ and (d) $LiCoPO_4$.[29]

Some have considered the tetrahedral as less catalytic-critical sites, but several findings demonstrate the distorted tetrahedral can be active as well. One work has proven that the coordination tuning of Co is successful in engineering the water oxidation efficiency of cobalt phosphates.[29] The most active coordination environment for Co was found to be the distorted tetrahedral geometry (shown in Figure 2.11 a).[29] Having open coordination sites, the distorted Co tetrahedra facilitate the binding of oxygen adsorbants and give a low OER overpotential.[29]

2.3.2.2 Valence and spin state

The valence state and spin state codetermines the electronic structure of transition metal cation in oxides and therefore a strong indicator of how the active transition metal center interacts with the adsorbed oxygen.[8] Mn containing oxides are among the most active ORR oxide catalysts and a mixed valence state of Mn^{3+}/Mn^{4+} has been considered as the critical component in producing a high ORR efficiency.[33-34] It is known that many crystals actually contain octahedral geometry and such octahedras have been widely accepted as the catalytic-critical sites in various crystal structures. Under octahedral environment, the 3d electron of transition metal gives t_{2g}-e_g splitting based on crystal field theory. Due to the fact that the e_g orbital directly points to the oxygen ligand and give a high orbital overlap, a strong correlation between the e_g orbital filling and catalytic ORR and OER performance has been established in perovskite family (Figure 2.12).[10, 35] As shown in Figure 2.12 a, the ORR of the various perovskite oxides displays a volcano-shape as a function of the e_g electron of B-site cations.[35] The e_g filling indicates the binding strength between the metallic center and oxygen, thereby acting as a good descriptor for oxygen electrocatalysis.[35]

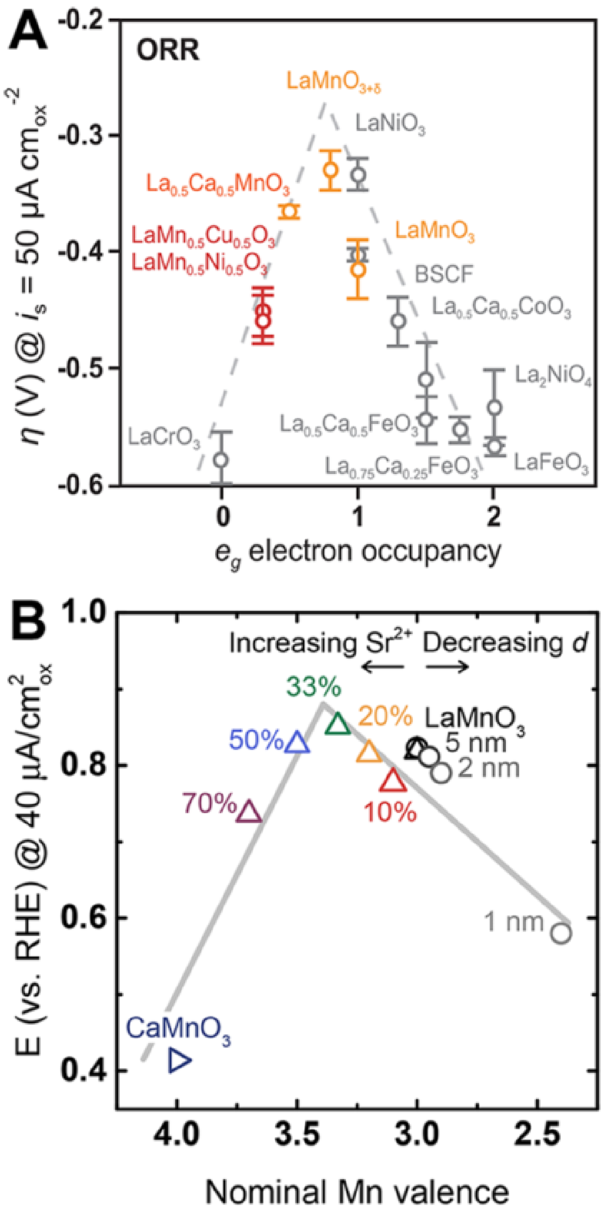

Figure 2.12 (a) The overpotential of ORR as a function of e_g electron number. (b) The ORR activity of $La_{1-x}Sr_xMnO_3$ as a function of nominal Mn valence state.[35]

2.3.2.3 Oxygen p-band center

The effectiveness of oxygen p-band center as activity descriptor can be interpreted from the rigid band model, as illustrated in Figure 2.13.[16] The oxygen electrocatalysis involves the addition and removal of oxygen. More specifically, the addition of oxygen refers to the movement of electrons from the Fermi level to the O p-band and the oxygen removal corresponds to a reverse process (i.e. moving electrons from the O p-band to Fermi level).[16] Since the reaction energies correlate with the interchanged electron numbers between the O p-band and the Fermi level, the important role that O p-band center plays in oxygen electrocatalysis has been rationalized.[16]

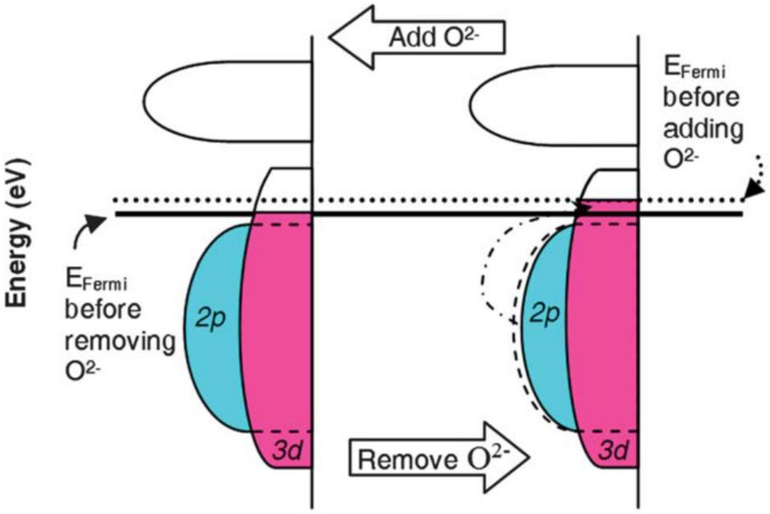

Figure 2.13 Schematic illustration of O p-band center - ORR energetics correlation based on rigid band model.[16]

By employing density functional theory (DFT) modeling, the O p-band center of oxide materials, especially for perovskite family with oxygen deficiency, has been predicted and correlated with electrocatalyst properties including activity and stability.[36-37] For example, the computed O p-band of various Co-based perovskite oxides has been correlated well with their OER activity.[37]

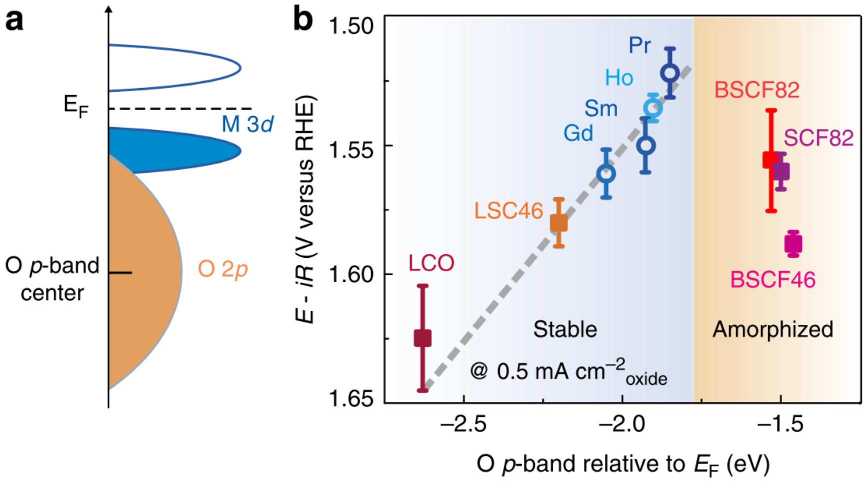

Figure 2.14 (a) Schematic representation of the transition metal oxides band structure and (b)

OER activity of the various Co-based perovskites as a function of the O p-band center relative to Fermi level (eV).[37]

It is found (shown in Figure 2.14 b) that an uplifted O p-band relative to the Fermi level brings a higher OER activity, but with the O p-band too close to the Fermi level, the OER activity is not further promoted and the stability drops dramatically.[37] The instability observed on the right branch (Figure 2.14 b) is due to the rapid surface amorphization and cation leaching as a result of oxygen vacancy formation during electrocatalysis.[37]

2.3.2.4 Metal-oxygen covalency

The metal-oxygen covalency defines the energy gap between the oxygen and metal electrons or the overlap between the metal 3d band and oxygen 2p band.[38] An increased metal-oxygen covalency facilitates the electron transfer between the metal and oxygen and promote the effective interaction between the oxygen adsorbates and active metallic center.[38] Particularly for semimetallic oxides (e.g. $LaMO_3$ (M=Co, Fe, Mn, Cr;), $La_{1-x}Sr_xCoO_{3-\delta}$, $ABaCo_2O_{5+\delta}$ (A =Gd, Sm, Pr;)), an enlarged metal-oxygen covalency generally gives a narrow energy gap between the O p-band and Fermi level (but for semiconducting oxides (e.g. p-type semiconductor), there is no direct correlation between the metal-oxygen covalency and O p-band center).[38] Thus the enlarged metal-oxygen covalency has been considered as the key for increasing the redox activity of oxygen (or the activation of lattice oxygen) in semimetallic perovskite oxides. Recent findings reveal that the increased metal-oxygen covalency facilitate the OER kinetics of oxygen-active electrocatalyst.[15] Hence, the metal-oxygen covalency might bridges the understanding of OER through different reaction mechanisms (i.e. reaction mechanisms either centered on the redox of metal ion or lattice oxygen).

2.3.3 Mechanism understanding

Traditional understanding on electrochemical reactions has been mainly focused on the cation-redox chemistry.[10, 35] It is convinced that the electrocatalytic reactions, including ORR and OER, involve the reduction/oxidation of transition metal cation on the oxide surface.[10, 35] The conventional ORR mechanism involving the four concerted proton-electron transfer on surface metallic center is presented in Figure 2.15 a, and the reverse of ORR is equivalent to the OER cycle. As displayed, the initial state of ORR is the adsorption of OH^- on the oxide surface, followed by the first step O_2^{2-}/OH^- displacement. Then, the reaction further proceeds through the peroxide formation (step 2) and oxide formation (step 3). The final step 4 involves the regeneration of OH^- on oxide surface. The metallic center gets oxidized /reduced during one single cycle. Researchers have found that the redox potential of transition metal ion shows a strong correlation with their OER/ORR activity.[39] As shown in Figure 2.15 b, the Fe^{2+}/Fe^{3+} redox peak position correlates well with the ORR activity of manganese ferrite ($Mn_xFe_{3-x}O_4$). It is also found that the position of Ni redox peaks well describes the OER activity of the various foreign metal-doped nickel hydroxides.[39] The established correlation between the redox potential and ORR/OER has been rationalized by the fact that the redox potential is positively related with the electronegativity of the substituting metal.[39]

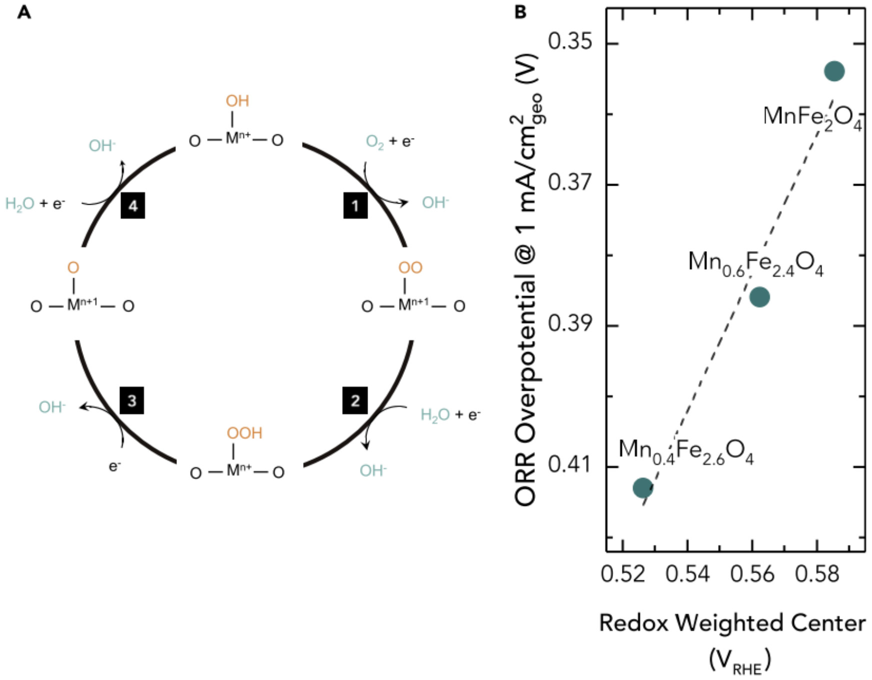

Figure 2.15 (a) Conventional ORR mechanism—centered on the redox chemistry of the metal cation—proposed for transition-metal oxide catalysts. (b) ORR activity of manganese ferrites versus the Fe^{2+}/Fe^{3+} redox center.[39]

The conventional mechanism—centered on the redox chemistry of the metal cation— has been challenged recently.[15, 40-41] The continuous formation and annihilation of oxygen vacancy on the oxygen-deficient oxide surface has been considered favorable in electrochemical reactions that involve the oxygen gas molecules.[42] Oxygen-deficient oxides with significant O p-band character near the Fermi level might exchanges electrons with the oxygen adsorbates (e.g. when oxygen incorporates, the oxygen adsorbates will be reduced and the surface lattice oxygen anion will be oxidized), making the anion-redox an important part in oxygen electrocatalysis.[42] Experimental evidences by operando surface-sensitive XAS technique show that the lattice oxygen anion is a critical redox partner to molecular oxygen, signifying the insufficient understanding of oxygen electrochemical reactions by the conventional surface ionic redox picture.[42] In fact, new OER mechanisms that are fundamentally different from the conventional schemes are being proposed in recent years.[15, 40]

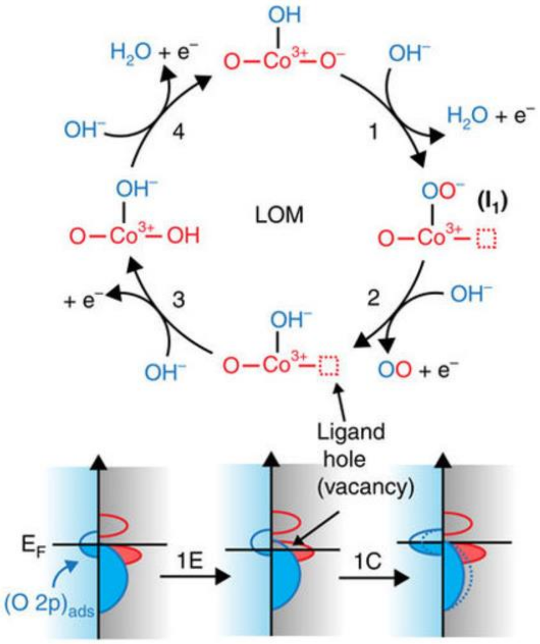

Figure 2.16 Lattice oxygen-mediated mechanism (LOM) proposed for $La_{1-x}Sr_xCoO_{3-\delta}$ towards OER (Lattice and electrolyte species are shown in red and blue, respectively).[40]

A lattice oxygen-mediated mechanism (LOM) has been proposed for oxygen-deficient $La_{1-x}Sr_xCoO_{3-\delta}$ towards water electrolysis.[40] The OER mechanism is shown in Figure 2.16. The metallic Co center does not undergo reduction or oxidation during one single cycle.

Instead, the lattice oxygen exchanges with the adsorbed intermediate, forming oxygen vacancy and producing superoxide ion O_2^-. Experimental evidences also show that the OER is strongly correlated with the oxygen vacancy concentration and oxygen diffusion rate.[40] More recently, researchers show direct experimental evidences for the lattice oxygen participation in $La_{0.5}Sr_{0.5}CoO_{3-\delta}$, $Pr_{0.5}Ba_{0.5}CoO_{3-\delta}$, $SrCoO_{3-\delta}$ oxide and etc.[15] To be specific, the detection of lattice oxygen involvement is assisted by in situ ^{18}O isotope labeling mass spectrometry. Potential non-concerted proton-electron transfer pathways involving the lattice oxygen have been proposed, which greatly enriches the exist understanding of OER.

References

[1] W. T. Hong, M. Risch, K. A. Stoerzinger, A. Grimaud, J. Suntivich, Y. Shao-Horn, *Energy Environ. Sci.* **2015**, 8, 1404-1427.

[2] Y. Lee, J. Suntivich, K. J. May, E. E. Perry, Y. Shao-Horn, *J. Phys. Chem. Lett.* **2012**, 3, 399-404.

[3] R. Frydendal, E. A. Paoli, B. P. Knudsen, B. Wickman, P. Malacrida, I. E. Stephens, I. Chorkendorff, *ChemElectroChem* **2014**, 1, 2075-2081.

[4] C. C. McCrory, S. Jung, J. C. Peters, T. F. Jaramillo, *J. Am. Chem. Soc.* **2013**, 135, 16977-16987.

[5] S. Yagi, I. Yamada, H. Tsukasaki, A. Seno, M. Murakami, H. Fujii, H. Chen, N. Umezawa, H. Abe, N. Nishiyama, *Nat. Commun.* **2015**, 6, 8249.

[6] A. Grimaud, A. Demortière, M. Saubanere, W. Dachraoui, M. Duchamp, M.-L. Doublet, J.-M. Tarascon, *Nat. Energy* **2017**, 2, 16189.

[7] J. T. Mefford, X. Rong, A. M. Abakumov, W. G. Hardin, S. Dai, A. M. Kolpak, K. P. Johnston, K. J. Stevenson, *Nat. Commun.* **2016**, 7, 11053.

[8] C. Wei, Z. Feng, G. G. Scherer, J. Barber, Y. Shao-Horn, Z. J. Xu, *Adv. Mater.* **2017**.

[9] M. Łukaszewski, *Int J Electrochem Sci* **2016**, 4442-4469.

[10] J. Suntivich, K. J. May, H. A.Gasteiger, J. B. Goodenough, Y. Shao-Horn, *Science* **2011**, 334, 1383-1385.

[11] X. Lu, C. Zhao, *Nat. Commun.* **2015**, 6, 6616.

[12] C. Tang, H. F. Wang, X. L. Zhu, B. Q. Li, Q. Zhang, *Part. Part. Syst. Charact.* **2016**, 33, 473-486.

[13] D. Chen, C. Chen, Z. Zhang, Z. M. Baiyee, F. Ciucci, Z. Shao, *ACS Appl Mater Interfaces* **2015**, 7, 8562-8571.

[14] X. Zhao, X. Zou, X. Yan, C. L. Brown, Z. Chen, G. Zhu, X. Yao, *Inorg. Chem. Front.* **2016**, 3, 417-421.

[15] A. Grimaud, O. Diaz-Morales, B. Han, W. T. Hong, Y.-L. Lee, L. Giordano, K. A. Stoerzinger, M. T. Koper, Y. Shao-Horn, *Nat. Chem.* **2017**, 9, 457-465.

[16] Y.-L. Lee, J. Kleis, J. Rossmeisl, Y. Shao-Horn, D. Morgan, *Energy Environ. Sci.* **2011**, 4, 3966.

[17] I. S. Amiinu, Z. Pu, X. Liu, K. A. Owusu, H. G. R. Monestel, F. O. Boakye, H. Zhang, S. Mu, *Adv. Funct. Mater.* **2017**, 27.

[18] Z. Liu, H. Nie, Z. Yang, J. Zhang, Z. Jin, Y. Lu, Z. Xiao, S. Huang, *Nanoscale* **2013**, 5, 3283-3288.

[19] Y. Li, C. Zhao, *ACS Catal.* **2017**, 7, 2535-2541.

[20] W. Tian, H. Li, B. Qin, Y. Xu, Y. Hao, Y. Li, G. Zhang, J. Liu, X. Sun, X. Duan, *J. Mater. Chem. A* **2017**, 5, 7103-7110.

[21] F. Tang, W. Cheng, Y. Huang, H. Su, T. Yao, Q. Liu, J. Liu, F. Hu, Y. Jiang, Z. Sun, *ACS Appl Mater Interfaces* **2017**, 9, 26867-26873.

[22] J. Liu, L. Jiang, B. Zhang, J. Jin, D. S. Su, S. Wang, G. Sun, *ACS Catal.* **2014**, 4, 2998-3001.

[23] Y. Liang, Y. Li, H. Wang, J. Zhou, J. Wang, T. Regier, H. Dai, *Nat. Mater.* **2011**, Vol 10, 780-786.

[24] Y. Liang, H. Wang, J. Zhou, Y. Li, J. Wang, T. Regier, H. Dai, *J. Am. Chem. Soc.* **2012**, 134, 3517-3523.

[25] H. Zhu, S. Zhang, Y. X. Huang, L. Wu, S. Sun, *Nano Lett.* **2013**, 13, 2947-2951.

[26] V. Celorrio, D. Tiwari, D. J. Fermin, *J. Phys. Chem. C* **2016**, 120, 22291-22297.

[27] L. Li, X. Feng, Y. Nie, S. Chen, F. Shi, K. Xiong, W. Ding, X. Qi, J. Hu, Z. Wei, L.-J. Wan, M. Xia, *ACS Catal.* **2015**, 5, 4825-4832.

[28] Z. Xiao, Y. Wang, Y.-C. Huang, Z. Wei, C.-L. Dong, J. Ma, S. Shen, Y. Li, S. Wang, *Energy Environ. Sci.* **2017**, 10, 2563-2569.

[29] H. Kim, J. Park, I. Park, K. Jin, S. E. Jerng, S. H. Kim, K. T. Nam, K. Kang, *Nat. Commun.* **2015**, 6, 8253.

[30] A. Grimaud, C. E. Carlton, M. Risch, W. T. Hong, K. J. May, Y. Shao-Horn, *J. Phys. Chem. C* **2013**, 117, 25926-25932.

[31] P. W. Menezes, A. Indra, A. Bergmann, P. Chernev, C. Walter, H. Dau, P. Strasser, M. Driess, *J. Mater. Chem. A* **2016**, 4, 10014-10022.

[32] J.-P. Jacobs, A. Maltha, J. G. Reintjes, J. Drimal, V. Ponec, H. H. Brongersma, *J Catal* **1994**, 147, 294-300.

[33] K. A. Stoerzinger, M. Risch, B. Han, Y. Shao-Horn, *ACS Catal.* **2015**, 5, 6021-6031.

[34] Q. Tang, L. Jiang, J. Liu, S. Wang, G. Sun, *ACS Catal.* **2014**, 4, 457-463.

[35] J. Suntivich, H. A. Gasteiger, N. Yabuuchi, H. Nakanishi, J. B. Goodenough, Y. Shao-Horn, *Nat Chem* **2011**, 3, 546-550.

[36] B. Han, M. Risch, Y.-L. Lee, C. Ling, H. Jia, Y. Shao-Horn, *Phys. Chem. Chem. Phys.* **2015**, 17, 22576-22580.

[37] A. Grimaud, K. J. May, C. E. Carlton, Y.-L. Lee, M. Risch, W. T. Hong, J. Zhou, Y. Shao-Horn, *Nat. Commun.* **2013**, 4, 2439.

[38] W. T. Hong, K. A. Stoerzinger, Y.-L. Lee, L. Giordano, A. Grimaud, A. M. Johnson, J. Hwang, E. J. Crumlin, W. Yang, Y. Shao-Horn, *Energy Environ. Sci.* **2017**, 10, 2190-2200.

[39] D. A. Kuznetsov, B. Han, Y. Yu, R. R. Rao, J. Hwang, Y. Román-Leshkov, Y. Shao-Horn, *Joule* **2017**, 2.

[40] J. T. Mefford, X. Rong, A. M. Abakumov, W. G. Hardin, S. Dai, A. M. Kolpak, K. P. Johnston, K. J. Stevenson, *Nat Commun* **2016**, 7, 11053.

[41] C. Yang, A. Grimaud, *Catalysts* **2017**, 7, 149.

[42] D. N. Mueller, M. L. Machala, H. Bluhm, W. C. Chueh, *Nat Commun* **2015**, 6, 6097.

Chapter 3

Experimental Methodology

.

Chapter 3 presents the experimental methodologies adopted in this thesis and clarifies their critical role. First, the synthesis method of the spinel oxides and catalyst electrode preparation procedure are described. As ORR exhibits mass transport limitation, the rotating disk electrode technique which facilitate the study of electron-transfer kinetics is demonstrated. Standard testing procedures for ORR and OER are included. As the various material characterization techniques are powerful tools to help reveal the fundamentals behind the catalytic phenomenon, the physical principles and characterization capabilities of each technique are briefly reviewed.

3.1 Rationale for selection

The synthesis of spinel $CoAl_2O_4$, $ZnMn_xCo_{2-x}O_4$ (x=0~2.0) and $ZnFe_xCo_{2-x}O_4$ (x=0~2.0) oxides were through a sol-gel combustion method. The sol-gel combustion synthesis at high temperatures is selected because it can produce high crystallinity and simple morphology. As this work mainly focused on the fundamental understanding of the spinel catalysts, potential influences from the morphology can be minimized through a simple sol-gel combustion synthesis. The synthesis of nano-size spinel oxides was by a facile wet chemical method. The wet chemical method is a well-established method in producing nano-size spherical ferrite particles with a uniform size distribution.

The use of rotating disk electrode method is necessary for investigating the ORR performance because the ORR is a mass-transport limited reaction. By introducing the convection of the electrolyte, the diffusion layer thickness can be fixed. It facilitates the steady-state current. Although there is no mass transportation issue for OER, the RDE system works for it as well. The XRD technique is to examine the crystal phase of the synthesized particles. XAFS technique is to obtain the cation valence state and the distribution of cations between the tetrahedral and octahedral sites in the spinel lattice. XPS aims to acquire the surface composition and cation oxidation state on the near surface. BET method determines the specific surface area of the oxide particles, which enables the extraction of the specific OER or ORR activity. SEM confirms the morphology of the oxide powders and it is an important tool for the identification of morphology effect. The use of TEM technique aims to examine the particle size distribution and catalyst surface change after oxygen electrocatalysis.

3.2 Synthesis

The synthesis of the micro-scale spinel oxides (i.e. $CoAl_2O_4$, $ZnCo_xMn_{2-x}O_4$ (x=0~2.0) and $ZnFe_xCo_{2-x}O_4$ oxides (x=0~2.0)) was by a traditional sol-gel auto combustion method[1] (shown in Figure 3.1) at high temperature and the synthesis of nano-size spinel ferrite oxides was via an established facile chemical method[2] (shown in Figure 3.2).

Synthesis of $CoAl_2O_4$ oxides via a sol-gel auto combustion method at different temperatures. 10 mmol cobalt acetate ($Co(OAc)_2 \cdot 4H_2O$), 20 mmol aluminum nitrate ($Al(NO_3)_3 \cdot 9H_2O$), 60 mmol citric acid and 60 mmol urea were dissolved in 200 mL deionized water with stirring. As the solution turns homogenous, 10 mL of concentrated nitric acid was added. The above mixture solution was constantly stirred and heated at 80°C~100°C until highly viscous gel was formed. The gel was then dried in the oven at 170°C for 12 hours, followed by calcination at different temperatures (400°C, 500°C, 600°C, and 800°C) for 6 hours to yield $CoAl_2O_4$ powders.

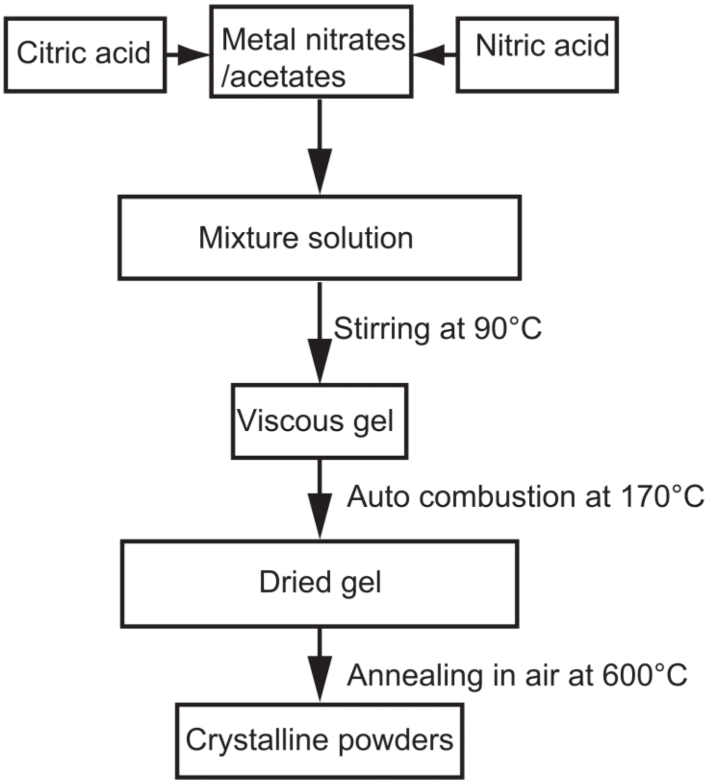

Figure 3.1 Scheme of sol-gel auto combustion method.

Synthesis of $ZnCo_xMn_{2-x}O_4$ oxides (x=0~2.0) via a sol-gel auto combustion method. 2.5 mmol $Zn(CH_3COO)_2 \cdot 2H_2O$ (99.999% trace metals basis, Sigma Aldrich), $(CH_3COO)_3Mn \cdot 2H_2O$ (97%, Sigma Aldrich) and $(CH_3COO)_2Co \cdot 4H_2O$ in total 5 mmol and 15 mmol citric acid (99%, Sigma Aldrich) were dissolved in 30 ml DI water and 2 ml nitric acid by stirring. The molar ratio of $(CH_3COO)_3Mn \cdot 2H_2O$ to $(CH_3COO)_2Co \cdot 4H_2O$ was (2-x) /x. The solution mixture was constantly stirred and heated to 90℃ and maintained at this temperature for several hours until it converted to a viscous gel. Then, the gel was decomposed in an oven at 170 °C for 12 hours to remove the remaining water. The dried-gel was ground thoroughly and annealed in air at 600 ℃ for 6 hours (heating rate:10°C min^{-1}) to obtain pure spinel $ZnCo_xMn_{2-x}O_4$ powder. The sol-gel auto combustion method affords a high yield of 90% ~crystalized particles.

Synthesis of $ZnFe_xCo_{2-x}O_4$ oxides (x=0~2.0) through a sol-gel auto combustion method. Metal acetates/nitrides ($Zn(CH_3COO)_2 \cdot 2H_2O$ (Sigma-Aldrich), $Fe(NO_3)_3 \cdot 9H_2O$ (≥99.95% trace metals basis, Sigma-Aldrich) and $Co(CH_3COO)_2 \cdot 4H_2O$ (99.999% trace metals basis, Sigma-Aldrich)) with a specific molar ratio were first mixed in diluted nitric acid solution through vigorous stirring. Take the synthesis of $ZnFe_{1.4}Co_{0.6}O_4$ as an illustrative example. 2.5 mmol of $Zn(CH_3COO)_2 \cdot 2H_2O$, 1.5 mmol $Co(CH_3COO)_2 \cdot 4H_2O$ and 3.5 mmol $Fe(NO_3)_3 \cdot 9H_2O$ were mixed in diluted nitric acid solution (30 ml deionized water + 2 ml nitric acid) by vigorous stirring. Citric acid (ACS reagent, ≥99.5%, Sigma-Aldrich) (15 mmol) acting as chelating agent, was then added in the mixture. Under constant stirring at 90℃ for several hours, the mixture solution converts into viscous gel. The gel was then decomposed in air at 170℃ (a heating rate of 10℃ min^{-1} to 170℃) for 12 hours to remove the remaining water and ground thoroughly. After applying a further heat treatment in air at 600℃ (a heating rate of 5℃ min^{-1} to 600℃) for 6 hours, phase pure spinel oxide particles were obtained.

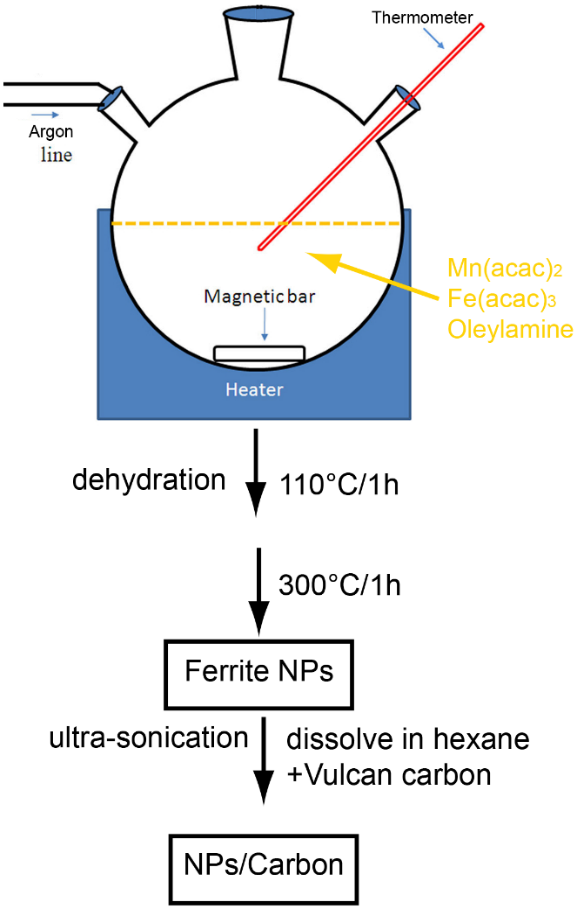

Figure 3.2 Schematic illustration of manganese ferrite nano-particle synthesis through a facile chemical method.

Synthesis of nano-scale spinel $Mn_xFe_{3-x}O_4$ oxides via a facile wet chemical method. Manganese ferrite nanoparticles were prepared according to an established facile wet chemical method.[2] Specifically, the synthesis started with dissolving $Mn(acac)_2$ (technical grade, Sigma-Aldrich) and $Fe(acac)_3$ (≥99.9% trace metals basis, Sigma-Aldrich) with a molar ratio of x: (3-x) in oleylamine (technical grade, 70%, Sigma-Aldrich). Then the mixture was dehydrated at 110°C for 1 hour, and then quickly heated to 300°C (heating rate: ~13°C min^{-1}) and aged at this temperature for an additional 1 hour under vigorous stirring in Argon atmosphere. After cooling, the resulting nanoparticles were first precipitated by centrifugation with addition of isopropanol (≥99.7%). And then re-dispersed in hexane (≥99.0%) and repeated centrifugation by adding isopropanol. The as-prepared nanoparticles were finally kept in hexane for further usage. The as-prepared ferrites have surfactant on the particle surface and need to be heat-treated at 250 °C in air to remove the surfactant. The ferrite nanoparticles could severely aggregate during heat treatment. It is therefore a common practice to load the nanoparticles onto the Vulcan carbon support before surfactant removal.

3.3 Electrode preparation

Oxide electrode was fabricated by drop-casting catalysts onto a rotating disk electrode (RDE). The metal oxide forms a homogeneous thin film covered on the glassy carbon electrode (shown in Figure 3.3).

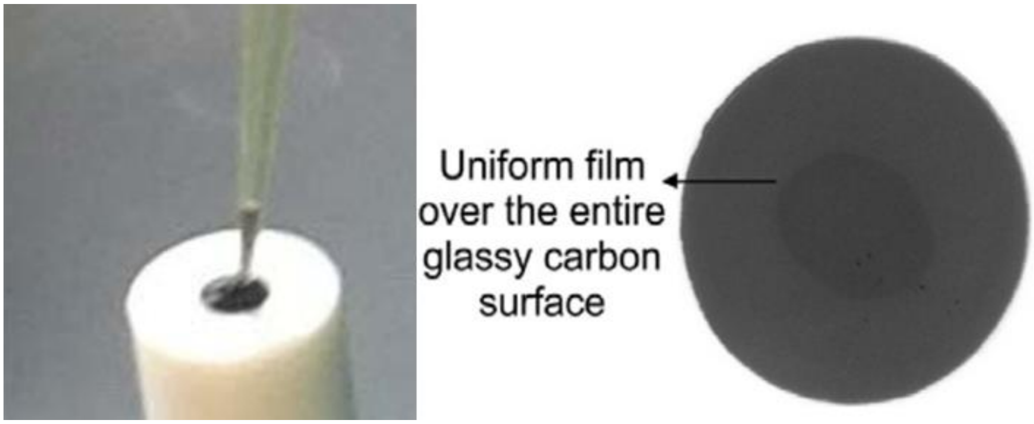

Figure 3.3 Illustration of drop-casting method and uniform thin film on the RDE.

The catalysts ink was prepared by ultra-sonicating the spinel oxide powders, acid-treated acetylene black (AB), Nafion® perfluorinated resin solution (5 wt% in water) in solution mixture containing water and isopropanol (volume ratio of Nafion® perfluorinated resin solution /water/isopropanol=0.05/4/1). The ink concentrations used were 5mg $m^{-1}{}_{ox}$, and 1mg $ml^{-1}{}_{AB}$. 10 μl of the ink was dropped on the RDE, yielding a final mass loading of 255 μg_{ox} $cm^{-2}{}_{disk}$ and 51μg_{AB} $cm^{-2}{}_{disk}$. To examine the catalytic contribution from acid-treated AB, catalyst ink (1mg $ml^{-1}{}_{AB}$) containing pure acid-treated AB was prepared and dropped on RDE to yield a final mass loading of 51μg_{AB} $cm^{-2}{}_{disk}$. Before drop casting catalysts onto RDE, the RDE electrode was polished for 15~30 minutes using alumina slurry and cleaned by repeated ultrasonication in ethanol and DI water.

3.4 Electrochemical characterization

3.4.1 Rotating disk electrode method

As shown in Figure 3.4, the critical part of RDE apparatus is the convection of the electrolyte. The spinning RDE drags the electrolyte to the disk surface and flings the old solution outwards by a centrifugal force (i.e. the disk surface is always replenished by a flow of electrolyte).

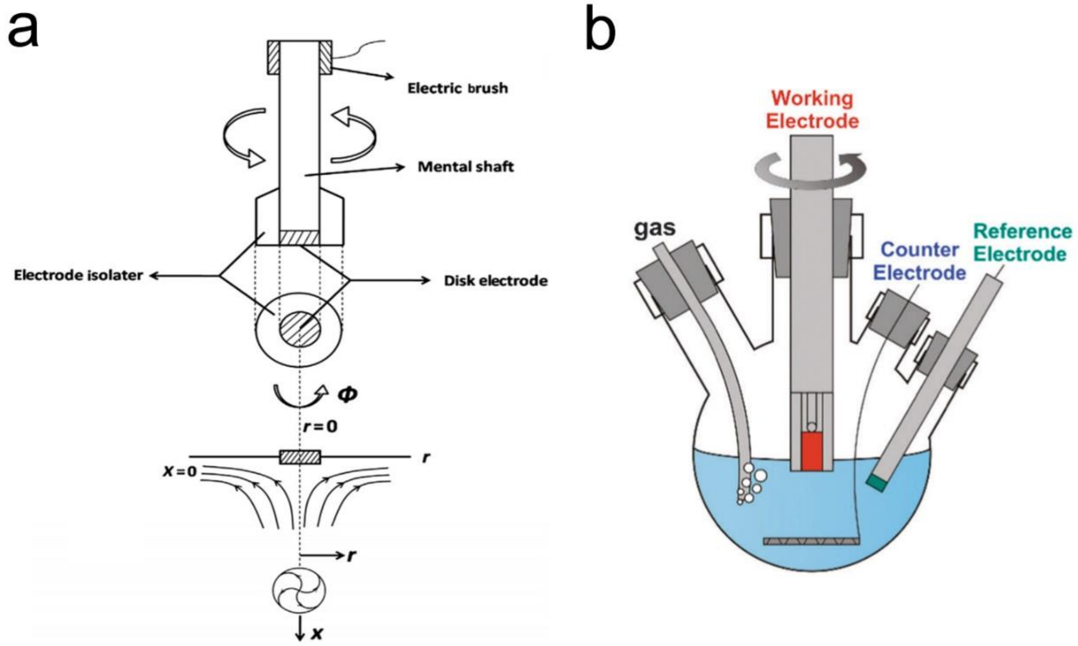

Figure 3.4 (a) Schematic of rotating disk electrode system (b) Set up of the three-electrode system.[3]

The convection helps create a fixed diffusion layer thickness near the electrode surface, thus producing a steady-state current density.[3] In the absence of convection, the diffusion layer near the electrode surface will get thicker with increasing the reaction time, leading to a nonsteady-state current density.[3] The rotating disk electrode technique is particularly indispensable for the ORR ($O_2 + 2\ H_2O + 4\ e^- \rightarrow 4\ OH^-$ in alkaline solution) because it is a reaction controlled by mass transfer. By increasing the rotating speed, the convection velocity of the electrolyte increases, as a result, the diffusion layer becomes thinner. The

RDE technique can facilitate a fast mass transport rate than that of the traditional stationary setup, thereby allowing a close examination of the charge-transfer kinetics even there is a limited mass transport for a reaction. The famous Koutecky-Levich Equation reveals the current-potential relationship on the RDE and limiting current expression:[3]

$$\frac{1}{i} = \frac{1}{i_k} + \frac{1}{i_l} = \frac{1}{i_k} + \frac{1}{0.62nFD_0^{2/3}\omega^{1/2}v^{-1/6}C_0^0}$$

where i_k is the kinetic current, i_l is the limiting current. The parameter n is the electron transfer number, F is the Faraday's constant, D_0 is the diffusivity of O_2 in the electrolyte. ω , v and C_O are the rotating speed, kinetic viscosity and concentration of O_2 in electrolyte, respectively.

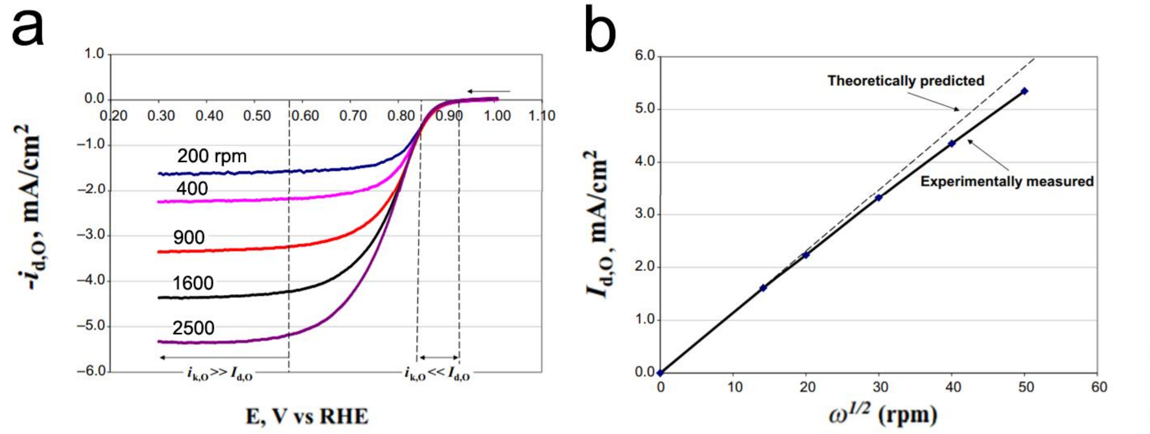

Figure 3.5 (a) Representative ORR polarization curve (negative-going scan) at different rotating speed. (b) The Koutecky-Levich plot.[3]

The representative ORR curve is shown in Figure 3.5 a. At the onset potential range (e.g. 0.92~0.85 V vs RHE), the electron-transfer rate cannot catch up with the diffusion-convection rate brought by the high rotating speed. As a result, the current is purely controlled by the electron-transfer kinetic. At high overpotential range, the electron-transfer kinetics of oxygen reduction is ultra-fast. Under this condition, the diffusion-convection process can no longer catch up with the electron-transfer rate (i.e. the oxidant concentration at the electrode surface will be exhausted to zero) and the reaction is limited by the diffusion. Since the limiting current density is expressed as a function of RDE rotating speed, by plotting the relationship of limiting current versus $\omega^{1/2}$, the electron transfer number can be evaluated according to the following equation:[3]

$$Slope = (0.62nFD_0^{2/3}v^{-1/6}C_0^0)^{-1}$$

3.4.2 Rotating ring-disk electrode method

Just like the RDE method described above, the rotating ring-disk electrode (RRDE) system is set into rotation during ORR measurements. As illustrated in Figure 3.6, the RRDE consists of a central glassy carbon disk electrode, a ring electrode and an insulating barrier in between.

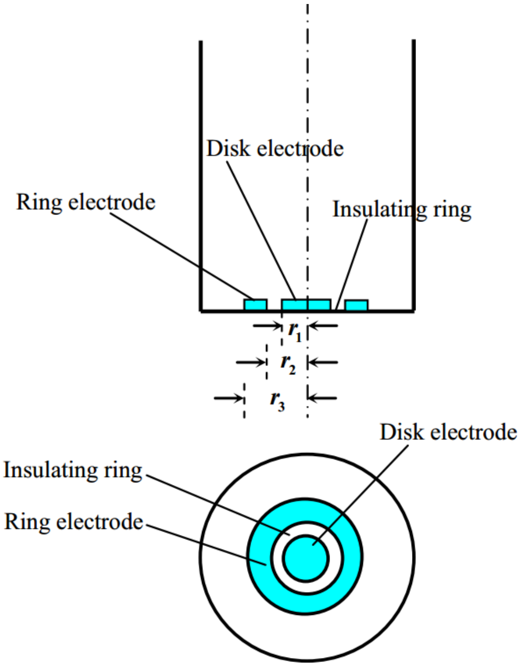

Figure 3.6 Schematic illustration of a rotating ring-disk electrode.[3]

During electrochemical measurements, the disk electrode is independent of the ring electrode. The ORR takes place on the catalyst-decorated disk electrode and generate intermediates (e.g. peroxide) throwing into the bulk solution or reaching the ring electrode surface. The unique advantage of RRDE is that the produced ORR intermediates can be detected by the ring disk. More specifically, the reaction intermediates released from the disk electrode will be electrochemically oxidized or reduced on the ring electrode surface,[3] depending on the potentials applied on the ring electrode. The reactions happen on the ring electrode produce ring currents from which the amount of ORR intermediates can be quantified. The percentage of disk reaction intermediates reach the ring electrode surface can be obtained from an important parameter: the collection efficiency of RRDE. The collection efficiency depends on the thickness of the insulating ring as well as the geometric sizes of ring and disk electrode. The commercially available RRDE generally has a collection efficiency of 20 ~ 40%.

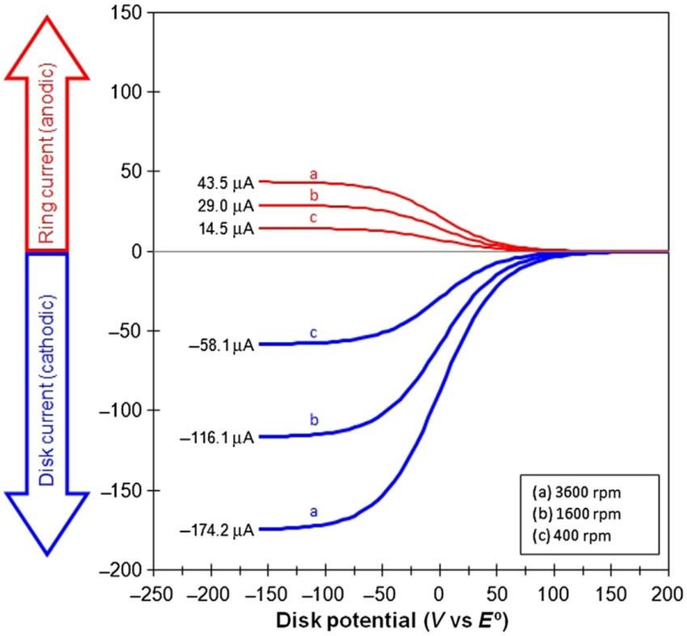

Figure 3.7 Linear sweep voltammetry curves recorded on RRDE in O_2-free 1.0 M KNO_3 + 0.01 M $[Fe(III)(CN)_6]^{3-}$ aqueous solution at a scan rate of 50 mV s^{-1} with applying a ring potential of 0.361 vs. SHE.[3]

The collection efficiency of RRDE can be calibrated experimentally based on the well-known reversible reaction of ferricyanide/ferrocyanide ($[Fe(III)(CN)_6]^{3-}/[Fe(III)(CN)_6]^{4-}$).[3] During RRDE measurements, the reduction of ferricyanide to ferrocyanide happens at the disk electrode surface and only a fraction of ferrocyanide can be collected by the ring electrode and be subsequently oxidized at the ring electrode surface. Thus, the collection efficiency (N) of RRDE can be calculated by the following equation:[3]

$$N = \left| \frac{I_r, [Fe(II)CN]^{4-}}{-I_d, [Fe(III)CN]^{3-}} \right|$$

where I_r is the ring current and I_d is the disk current, as can be observed in Figure 3.7. The RRDE method enables the detection of reaction intermediates and facilitate the electron transfer studies on ORR.

3.4.3 Oxygen electrocatalysis characterization

The ORR and OER are performed on a standard three-electrode setup shown in Figure 3.4 b using a PINE WaveDriver 20 bipotentiostat. To be specific, the catalyst-decorated RDE/RRDE is the working electrode. Pt wire and saturated calomel electrode (SCE) act as the counter and reference electrode, respectively. The potential is imposed between the working and reference electrode and the recorded current is collected between working and counter electrode. The oxide catalysts are investigated in alkaline solution for their ORR and OER. This is because alkaline is a safe environment for oxide materials. Prior to the ORR measurements, the catalysts are scanned in Ar-saturated 0.1 M KOH electrolyte at a scan rate of 10 mV $^{-1}$ for background correction purpose. The catalysts are examined in a new batch of O_2-saturated KOH electrolyte for ORR. As O_2 is the reactant for ORR (O_2 + 2 H_2O + 4 $e^- \rightarrow$ 4 OH^- in alkaline solution), an O_2 flow is continuously supplied during the ORR measurements. The ORR CV profiles are recorded within a potential window of 1.0 V~0.4 V (vs. RHE) at different rotating speeds (100 rpm, 400 rpm, 900 rpm, 1600 rpm, and 2500 rpm) with a scan rate of 10 mV $^{-1}$. The ORR CV profiles collected at a rotating speed of 1600 rpm is used to extract the ORR specific activity. As for RRDE measurements, the collection efficiency of RRDE is determined before ORR tests. The OER test is conducted in O_2-saturated 0.1 M KOH electrolyte at a rotating speed of 1600 rpm with a scan rate of 10 mV $^{-1}$. For pH dependence examination purpose, the concentration of the KOH electrolyte varies from to 0.03 M to 1 M, corresponding to a pH range of 12.5 ~14.0. The electrolyte resistance is measured right after each ORR or OER test.

3.4.4 Electrochemical data analysis

The oxide catalysts' ORR and OER performance are presented by their specific activity. The ORR activity is extracted from the negative-going polarization curves in O_2-saturated 0.1 M KOH solution at a scan rate of 10 mV s^{-1} with a rotating speed of 1600 rpm. The capacitance is first corrected by subtracting the current of positive-going scans in Ar saturation from that in O_2 saturation. The mass transport correction is performed to extract the kinetic current by employing the well-known Levich equation:[3]

$$i^{-1} = {i_k}^{-1} + {i_l}^{-1}$$

where i is the measured O_2 reduction current density, i_k is the mass-transport-corrected kinetic ORR current density, and i_l represents the limiting current density. The obtained ORR kinetic current is further normalized to the oxide surface area to get the specific current density.

The iR-corrected potential, $E_{iR-corrected}$, is calculated by the following equation:[4]

$$E_{iR-corrected} = E_{applied} - iR$$

where i is the ORR current in O_2-saturated electrolyte and R is the uncompensated ohmic electrolyte resistance (~45Ω; 0.1 M KOH) measured via high frequency ac impedence in O_2-saturated 0.1 M KOH. The iR-corrected potential, plotted as a function of the specific current density (kinetic current) gives the final Tafel plots.

The OER activity is extracted from the OER CV profiles at different electrolyte pH. The capacitance is corrected by averaging the forward and backward current. The current is normalized to the oxide surface area and iR-corrected electrode potential is obtained.[4]

3.5 Material characterization

X-ray diffraction (XRD). X-rays is the electromagnetic radiation having a wavelength ranging from 10 nm to 10^{-3} nm. Due to the fact that the X-rays have much shorter wavelength than the visible light, the X-rays are powerful tools for analyzing the crystal structure of materials. The diffraction phenomenon of waves had been well known before the discovery of X-rays. For instance, visible light will gets diffracted whenever it encounters periodic structures having a period of the same order of magnitude as the incident light wavelength. It is proposed by von Laue in 1912 that the X-rays can be diffracted by periodically arranged atoms if the X-rays have wavelengths similar to that of the atomic spacing within the crystal lattice. It is known that a crystalline matter contains atomic layers with different orientation and lattice spacing. Thus, each of these atomic planes can act as an effective grating when X-rays interact with the crystalline matter.

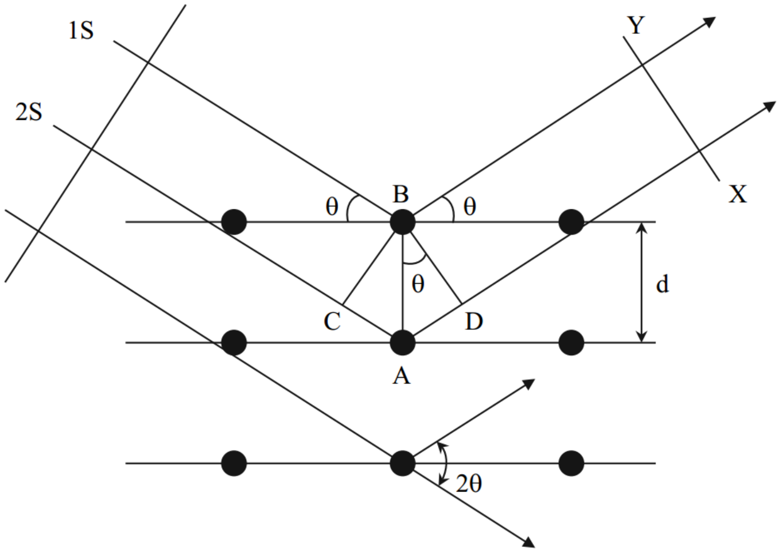

Figure 3.8 Diffraction of X-rays by crystalline matter.[5]

In the same year of 1912, a much simpler mathematical form (Bragg law, see the following equation) has been proposed by British physicists for expressing the condition of X-ray diffraction:[5]

$$n\lambda = 2d\sin\theta$$

where λ is the wavelength of the X-ray, n is the order of reflection, d is the lattice spacing, θ is the incidence angle. In general, the diffracted beam is considered as a reflection of the incident beam by various lattice planes (In essence, it is the X-ray scattered by the atoms in all the crystal planes). As shown in Figure 3.8, when X-ray 1S and 2S reflect, constructive interference will be resulted as long as the two X-ray travel a total distance that differs by a whole number multiple of their wavelength and generate a diffracted beam in a given direction. In both optical reflection and Bragg reflection, the angle of incidence equals to that of the reflection. While the optical reflection can take place at any incidence angles, the Bragg reflection of X-rays only occurs at specific angles when the Bragg law is satisfied.

Since the 002 and 004 reflections are equivalent to the 2nd and 4th-order reflections from the (001) crystal planes, respectively, the reflections are generally viewed by their first-order one.[5] Therefore, the Bragg law (i.e. the following equation) is dominantly used in XRD.[5-6]

$$\lambda = 2d\sin\theta$$

At any detectable angles, the condition for diffraction is d > λ/2. The essential components of diffractometer (Figure 3.9) include X-ray source, sample holder and a detector measuring the intensity of the diffracted beam. In the most common θ-2θ scan, the angle between the sample surface and the incident X-ray is fixed at half the diffraction angle 2θ.

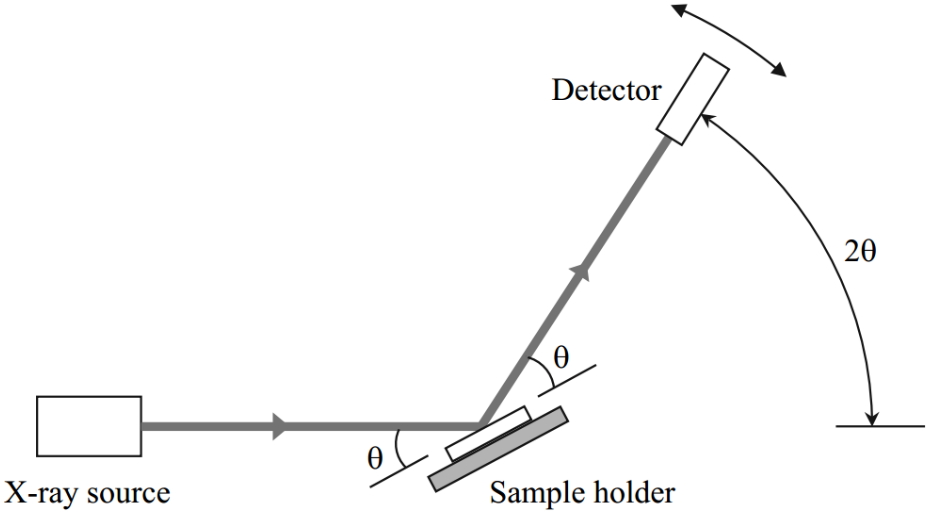

Figure 3.9 Essential component of typical diffractometer.

X-ray Absorption Fine Structure (XAFS). X-ray Absorption Fine Structure (XAFS) is a widely used technique that examines how X-rays are being absorbed by the specimen at energies near or above the discrete core-electron binding energies of the atom.[7]

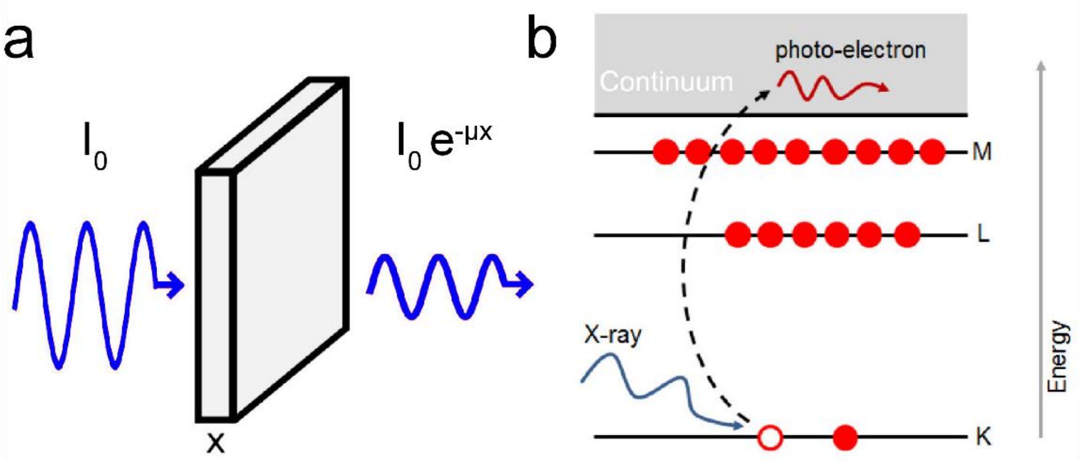

Figure 3.10 (a) Illustration of XAFS measurements. A beam of X-rays (intensity I_0) passes through a homogeneous sample (thickness x) and loses certain intensity due to the interaction. The transmitted X-ray intensity is measured to give the absorption coefficient μ.[7]

The light source is synchrotron radiation-produced high-intensity continuous X-ray. As shown in Figure 3.10, dramatic absorption occurs when the X-ray energy is equal to the core-electron binding energy and the core-level electrons get excited into the continuum.[7-8] The core-electron binding energy is dependent on the quantum number (n) of electrons in a specific atom orbitals and the element atomic number. The core-electron binding energy decreases with an increase of quantum number, i.e. B.E.K shell > B.E.L shell > B.E.M shell. Since each shell (n=1, 2, 3 …) has distinct core-electron binding energy, the absorption spectrum for any element resembles the representative X-ray absorption spectrum of Pb (Figure 3.11).[8]

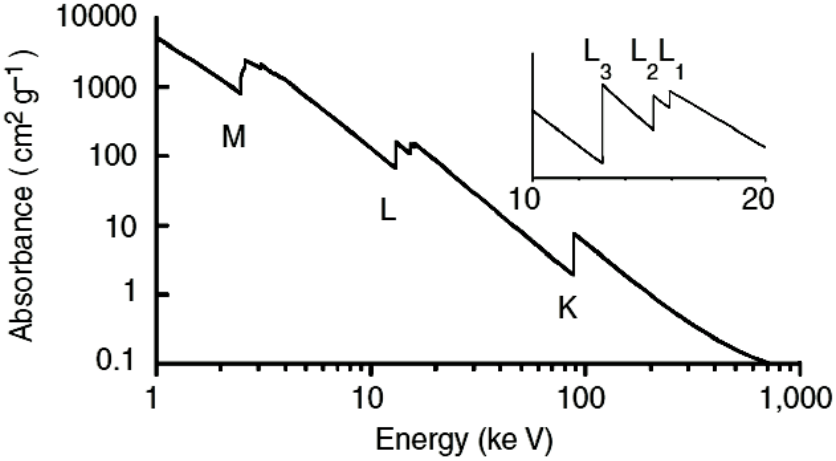

Figure 3.11 Illustration of representative X-ray absorption spectroscopy. Three absorption edges can be observed (K, L, and M edges), corresponding to the electron emission from K, L, M shells, respectively.[7]

The core-electron binding energy also correlates positively with the atomic number, for example, ranging from 7112 eV for Fe (Z=26) K-edge to 115606 eV for U (Uranium, Z=92) K-edge.[7] Therefore, the XAFS is element-specific and one can tune the energy range of X-ray to examine the specific element and edge (e.g. K-edge or L-edge). The near edge region is generally referred to as X-ray absorption near-edge structure (XANES). A comparative analysis of the absorption edge energies with that of reference oxide allows the determination of absorbing atom oxidation state. The oscillations extend up to ~1000 eV above the near edge region are referred to as extended X-ray absorption fine structure (EXAFS).[8] At these energies, the photoelectron generated has a relatively higher energy of

$E-E_0$ (E is the absorbed X-ray photon energy, E_0 is the core-electron binding energy). The wavelength (λ_e) of the photoelectron, given by the following equation, is comparable to the interatomic distances.[7]

$$\lambda_e = h/\sqrt{2m_e(E-E_0)}$$

where m_e is the mass of the electron.

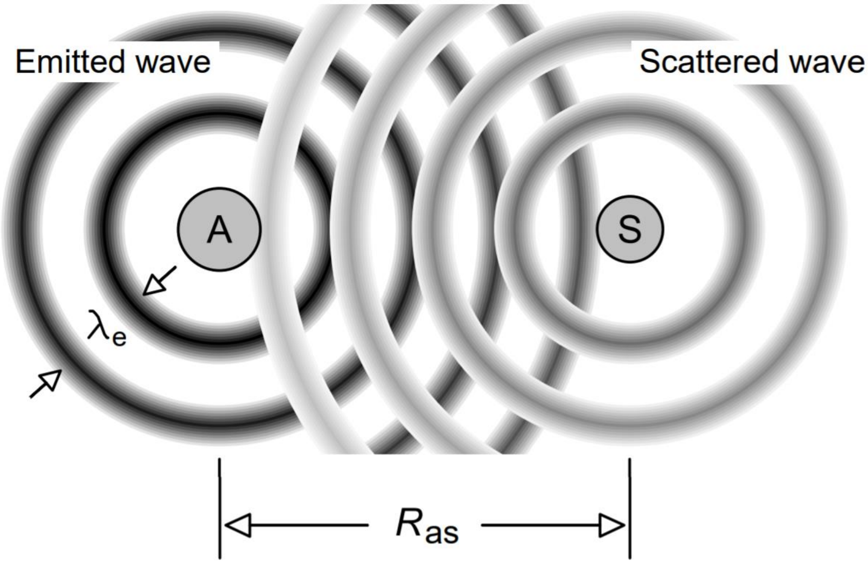

Figure 3.12 Illustration of the single scattering. The photoelectron emitted from the absorbing atom (A) is back-scattered by a single scattering atom (S). The final-state wave function at the absorber is modified by the back-scattered wave. If the back-scattered and out-going waves are in phase, there will be constructive interference and the wave function increases. If the back-scattered and out-going waves are out of phase, it gives destructive interference and decreased wave function. Ras is the distance between the absorbing and scattering atom.[8]

Figure 3.12 illustrate the single scattering pathway. A photoelectron wave is scattered by a single scattering atom before returning to the absorbing atom. Actually, the scattering pathway can be more complicated. The photoelectron ejected can be scattered by more atoms before returning to the absorbing atom. This is described as multi-scattering (e.g. absorber→scatterer 1→scatterer 2→scatterer 1→absorber). Failures to take multi-scattering into account leads to significant errors in the subsequent determination of coordination number or bond length.[8] The EXAFS ($\chi(\mu)$) is typically defined as the modulation of the absorption rate normalized to the background absorption:[8]

$$\chi(E) = \frac{\mu(E) - \mu_0(\mathrm{E})}{\mu_0(E)}$$

where μ is the observed adsorption coefficient and μ_0 is the background absorption.

The $\chi(E)$ in E space has to be converted to $\chi(k)$ in the k space in order to correlated EXAFS to structure parameter. For better visualize the information given by the EXAFS spectrum, Fourier transformation is generally employed to decompose the k-space signal into R-space signal, which allow a qualitative understanding of a substance. The Fourier transform (FT) technique gives a scattering profile as a function of the absorber-neighboring atom radial distance.[7-8] The FT peak size are associated with the neighboring atom type and number.

X-ray photoelectron spectroscopy (XPS). XPS is one of the most heavily used electron spectroscopies owing to its capabilities in extracting surface-sensitive information. The XPS technique allows an identification of the elemental composition in the near-surface (≤ 10 nm). In addition, the chemical environment of the element can be revealed from the XPS. The physical basis of XPS technique is the photoelectric effect. The photoelectric effect describes a simple process in which the initially bound core-level electrons are ejected by incoming photons[9] (as shown in Figure 3.13). The electrons emitted in such manner are photoelectrons. The emission of electron happens when the energy of incoming photon is sufficient.

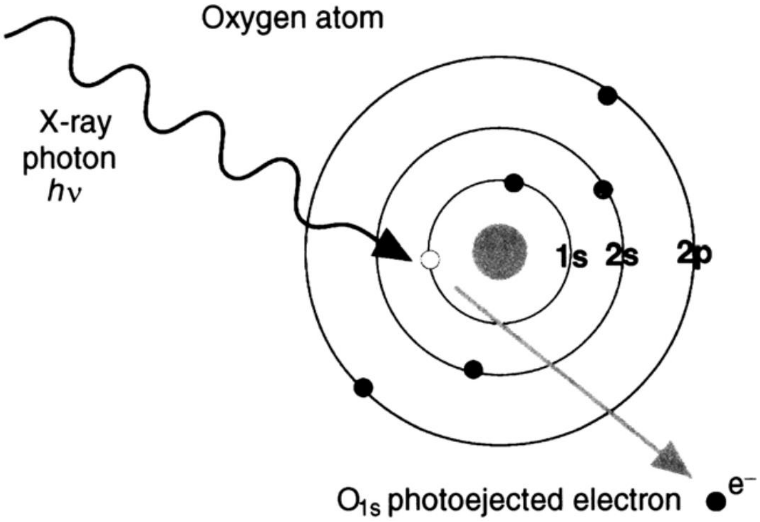

Figure 3.13 Illustration of photoelectron generations.

In XPS measurements, an incident X-rays (e.g. Mg or Al Kα radiation) strikes the sample surface and an electron energy analyzer filters the emitted photoelectron kinetic energy K.E. The derived binding energy B.E. from the following equation is used to construct the energy spectrum because the B.E. is independent of the X-ray energy, whereas the K.E. is not.[9-10]

$$\text{K. E.} = E_{Photon} - B.E. - \emptyset$$

where $\emptyset$ is the work function of the instrument, E_{Photon} is the initial energy of the incoming photon. The correction of work function is needed because the B.E. refers to the B.E. with respect to the Fermi-level instead of the vacuum level. In the produced XPS spectrum of a specific element, there will be characteristic binding energies associated with different core electron orbital. Figure 3.14 shows the characteristic binding energies of U (Uranium).

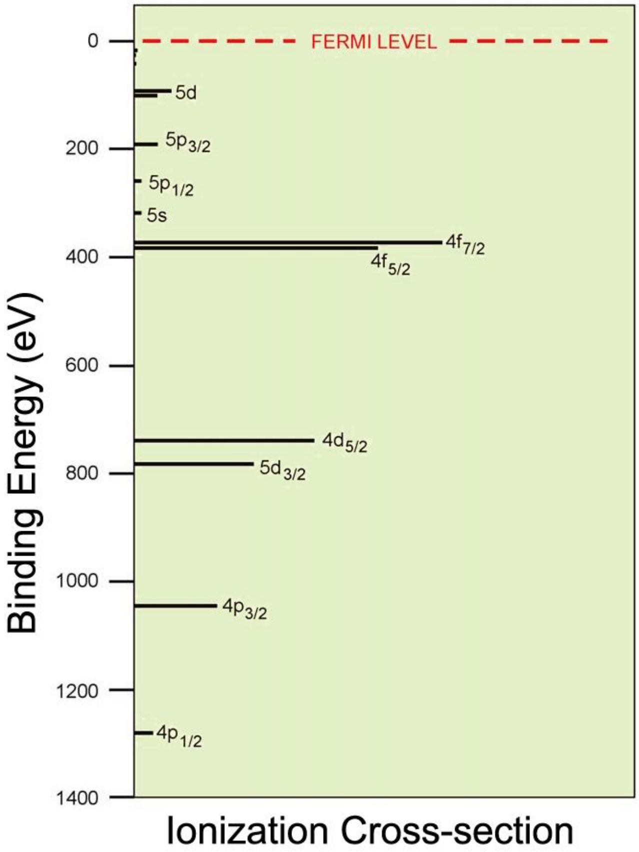

Figure 3.14 The binding energies and ionization cross-section of Uranium.

The peak notations nl_j (e.g. $4p_{3/2}$ in Figure 3.14) used in the XPS spectrum correspond to the principal quantum number (n), angular momentum quantum number (l) and L-S coupling (j = l + s).[10] The s refers to the spin angular momentum number and can be 1/2 and -1/2. All the orbital levels except the s orbitals (l = 0) produce spin-orbital splitting and give doublet peaks (e.g. $4p_{1/2}$, $4p_{3/2}$; $4f_{5/2}$, $4f_{7/2}$) at different binding energies. The binding energy of a core electron is sensitive to the chemical bonding of the element. For a specific element, its metal form and oxide form have different binding energies. Withdrawal of valence electrons from the nucleus increases the core electron binding energy.[10] In contrast, the donation of valence electron charge brings the core electron binding energy down. Such chemical shift in XPS spectrum allows the determination of the metal oxidation state. By fitting the XPS spectrum, a more quantified information about the oxidation state can be obtained. It is known that the penetration depth of X-rays can reach micrometers, however, the generated photon electrons situated at a depth greater than 10 nm below the sample surface will lose energy and give no contribution to the XPS signals.[9] Therefore, the discrete signals on the XPS spectra are from the near-surface region only. And, it explains the surface sensitivity of this characterization technique.

Brunauer-Emmett-Teller (BET). The BET theory is an extension of the Langmuir theory (Langmuir theory specifically deals with monolayer molecular adsorption) to multilayer molecular adsorption[11] (shown in Figure 3.15). There are several assumptions under BET analysis.[11] First, it is the homogeneous surface assumption. This means that the adsorption takes place equally across the samples surface and there are no preferable sites. The second assumption is the limited molecular interaction. A molecule adsorbed on the surface act as a sorption site for another gas molecule. The inter-molecular interactions are not considered during BET analysis. In addition, it is assumed that the same energy is required for the adsorption of each single molecular layer. For the surface adsorption layer, the adsorption energy is equal to the heat of adsorption. While for the subsequent layers, the energy required for adsorption is equal to the heat of condensation because these layers are treated as a condensed liquid. Local equilibrium is also assumed in BET theory. The uppermost layer is in equilibrium with the gas phase, and the adsorption and desorption rate maintains the same. The last assumption is infinite adsorption at saturation. One the saturation pressure (p_0) is reached (increase of pressure increases the adsorption), it is considered that the solid surface is totally surrounded by condensed liquid-phase adsorbent.

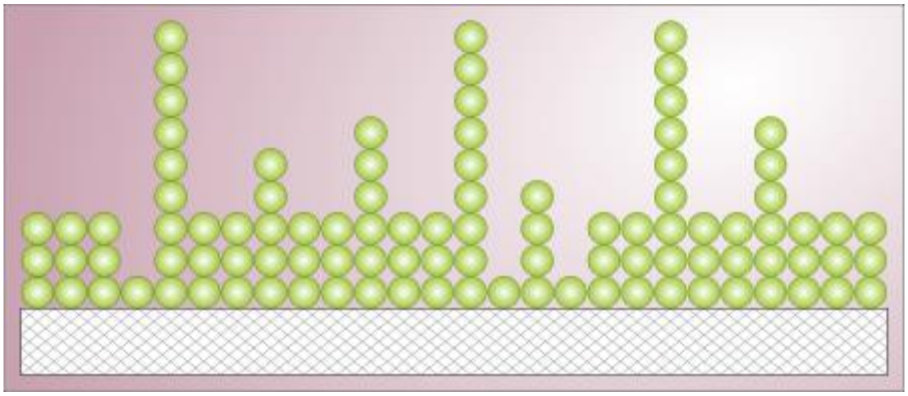

Figure 3.15 BET model of multilayer adsorption.

The BET measurement starts with a de-gas process with the aid of a vacuum pump and a heating set up (remove the water vapor). During the BET test, a known quantity of ultra-pure nitrogen gas will be introduced into the sample tube and at the same time, the pressure (p/p_0) is recorded. The BET instrument will give the analysis results and present the plot of the following equation,[11] allowing the solving of constant c and v_m.

$$\frac{1}{v[\left(\frac{p}{p_0}\right)-1]}=\frac{c-1}{v_m c}\left(\frac{p}{p_0}\right)+\frac{1}{v_m c}$$

where v is the adsorbed volume of gas, v_m is the volume of adsorbed monolayer molecule. p_0 and p are the saturation pressure and equilibrium pressure, respectively. Accordingly, the specific surface area (S) can be determined by:[11]

$$\mathrm{S}=\frac{v_m N A}{22400\times m}$$

where N is the Avogadro's number (constant), 22,400 is the volume of one mole of gas under standard pressure and temperature. A and m are the adsorbed molecule's specific cross-sectional surface area and the mass of specimen used, respectively.

The pore size distribution of materials can be revealed from their adsorption isotherms (adsorbed quantity as a function of relative pressure p/p_0 at a constant temperature). Five types of adsorption isotherms[11] are illustrated in Figure 3.16.

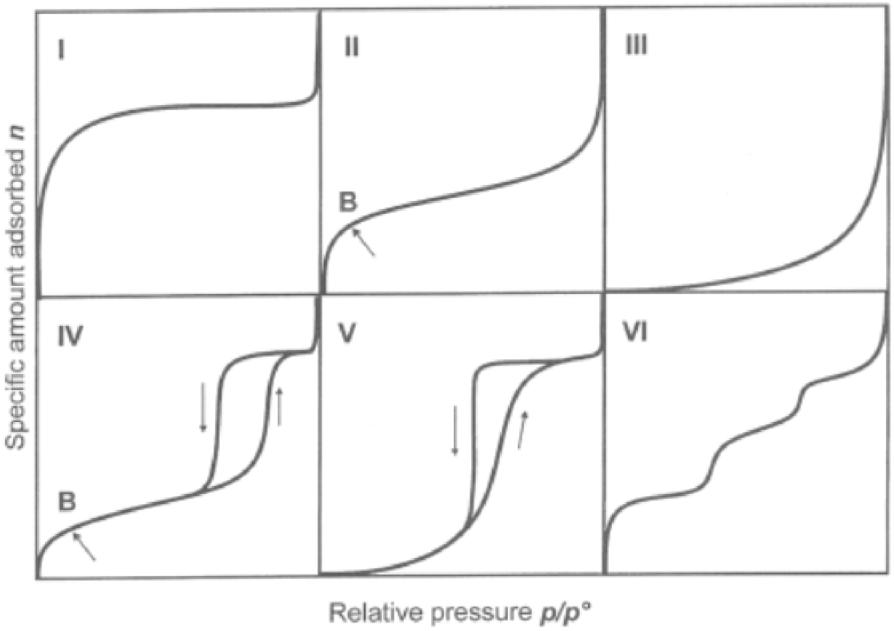

Figure 3.16 Five representative adsorption isotherms given by solid materials with different pore size distribution and surface features.

Type I isotherm is given by microporous (< 2 nm) materials. Type II isotherm represents non-porous or macroporous (> 50 nm) solid. Type III isotherm represents nonporous materials with the adsorbate-adsorbent interaction being weak. Type IV isotherm represents mesoporous materials and the characteristic hysteresis loop is related to the capillary condensation in the mesopores within the solid materials. The major difference between type V and type IV isotherm is analogous to that between type II and III. Type VI isotherm is generally given by solid with a homogeneous surface.

Scanning Electron Microscopy (SEM). The unsatisfactory image resolution of light microscopes which is limited by the wavelength of the visible light has stimulated development of electron microscopes. The unique advantage of electron is its much shorter wavelength.[12]

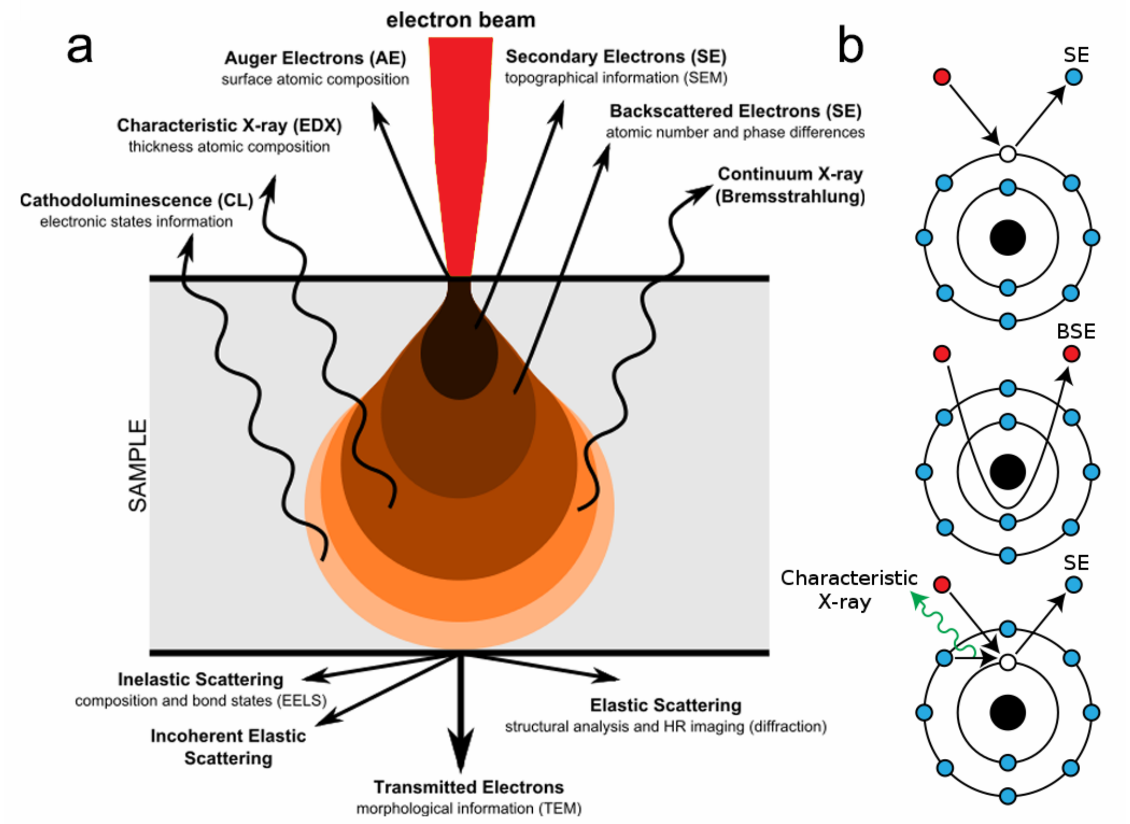

Figure 3.17 (a) Signals emitted from the sample-electron interaction. (b) Mechanism of emission of secondary electron (SE), backscattered electron (BSE) and characteristic X-ray.

The scanning electron microscope is a topographic technique and it produces images by acquiring signals generated from the interactions between the high-energy electron beam and specimen.[12] When shining incident electron towards the sample surface, the energetic electrons are able to penetrate and produce a series of signals by interacting with the specimen atoms. The penetration depth and volume depend on the electron energy, incident angle and the elements atomic number/composition of the solid specimen. Specifically, the penetration depth and volume increase with increasing electron beam energy and drop with an increase of atomic number.[12] Elements with a higher atomic number are more capable in consuming the energy of the electron beam and reduce the penetration. The beam energy can be adjusted by the accelerating voltage. A higher accelerating voltage gives a deeper penetration depth, while as a consequence, some of the surface details might be lost.

The interactions between the specimen and electron beam includes elastic and inelastic interactions.[12] Elastic scattering is featured with a negligible energy loss, resulting from the elastic collision between the incident electron and the specimen nucleus or outer shell electrons. Roughly 10-50 % incident electrons were bounced back (defined as backscattered electrons, with energy greater than 50 eV) with an angle of more than 90° and with 60-80 % of the initial energy retained. Elements with higher atomic number tend to give a higher backscattered signal because the atomic nucleus have more positive charges.[12] Inelastic scattering occurs when the electron energy transfers to the specimen atom. The ejection of the loosely bound electrons from the specimen (ionization of specimen atom) give rise to secondary electrons (having low energy around 3~5 eV).[12] A series of other signals are generated when the electron beam strikes the specimen, including the emitted Auger electron, X-ray and Cathodoluminescence (shown in Figure 3.17). Secondary electrons are mainly used for visualize the surface roughness and texture (topographic information). The backscattered electrons are utilized for collecting both the topographic and composition information. The fact that the backscattered electrons have much higher energy prevent them from being absorbed by the atoms. Thus, the region from which backscattered electrons are generated is significantly larger than that of the secondary electron. The emission of characteristic x-ray (photon) act as a way to reestablish the charge balance induced by the ionization event. Analysis of the x-ray signals with an energy-dispersive (EDX) analyzer can help extract information of the specimen composition.

Transmission Electron Microscopy (TEM). The TEM use transmitted electrons to produce atomic-resolution images, acquiring crystallography and chemistry information of the specimen. The TEM images are governed by three different contrast, which are the diffraction contrast, phase contrast and atomic number induced contrast. The phase contrast is fundamental in atomic-resolution imaging.[13]

References

[1] A. Sutka, G. Mezinskis, *Front Mater Sci* **2012**, 1-14.

[2] C. Wei, Z. Feng, M. Baisariyev, L. Yu, L. Zeng, T. Wu, H. Zhao, Y. Huang, M. J. Bedzyk, T. Sritharan, Z. J. Xu, *Chem. Mater.* **2016**, 28, 4129-4133.

[3] C. Du, Q. Tan, G. Yin, J. Zhang, *Rotating Electrode Methods and Oxygen Reduction Electrocatalysts*, Elsevier, **2014**.

[4] C. Wei, L. Yu, C. Cui, J. Lin, C. Wei, N. Mathews, F. Huo, T. Sritharan, Z. Xu, *Chem comm* **2014**, 50, 7885-7888.

[5] Y. Waseda, E. Matsubara, K. Shinoda, *X-ray diffraction crystallography: introduction, examples and solved problems*, Springer Science & Business Media, **2011**.

[6] M. Lee, *X-ray Diffraction for Materials Research: From Fundamentals to Applications*, CRC Press, **2016**.

[7] V. R. Mastelaro, E. D. Zanotto, *Materials* **2018**, 11, 204.

[8] G. Bunker, *Introduction to XAFS: a practical guide to X-ray absorption fine structure spectroscopy*, Cambridge University Press, **2010**.

[9] J. F. Watts, *Surface science techniques* **1994**, 5-23.

[10] M. Peter, A. Sherwood, *Anal Bioanal Chem* **2013**, 405, 2415.

[11] C. S. Dutcher, X. Ge, A. S. Wexler, S. L. Clegg, *J Phys Chem C* **2011**, 115, 16474-16487.

[12] S. Aharinejad, A. Lametschwandtner, *Microvascular Corrosion Casting in Scanning Electron Microscopy*, Springer, **1992**.

[13] H. Kohl, L. Reimer, *Transmission electron microscopy: physics of image formation*, Springer, **2008**.

Chapter 4

Structure flexible $CoAl_2O_4$ spinel oxides towards oxygen evolution reaction: Revealing the leading role of octahedra

Spinel oxide contains two geometric sites, i.e. the tetrahedral site and octahedral site. It is intriguing to find out which geometric site is critical in oxygen electrocatalysis. In this chapter, spinel $CoAl_2O_4$ *oxides were studied as OER catalysts because it is feasible to tune the* $CoAl_2O_4$ *from a normal structure to an inverse structure by simply varying the synthesis temperature. It is found that there exists a strong correlation between the OER and the structure inversion degree of spinel* $CoAl_2O_4$*. A progressively increased occupation of Co in the octahedral site gives enhanced OER activities, substantiating the leading role of octahedral geometry in electrocatalysis.*

4.1 Introduction

Oxygen electrocatalysis, for example, oxygen evolution (OER) and oxygen reduction reaction (ORR), are critical half-cell reactions in clean energy technologies (e.g. fuel cells, metal-air batteries, water electrolyzer and etc.).[1-2] Transition metal oxide materials have been intensively examined as oxygen electrocatalyst because they are of low cost and environmental friendly. It is known that transition metal oxides can form totally different crystal structures, including perovskite, spinel, rutile and etc. All these crystal structures accommodate transition metal in distinct coordination environment and produce different arrangements. Spinel is an interesting crystal family which has generated great attention in electrocatalysis field during recent years.[3-4]

Spinel oxide has a chemical formula of AB_2O_4 and it is constituted by transition metal elements (A and B) in different oxygen-coordinated geometry including the four oxygen-coordinated tetrahedral and six oxygen-coordinated octahedral geometry. The distribution of transition metal elements in the two geometric sites is determined by the crystal field stabilization energy and strongly depends on the synthesis conditions (e.g. annealing atmosphere, synthesis temperature, cooling rate and etc).[5-6] The parameter inversion degree (λ) defines the structure reversal in spinel oxide $(A_\lambda B_{1-\lambda})_{Td}[A_{1-\lambda}B_{1+\lambda}]_{Oh}O_4$. According to literature findings, the structure reversal of spinel has great implications for the oxygen electrocatalysis.[3] It is likely that the two geometric sites give different contributions to electrocatalytic reactions.

In this chapter, various spinel $CoAl_2O_4$ oxides synthesized at different temperatures were studied as OER catalysts. The Al in $CoAl_2O_4$ system act as catalytically inactive TM in the spinel lattice. The Al^{3+} has an electronic configuration of $1s^22s^22p^6$ and it is not active. It guarantees that the OER activity of $CoAl_2O_4$ is only affected by the electronic structure of Co. In this way, the relationship between the distribution of Co and OER activity can be exclusively examined. The experimental results show that the inversion degree of $CoAl_2O_4$ oxides was regulated from 0.15 to 0.67 by decreasing the synthesis temperature from 800°C to 400°C. It is found that the OER activity is positively related to the occupancy of Co in octahedral site, demonstrating the leading role of octahedral geometry in spinel structure towards oxygen electrocatalysis.

4.2 Experimental details

Preparation of $CoAl_2O_4$ oxides. $CoAl_2O_4$ powders were prepared by a sol-gel method[7] using citric acid as a chelating agent and urea as combustion agent. 10 mmol cobalt acetate ($Co(OAc)_2 \cdot 4H_2O$), 20 mmol aluminum nitrate ($Al(NO_3)_3 \cdot 9H_2O$), 60 mmol citric acid and 60 mmol urea were dissolved in 200 mL deionized water with stirring. As the solution turns homogenous, 10 mL of concentrated nitric acid was added. The above mixture solution was constantly stirred and heated at 80°C~100°C until highly viscous gel was formed. The gel was then dried in the oven at 170°C for 12 hours, followed by calcination at different temperatures (400°C, 500°C, 600°C, and 800°C) for 6 hours to yield $CoAl_2O_4$ powders.

Electrode preparation. Oxide electrode was fabricated by drop-casting catalysts onto a rotating disk electrode (RDE). Catalysts ink were prepared by ultra-sonicating the $CoAl_2O_4$ powders, acid-treated acetylene black (AB), Nafion® perfluorinated resin solution (5 wt% in water) in mixture solution containing water and isopropanol (volume ratio of Nafion® perfluorinated resin solution /water/isopropanol=0.05/4/1). The ink concentrations are 5 mg $m^{-1}{}_{ox}$ and 1mg $ml^{-1}{}_{AB}$. 10 μl of the ink was dropped on the RDE, yielding a final mass loading of 255 μg_{ox} $cm^{-2}{}_{disk}$ and 51μg_{AB} $cm^{-2}{}_{disk}$.

Electrochemical measurements. The OER activity of the $CoAl_2O_4$ catalysts was tested in O_2-saturated 1 M KOH solution using a three-electrode cell. The working electrode is catalyst decorated glassy carbon electrode. A Pt spiral wire and saturated calomel electrode (SCE) were used as the counter and reference electrode, respectively. The electrochemical experiments were performed using a WaveDriver Potentiostat and RDE bundle controlled by aftermath software package. A rotating speed of 1600 rpm was applied during the OER test and at least three independent measurements were performed for each catalyst.

4.3 Results and discussion

The XRD patterns of $CoAl_2O_4$ synthesized at different temperatures are shown in Figure 4.1 a. All the diffraction peaks can be indexed as cubic spinel structure (Fd-3m), indicating the phase purity of the synthesized $CoAl_2O_4$. The crystallinity degree of $CoAl_2O_4$ is getting increasingly higher with the increase of temperature. This is because the intensity of the diffraction peaks becomes stronger. Figure 4.2 b shows the surface areas of the various $CoAl_2O_4$ characterized by Brunauer–Emmett–Teller (BET). As displayed, the surface area decreases from 85.5 m^2g^{-1} to 30 m^2 g^{-1} with increasing the calcination temperature from 400°C to 800°C.

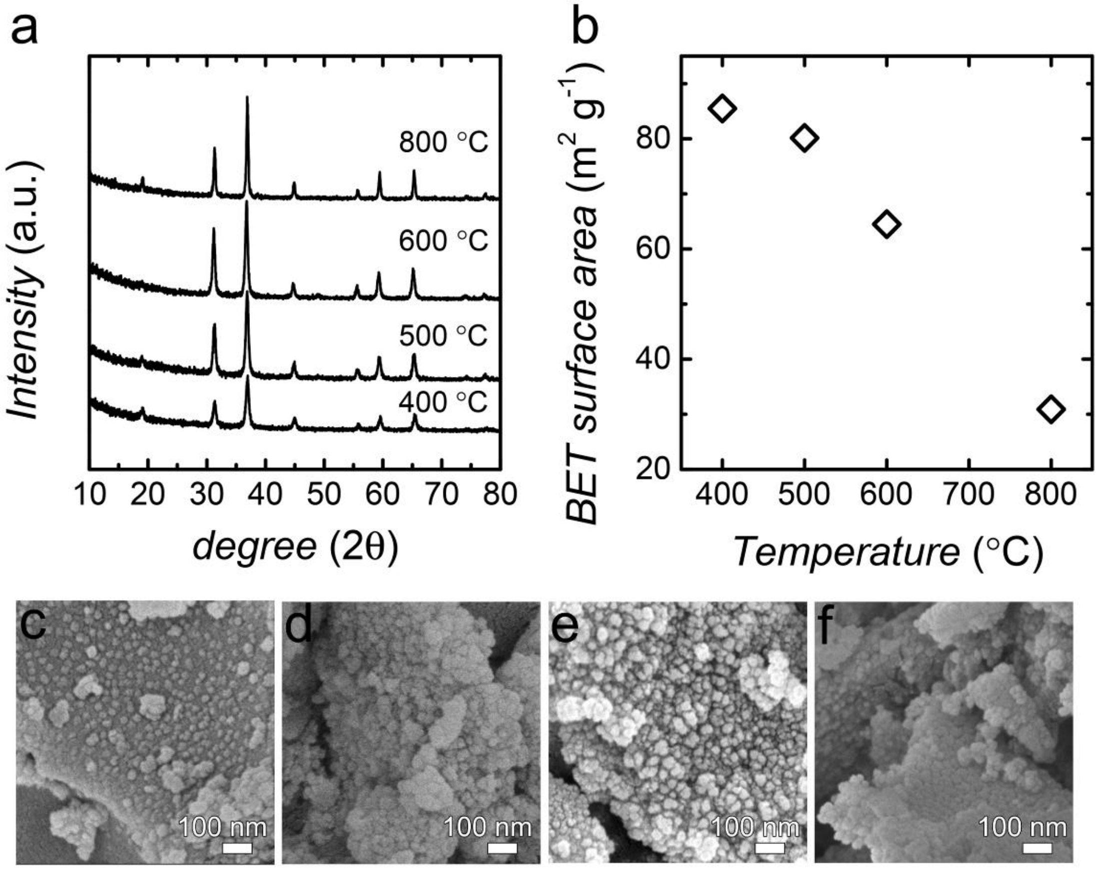

Figure 4.1 (a) XRD patterns and (b) BET surface area of $CoAl_2O_4$ oxides prepared at different temperatures ranging from 400°C to 800°C. SEM images of $CoAl_2O_4$ prepared at (c) 400°C (d) 500°C (e) 600°C and (f) 800°C.

X-ray absorption fine structure (XAFS) experiments were conducted to examine the chemical state and local environment of transition metal Co. The oxidation states were estimated from the X-ray absorption near edge structure (XANES) spectra (Figure 4.2 a). As there is a linear correlation between the absorption edge energies and the oxidation states,[8] the edge energies of Co in the various $CoAl_2O_4$ and reference oxides (CoO, Co_3O_4) were quantified by an integration method. The oxidation states of Co in $CoAl_2O_4$ were then determined (Figure 4.2 b) based on the linear relationship. It is found that the Co oxidation state in the various $CoAl_2O_4$ ranges between +2.0 ~ 2.3 and increasing the annealing temperature seems to impede the oxidation of Co in the $CoAl_2O_4$ system. The surface-sensitive Co 2p XPS spectra was provided in Figure 4.2 c, the deconvolution of the Co $2p_{3/2}$ peak indicates that the near-surface Co oxidation state does not exhibit much difference by varying the synthesis temperature.

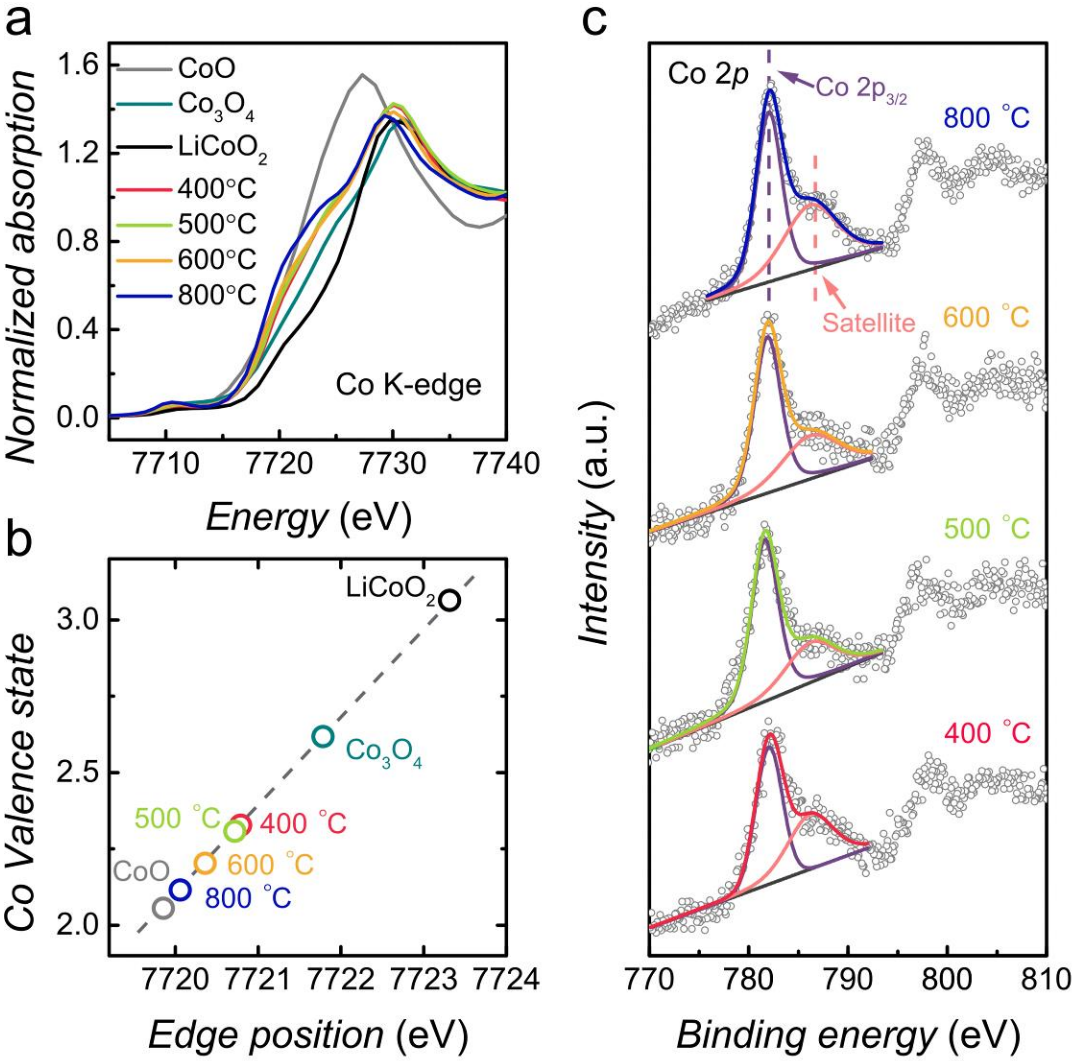

Figure 4.2 (a) Co K-edge XANES spectra and (b) the determined absorption edge positions and valence states of Co in the various $CoAl_2O_4$ oxides. (c) XPS spectra (grey dots) and deconvoluted XPS spectra (solid color lines) of Co 2p for $CoAl_2O_4$ oxides.

The OER was examined in 1 M KOH within a potential window of 1.0~1.67 V vs RHE. Tafel plots were extracted from the CV data (Figure 4.3 a) by employing background and iR-correction. To better assess the catalytic activity, the OER current was normalized by the oxides' BET surface area instead of disk area and Tafel plots are shown in Figure 4.3b. It is apparent that the 400°C sample shows significantly enhanced OER activity than the rest three. The OER activity of the $CoAl_2O_4$ oxide decreases with increasing annealing temperature.

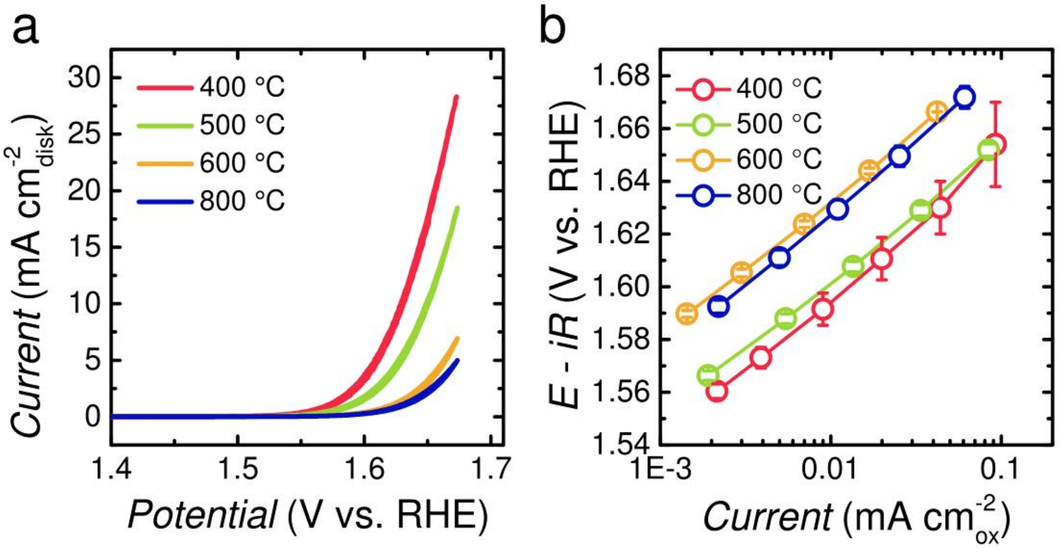

Figure 4.3 (a) OER CV curves and (b) OER Tafel plots of the various $CoAl_2O_4$ oxides.

Extended X-ray absorption fine structure (EXAFS) experiments were conducted to examine the local environment of transition metal Co. Fourier transformed (FT) EXAFS spectra at Co K-edge was shown in Figure 4.4 a to give information about the nearest coordination shells around the absorbing Co atom. The first peak (I) located at ~ 1.5 Å, is attributed to the Co-O distances.[9] Contributions from M_{Oct}-M_{Oct} and M_{Oct}-M_{Td}/M_{Td}-M_{Td} scattering give rise to the second (II) and third (III) peak at ~ 2.4 Å and ~ 3 Å, respectively.[9] The intensity ratio of peak (III)/peak (II) is an index of the cation occupancy ratio between tetrahedral and octahedral sites.[9] The high temperature-annealed $CoAl_2O_4$ oxide (800°C) only show one prominent peak at ~ 3 Å. This strongly indicates the tetrahedral-dominated occupation of Co and a resulted near normal spinel structure. With lowering the synthesis temperature, the peak at ~ 2.4 Å emerges and becomes increasingly prominent, which leads to a reduced ratio of peak (III)/peak (II). The reduced peak (III)/peak (II) ratio demonstrates that low-temperature synthesis tend to produce a higher inversion degree (x) in $(Co_{1-x}Al_x)_{Td}[Co_xAl_{2-x}]_{Oct}O_4$ structure.

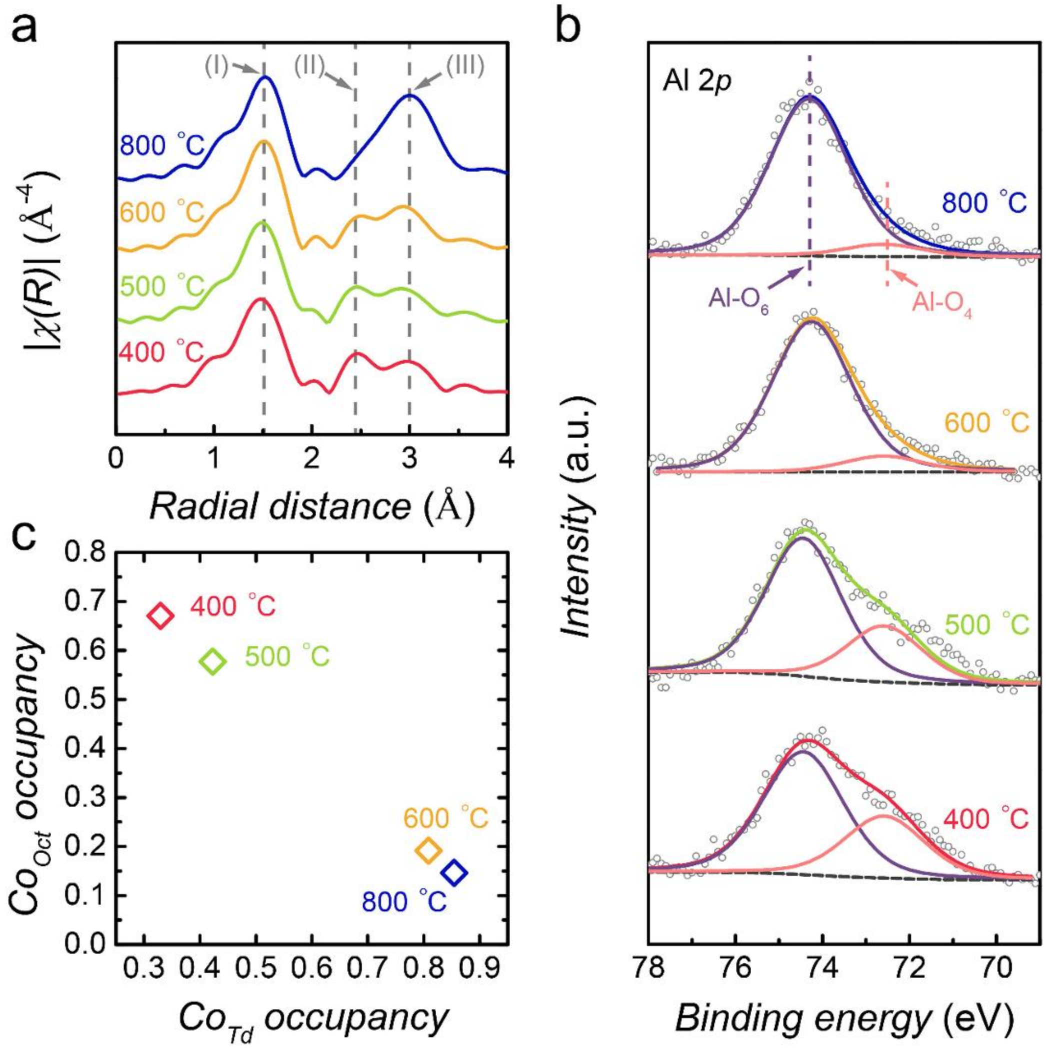

Figure 4.4 (a) EXAFS spectra of $CoAl_2O_4$ oxides at Co K-edge. (b) XPS spectra and peak deconvolution of Al 2p in $CoAl_2O_4$ oxides. (c) Tetrahedral and octahedral site-occupancy of Co in $CoAl_2O_4$, determined by peak deconvolution of Al 2p XPS spectra.

To further confirm the temperature-dependent structure reversal, XPS profile of Al 2p (Figure 4.4 b) was analyzed. The Al 2p binding energies at 74.3 ± 0.1 eV and 72.6 ± 0.1 eV can be assigned to the chemical bonding of Al in tetrahedra AlO_4 and in octahedra AlO_6, respectively.[10] The deconvolution of the Al 2p XPS spectra thus enables a quantitative examination of the cation distribution. The percentage of Al in the two geometric site is determined by the area ratio of the two peaks and corresponding results are shown in Table 4.1.

Table 4.1 Deconvolution of Al 2p XPS spectra. XPS peak position, area distribution and chemical bonding, percentage of Al in tetrahedral site and octahedral site.

Al 2p	BE (eV)	Area distribution (%)	Chemical bonding	$Al_{(Td)}$ %	$Al_{[Oct]}$ %
400 °C	74.44	33.5	Al in AlO_4 tetrahedra	33.5	66.5
	72.58	66.5	Al in AlO_6 octahedra		
500 °C	74.44	28.9	Al in AlO_4 tetrahedra	28.9	71.1
	72.58	71.1	Al in AlO_6 octahedra		
600 °C	74.25	9.6	Al in AlO_4 tetrahedra	9.6	90.4
	72.6	90.4	Al in AlO_6 octahedra		
800 °C	74.31	7.3	Al in AlO_4 tetrahedra	7.3	92.7
	72.6	92.7	Al in AlO_6 octahedra		

Given the occupation of Al, the number of Co in tetrahedral and octahedral sites was determined accordingly and summarized in Figure 4.4 c. As displayed, with decreasing temperature from 800°C to 400°C, the Co number in tetrahedral sites reduced from 0.85 to 0.33. As a result, the inversion degree of $CoAl_2O_4$ increased from 0.15 to 0.67. The produced $CoAl_2O_4$ structures can be approximated as $(Co_{0.33}Al_{0.67})_{Td}[Co_{0.67}Al_{1.33}]_{Oct}O_4$, $(Co_{0.42}Al_{0.58})_{Td}[Co_{0.58}Al_{1.42}]_{Oct}O_4$, $(Co_{0.81}Al_{0.19})_{Td}[Co_{0.19}Al_{1.81}]_{Oct}O_4$ and $(Co_{0.85}Al_{0.15})_{Td}[Co_{0.15}Al_{1.85}]_{Oct}O_4$ at 400°C, 500°C, 600°C and 800°C, respectively.

Figure 4.5 Images of synthesized $CoAl_2O_4$ at 400°C, 500°C, 600°C and 800°C (from bottom to top).

The fact that a higher inversion degree is facilitated by low-temperature synthesis in spinel $CoAl_2O_4$ system is consistent with the literature data.[11] In addition, it is interesting to find that the color of the various $CoAl_2O_4$ samples exhibits big differences. The high temperature-annealed $CoAl_2O_4$ powder gives a blue color. In remarkable contrast, the color of the low-temperature counterparts (Figure 4.5) changes to green. The observed green color in $CoAl_2O_4$ is believed to be an indication of the octahedral-coordinated Co in the spinel lattice.[11]

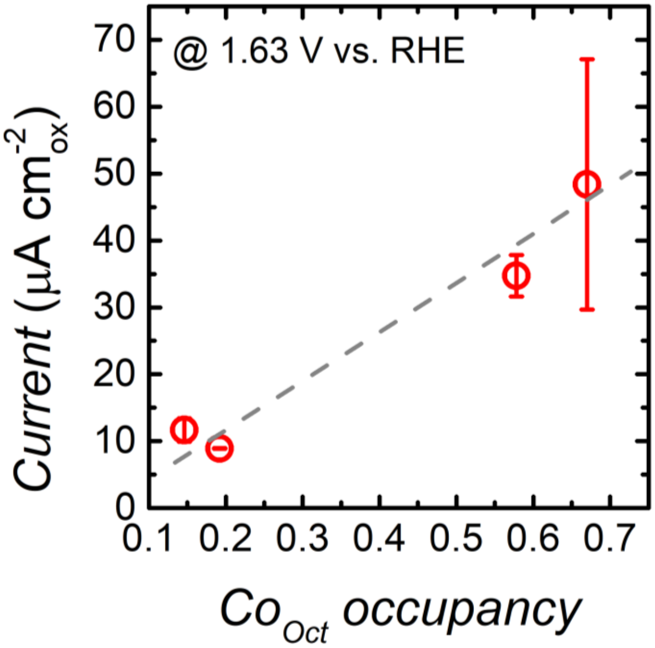

Figure 4.6 OER specific activity as a function of Co occupancy in octahedral sites

Since the various $CoAl_2O_4$ oxides do not show much difference in near-surface Co oxidation states (confirmed by Co 2p XPS spectrum, Figure 4.2 c), it is proposed that the Co geometric coordination plays an important role in OER. Thus, the OER activity of the various $CoAl_2O_4$ oxides was plotted as a function of the octahedral Co number in Figure 4.6. Specifically, the OER activity is presented by the potentials required to drive a specific current density of 25 A cm$^{-2}_{ox}$. A positive correlation between the OER specific activity of $CoAl_2O_4$ oxides and the Co occupancy in octahedral site can be observed, indicating the leading role of octahedral geometric in spinel oxides towards oxygen electrocatalysis.

4.4 Conclusion

A series of spinel $CoAl_2O_4$ oxides were synthesized at different temperatures (from 400 to 800) and studied as OER catalysts. Through Al 2p XPS spectrum analysis, the distribution of cations in the various $CoAl_2O_4$ oxides were determined (i.e. $(Co_{0.33}Al_{0.67})_{Td}[Co_{0.67}Al_{1.33}]_{Oct}O_4$, $(Co_{0.42}Al_{0.58})_{Td}[Co_{0.58}Al_{1.42}]_{Oct}O_4$, $(Co_{0.81}Al_{0.19})_{Td}[Co_{0.19}Al_{1.81}]_{Oct}O_4$ and $(Co_{0.85}Al_{0.15})_{Td}[Co_{0.15}Al_{1.85}]_{Oct}O_4$). It means that the inversion degree of $CoAl_2O_4$ oxides was regulated from 0.15 to 0.67 by decreasing the synthesis temperature from 800°C to 400°C. It is found that the OER activity of $CoAl_2O_4$ oxides is positively related to the occupancy of Co in octahedral site. This indicates that the octahedral geometry plays a leading role in spinel structure towards oxygen electrocatalysis.

References

[1] I. Katsounaros, S. Cherevko, A. R. Zeradjanin, K. J. Mayrhofer, *Angew Chem Int Ed Engl* **2014**, 53, 102-121.

[2] O. Z. Sharaf, M. F. Orhan, *Renew Sust Energ Rev* **2014**, 32, 810-853.

[3] Guangping Wu, W. D. Jun Wang, L. L. Yao Nie, Xueqiang Qi, Siguo Chen, Z. Wei, *Angew. Chem. Int. Ed.* **2015**, 54, 1-6.

[4] Y. Liang, H. Wang, J. Zhou, Y. Li, J. Wang, T. Regier, H. Dai, *J. Am. Chem. Soc.* **2012**, 134, 3517-3523.

[5] J. Li, H. Yuan, G. Li, Y. Liu, J. Leng, *J. Magn. Magn. Mater.* **2010**, 322, 3396-3400.

[6] B. Bateer, C. Tian, Y. Qu, S. Du, Y. Yang, Z. Ren, K. Pan, H. Fu, *Dalton Trans* **2014**, 43, 9885-9891.

[7] A. Sutka, G. Mezinskis, *Front Mater. Sci.* **2012**, 1-14.

[8] H. Dau, P. Liebisch, M. Haumann, *Anal. Bioanal. Chem.* **2003**, 376, 562-583.

[9] H. Y. Wang, S. F. Hung, H. Y. Chen, T. S. Chan, H. M. Chen, B. Liu, *J. Am. Chem. Soc.* **2015**, 138, 36-39.

[10] K. Tshabalala, I. Nagpure, H. Swart, O. Ntwaeaborwa, S.-H. Cho, J.-K. Park, *J. Vac. Sci. Technol. B* **2012**, 30, 031401.

[11] X. Duan, M. Pan, F. Yu, D. Yuan, *J. Alloys Compd.* **2011**, 509, 1079-1083.

Chapter 5

Mn-Co containing spinel oxides towards oxygen reduction: Revealing the catalytic-critical role of e_g filling

A series of spinel oxides $ZnCo_xMn_{2-x}O_4$ *(x ranging from 0 to 2) were prepared to facilitate an exclusive examination of the edge-sharing* $[TMO_6]$ *octahedra towards ORR and to reveal the dominating parameter that governs the composition dependent ORR. It is found that the distinctive ORR of* $ZnCo_xMn_{2-x}O_4$ *is strongly correlated to the* e_g *electron of active Mn that resulting from the superexchange interactions (*$Mn_{[Oh]}$*-O-*$Co_{[Oh]}$*) through the edge sharing* $[Co_xMn_{1-x}O_6]$ *octahedra. With Co gradually replaces Mn, the* e_g *state of Mn cations evolves from 0.3 to 0.9. The ORR of Mn-Co based spinel oxides exhibits a volcano shape as a function the* e_g *occupancy of Mn cations, indicating the influencing role of* e_g *electron.*

---

*This chapter published substantially as Y. Zhou, S. Sun, S. Xi, Y. Duan, T. Sritharan, Y. Du, Z. J. Xu. *Adv. Mater.* 30, 1705407 (2018).

5.1 Introduction

The escalating demand for energy and the detrimental environmental impact brought by the consumption of fossil fuels have stimulated research on clean and sustainable energy conversion/storage devices. Promising clean energy storage/conversion devices, e.g. the rechargeable metal-air batteries, electrolyzer, and regenerative fuel cells, are relying strongly on oxygen electrochemistry.[1] Developing efficient and cost-effective catalysts for oxygen reduction reaction is one of the critical aspects for the clean energy infrastructures. Noble metals, for example, Pt, offer high ORR efficiency but are not sustainable choices.[1] Due to abundant reserve and environmental friendless, transition metal oxides have been widely studied as alternative electrocatalysts and promising catalytic activity has been reported.[1-2] Among all the oxide families, oxide materials with spinel structure has received tremendous attention, especially for mixed-metal spinel oxides.[2-4] It is found that the mixed-metal (Mn and Co) spinel oxide is one of the most promising materials in catalyzing oxygen reduction reaction (ORR).[3-4] Great efforts have been devoted to fabricating ultra-small particles,[4] engineering the Mn/Co composition,[2] designing porous Mn-Co spinel oxide[5] or hybrids (e.g. $MnCo_2O_4$/N-doped-rmGO)[6] to improve catalyst's mass or geometric activity. The analysis by intrinsic activity (kinetic current density normalized to catalysts' surface area), however, is rather limited.

Spinel oxides feature a cubic-tetragonal phase transition sensitively correlated to Mn concentration.[2] As such, the well-designed tetragonal and cubic Mn-Co spinel oxides of the same compositions has revealed the structure-activity relationship where cubic spinel beats their tetragonal counterparts.[2] The inferior catalytic activity of tetragonal spinel was due to its weaker oxygen binding energy.[2] While an increased ORR activity given by higher Mn content was consistently observed in the Mn-Co spinel possessing the same crystal structure (either cubic or tetragonal), results from other studies have been contradictory in this regard.[3, 7] Typically, continuous increasing Mn/Co ratio beyond 0.5 has produced a decreasing ORR activity in $Mn_xCo_{3-x}O_4$.[7] In addition, while the highest ORR activity was generally attained by a cubic Mn-Co spinel phase among the investigated composition range, the optimum Mn/Co ratio in yielding the highest activity differs from 0.15~2.0 based on earlier studies.[3, 7-8] Thus, the dominating parameter that relates the oxygen reduction activity of Mn-Co containing spinel oxides to compositional changes of Mn/Co has not been revealed.

In this chapter, the activity of edge-sharing [$Co_xMn_{1-x}O_6$] octahedra is exclusively examined by the design of spinel $ZnCo_xMn_{2-x}O_4$ (x=0.0~2.0) oxide. The Zn aims to fix the spinel to normal structure, and with the inactive Zn ($e^4t_2^6$) occupying all the tetrahedral site, catalytic contribution from tetrahedral geometry is excluded. The optimized ORR activity observed in $ZnCo_{1.4}Mn_{0.6}O_4$ is comparable to series of $Mn_xCo_{3-x}O_4$ reported, which substantiate the dominating role of octahedral geometry in catalytic oxygen reduction. It is revealed that the Mn/Co compositional effects on ORR are the consequences of superexchange interaction between edge sharing [CoO_6] and [MnO_6]. The modulated e_g occupancy of active Mn cation brought by Co substitution describes the ORR activity of edge-sharing [$Co_xMn_{1-x}O_6$] in spinel $ZnCo_xMn_{2-x}O_4$ oxide.

5.2 Experimental section

Material synthesis. The $ZnCo_xMn_{2-x}O_4$ particles were synthesized via a sol-gel auto combustion method.[9] 2.5 mmol $Zn(CH_3COO)_2 \cdot 2H_2O$, 5 mmol $(CH_3COO)_3Mn \cdot 2H_2O$ + $(CH_3COO)_2Co \cdot 4H_2O$ and 15 mmol citric acid were dissolved in 30 ml DI water and 2 ml nitric acid by stirring. The molar ratio of $(CH_3COO)_3Mn \cdot 2H_2O$ to $(CH_3COO)_2Co \cdot 4H_2O$ was (2-x) /x. The solution mixture was constantly stirred and heated to 90℃ and maintained at this temperature for several hours until it converted to a viscous gel. Then, the gel was decomposed in an oven at 170 °C for 12 hours to remove the remaining water. The dried-gel was ground thoroughly and annealed in air at 600 ℃ for 6 hours (heating rate: 10°C min^{-1}) to obtain pure spinel $ZnCo_xMn_{2-x}O_4$ powder. The sol-gel auto combustion method affords a high yield of 90% ~crystalized particles.

Electrode preparation. Oxide-decorated electrode was fabricated by drop-casting catalysts onto a rotating disk electrode (RDE). Catalysts ink were prepared by ultra-sonicating the $ZnCo_xMn_{2-x}O_4$ powders, acid-treated acetylene black (AB), Nafion® perfluorinated resin solution (5 wt% in water) in mixture solution containing water and isopropanol (volume ratio of Nafion® perfluorinated resin solution /water/isopropanol=0.05/4/1). The ink concentrations are 5 mg $m^{-1}{}_{ox}$, and 1mg $ml^{-1}{}_{AB}$. 10 μl of the ink was dropped on the RDE, yielding a final mass loading of 255 μg_{ox} cm^{-2}_{disk} and 51μg_{AB} cm^{-2}_{disk}. Before drop casting catalysts onto RDE, the RDE electrode was polished for 30 minutes using alumina slurry and cleaned by repeated ultrasonication in ethanol and DI water.

Electrochemical measurements. All electrochemical measurements were conducted with PINE Wave Driver 20 bi-potentiostat in a three-electrode glass cell where Pt wire acts as counter electrode, catalyst-decorated ring disk electrode (RDE) as working electrode and saturated calomel electrode (SCE) as reference electrode. Electrolyte used was 0.1 M KOH and potentials were calibrated to reversible hydrogen electrode (RHE). Prior to the ORR, the working electrode is scanned in Ar-saturated 0.1 M KOH (1.0~0.4 V vs. RHE) for the background current collection. During ORR tests, the working electrode is scanned cathodically from 1.0 to 0.4 V vs. RHE in O_2-saturated 0.1 M KOH electrolyte at different rotating speeds (100 rpm, 400 rpm, 900 rpm, and 1600 rpm).

5.3 Results and discussion

As shown in Figure 5.1 a, the spinel structure consists of corner-sharing tetrahedra/octahedra and edge-sharing octahedra/octahedra arrangements. The electronic state of transition metal cations is closely related to the exchange interactions in the spinel lattice. The crystal structure of the synthesized $ZnCo_xMn_{2-x}O_4$ (x=0~2) oxides were confirmed by XRD characterization. XRD patterns (Figure 5.1 b) demonstrate that spinel structures are maintained with Co substitution. Specifically, a transition from tetragonal to cubic phase can be observed as Co content increases and the transition point is at a Co composition (x) between 0.6~1.0. The low symmetric tetragonal phase frequently observed in Mn-rich spinel oxides is owing to the lattice distortion induced by high spin Mn ions ($t_{2g}^3e_g^1$).[2] The structure transition from tetragonal (Mn-rich spinel) to cubic phase (Co-rich spinel) in $ZnCo_xMn_{2-x}O_4$ can be ascribed to the changing in Mn concentration. More specifically, with Co gradually replacing Mn, the Jahn-Teller distortion is getting indistinctive as Mn is becoming less concentrated, and thus the spinel converts to cubic form in Co-rich $ZnCo_xMn_{2-x}O_4$. Figure 5.1 c shows the surface areas of investigated oxides from Brunauer–Emmett–Teller (BET) measurements. The BET values range from 20 ~ 35 m^2 g^{-1} in almost all the compositions, except for $ZnCo_2O_4$ (~5 m^2 g^{-1}).

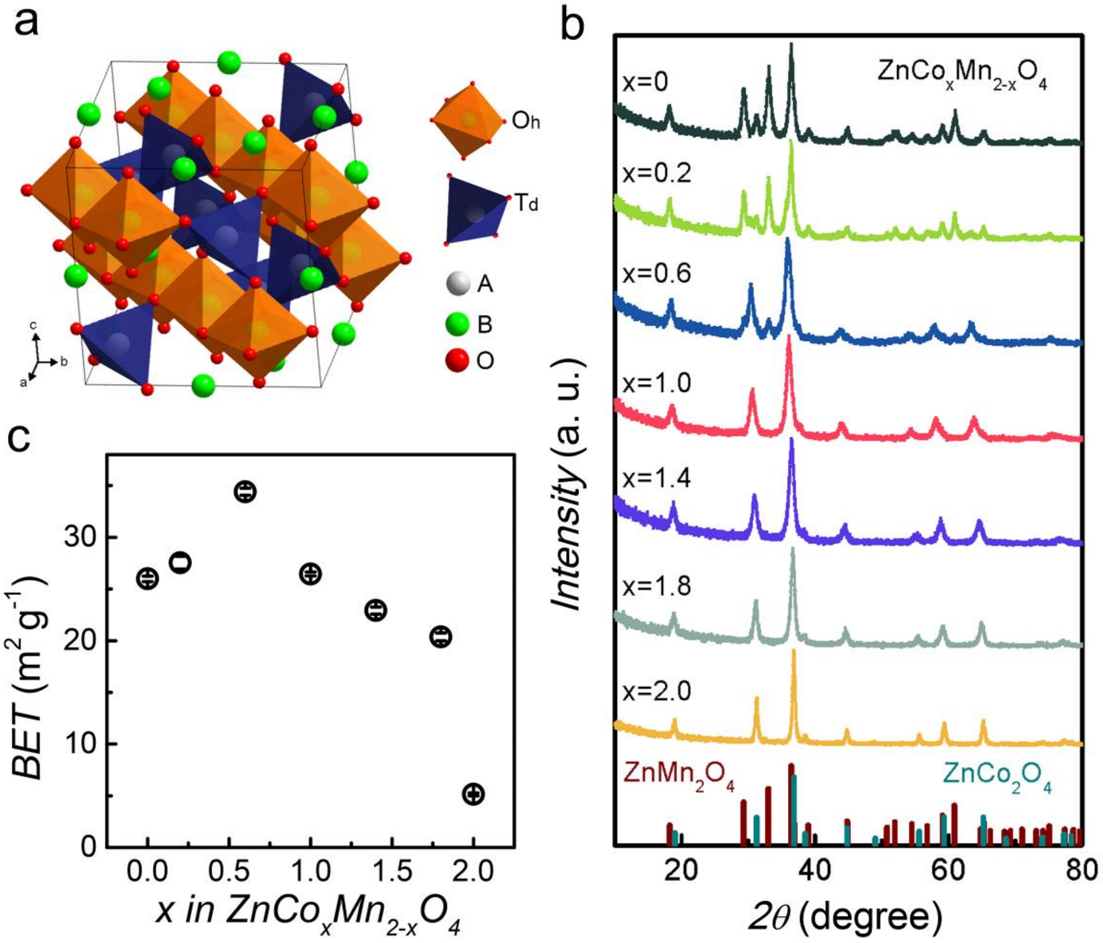

Figure 5.1 (a) Crystal structure of spinel oxide. (b) XRD pattern and (c) BET surface area of the synthesized ZnCo$_x$Mn$_{2-x}$O$_4$ oxides.

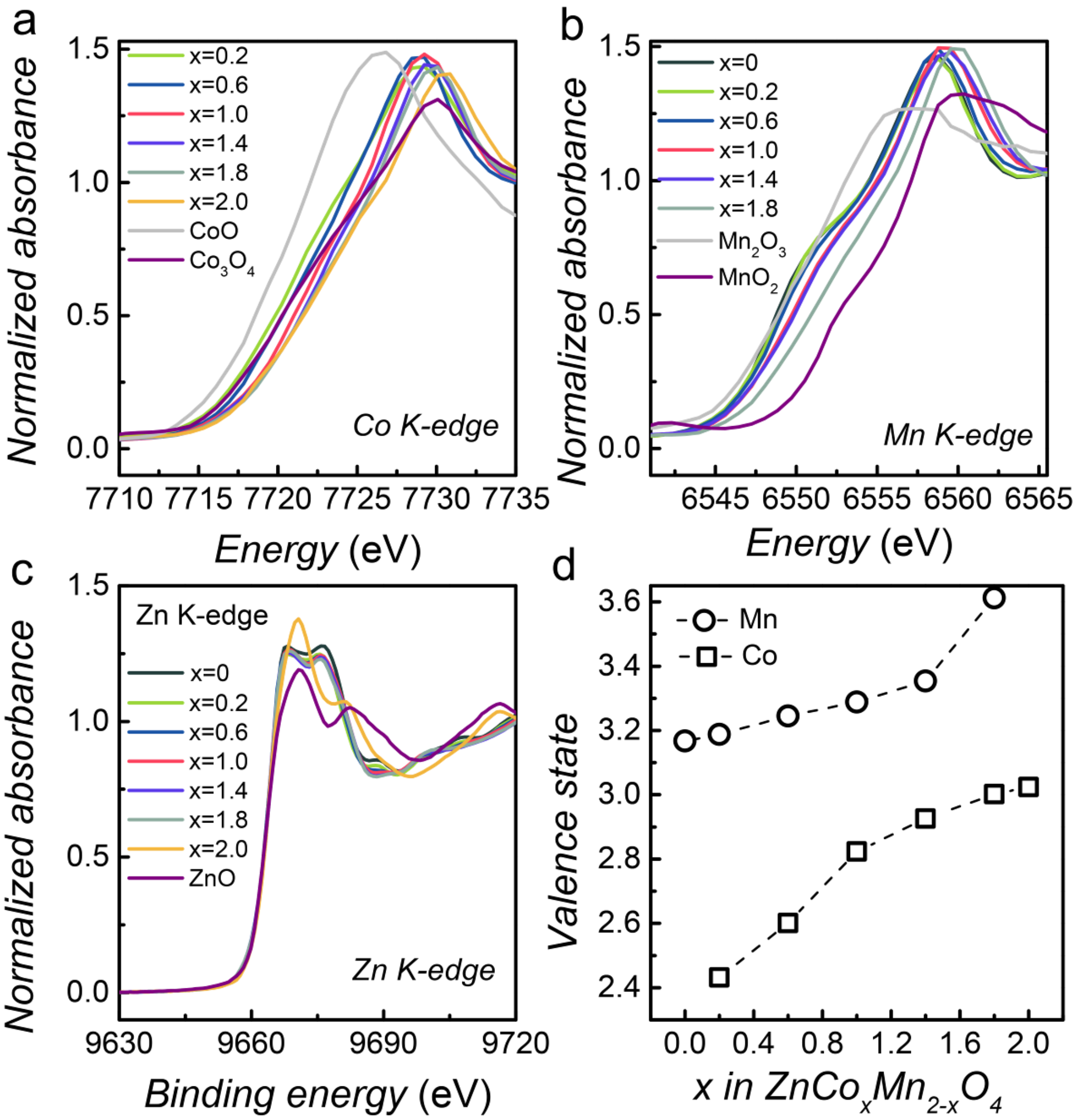

Figure 5.2 Normalized XANES spectra at (a) Co, (b) Mn and (c) Zn K-edge. (d) The quantified Mn and Co valence state obtained from XANES analysis.

To examine the valence state of cations, the X-ray absorption near edge structure (XANES) spectra at Mn, Co, and Zn K-edge are provided (Figure 5.2 a, 5.2 b and 5.2 c). For Mn K-edge spectra (Figure 5.2 b), the edge position progressively shifts to high binding energy with increasing Co content, indicating an increment in Mn oxidation state as Co gradually replaces Mn. As for Co K-edge, substituting Co from 0.2 to 1.8 results in a higher Co valence state in Mn-containing ZnCo$_x$Mn$_{2-x}$O$_4$ as signified by the gradual positive shift in adsorption edge (Figure 5.2 a). All the Zn K-edges (Figure 5.2 c) overlap with that of the reference ZnO, indicating the very existence of Zn^{2+} in the various $ZnCo_xMn_{2-x}O_4$ oxides. Since the adsorption edge position can be quantitatively related to cation oxidation state, the oxidation state of Mn and Co in $ZnCo_xMn_{2-x}O_4$ were determined through an integration method[10] and summarized in Figure 5.2 d. As illustrated, with Co gradually replaces Mn, an enhanced presence of Mn^{4+} can be observed, which is in agreement with those reported for $LaMnCoO_3$, $Mn_xCo_{3-x}O_4$.[7, 11] The Mn valence state higher than +3 indicates the presence of mixed Mn^{3+}/Mn^{4+}, as the broad pre-edge peak shape in the Mn K-edge spectra evidenced the absence of any significant Mn^{2+}.[12-13] In contrast, the Co exists as a mixed valence state of Co^{2+} and Co^{3+}.

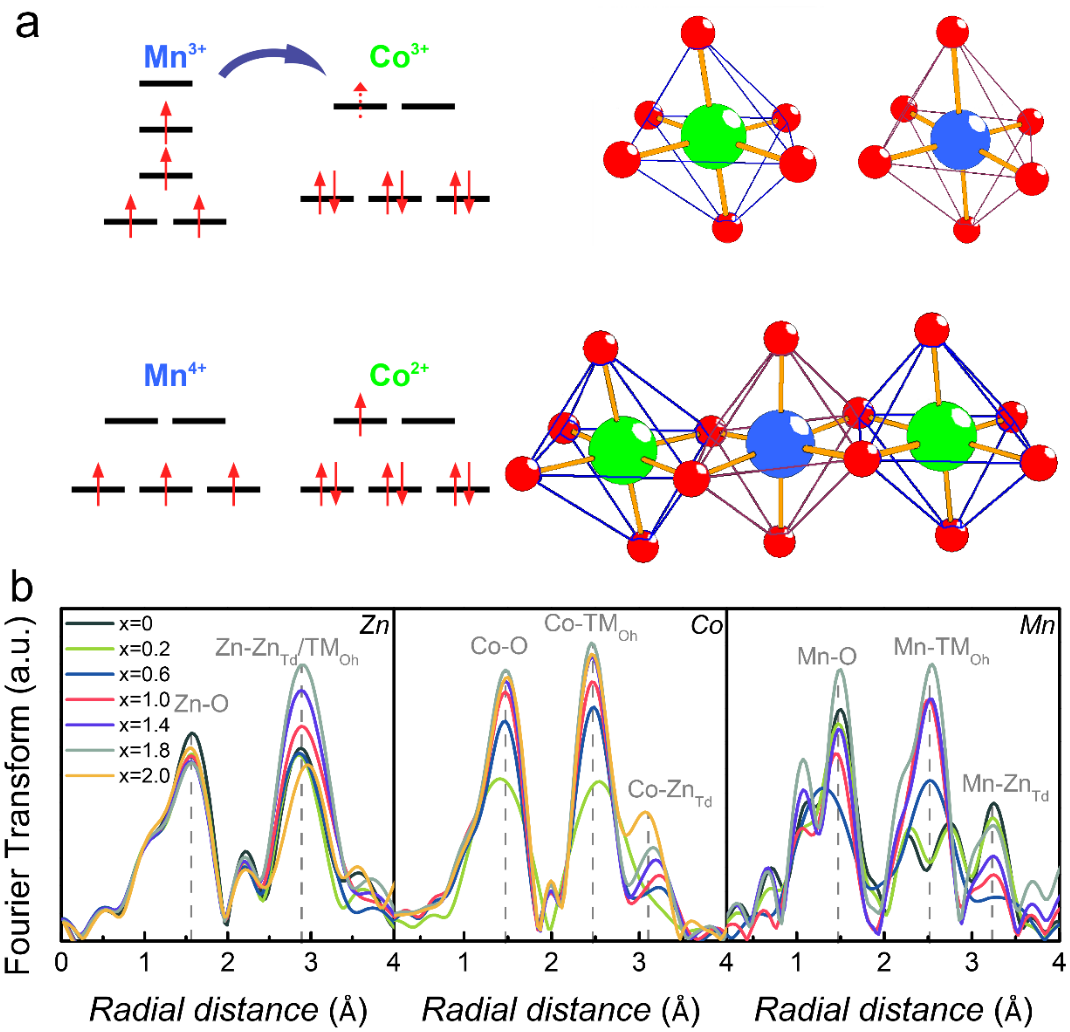

Figure 5.3 (a) Charge redistribution via $Mn^{3+} + Co^{3+} \rightarrow Mn^{4+} + Co^{2+}$. (b) EXAFS k^3 $\chi(R)$ spectra at Zn, Co and Mn K-edge for $ZnCo_xMn_{2-x}O_4$.

The cation oxidation distribution observed from the XANES can be explained by the charge redistribution via $Mn^{3+} + Co^{3+} \rightarrow Mn^{4+} + Co^{2+}$, as illustrated in Figure 5.3 a. The superexchange interaction between the Mn and Co cations via the mediation of oxygen anions (Mn–O–Co) give rise to the electronic structure change.[14] To be specific, the $ZnMn_2O_4$ spinel has elongated MnO_6 octahedra and $ZnCo_2O_4$ has cubic CoO_6 octahedra. As Co progressively replaces Mn, electron transfers from the Mn e_g orbital to the empty e_g orbital of Co through the edge-sharing $[Co_xMn_{1-x}O_6]$ octahedra network, giving electronic state change. To probe the local environment of the metal cations in spinel $ZnCo_xMn_{2-x}O_4$, extended X-ray absorption fine structure (EXAFS) was carried out. Structure information can be extracted from the Fourier transform (FT) EXAFS spectra where the bond distances between the absorbing atom and backscattering atom are revealed. The first peak around ~1.5 Å reflects the first oxygen to absorbing atom bond distance, as indicated by Zn-O, Co-O and Mn-O in Figure 5.3 b, respectively.[15-16] The next peak comprising one broad or two sub-peaks can be assigned to the scattering paths of the metal ions to its nearest neighboring metal cations in tetrahedral or octahedral site.[15-16] Such interatomic metal-metal distances were found to be crucial in revealing the cation distribution in spinel oxide. To be specific, the metal ion of interest, if located at octahedral site, possess two metal-metal distances ($Atom_{[Oh]}$-$Atom_{[Oh]}$ at ~2.5 Å, and $Atom_{[Oh]}$-$Atom_{[Td]}$ at ~3.0 Å) in the FT EXAFS spectra. In contrast, only one metal-metal distance ($Atom_{[Td]}$-$Atom_{[Oh]}$ at ~3.0 Å) exists for the absorbing metal ions located at tetrahedral site.[17] Through observing the interatomic metal distances for the Zn, Co and Mn spectra (Figure 5.3), it can be concluded that Zn is preferentially fixed at tetrahedral sites, while Co/Mn is incorporated in octahedral B-sites.

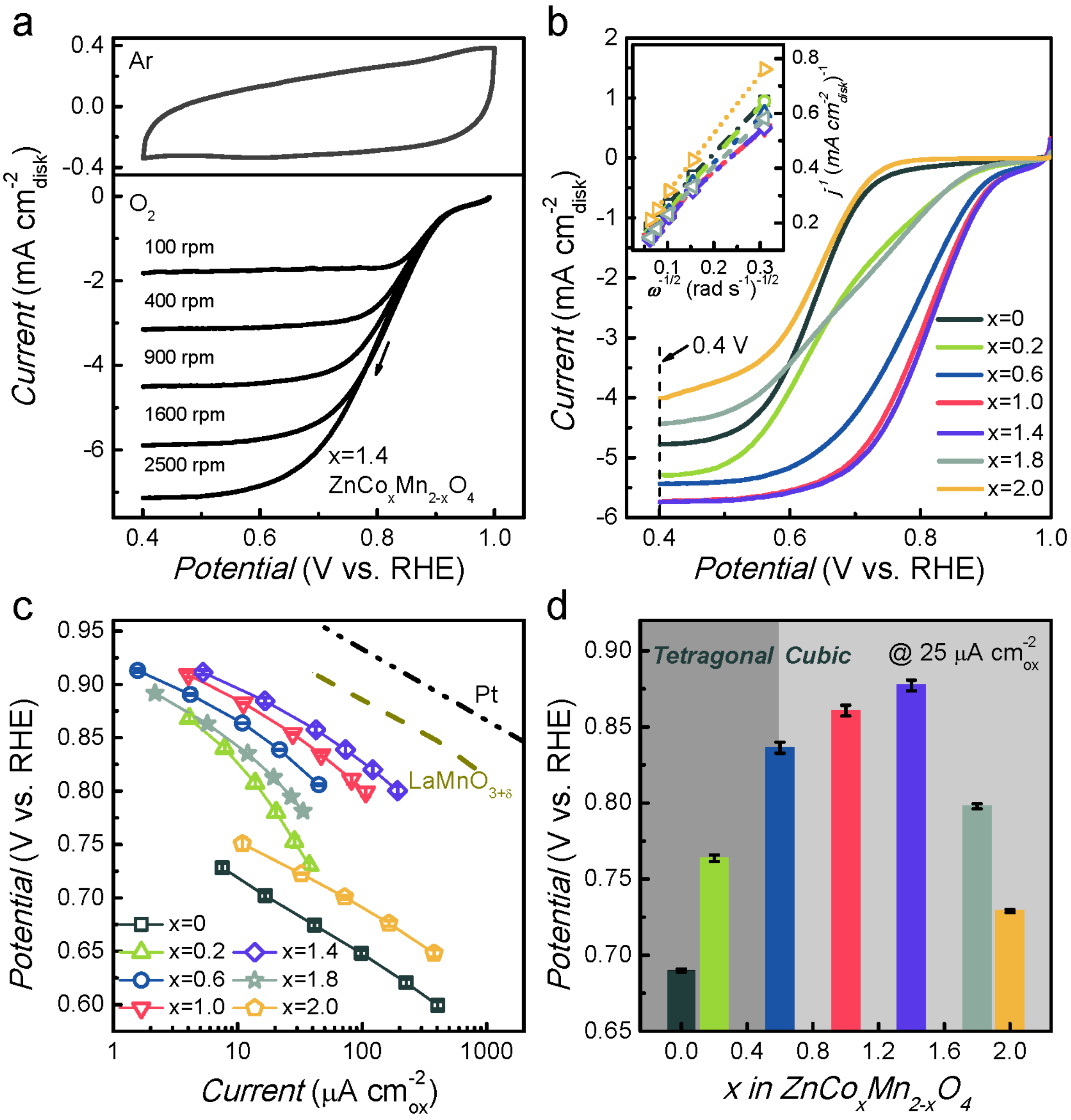

Figure 5.4 (a) Representative background CV scanned in Ar-saturated electrolyte and ORR polarization curves at different rotating speeds in O_2-saturated 0.1 M KOH electrolyte ($ZnCo_{1.4}Mn_{0.6}O_4$). (b) ORR polarization curves of $ZnCo_xMn_{2-x}O_4$ at a rotating speed of 1600 rpm, inset is the Koutecky-Levich plots at applied potential of 0.4 V. (c) Specific activities of $ZnCo_xMn_{2-x}O_4$, compared with those reported in the landmark literature: Pt/C and $LaMnO_{3+\delta}$. (d) Potentials at 25 μA cm^{-2}_{ox} for the various $ZnCo_xMn_{2-x}O_4$ catalysts.

The electrocatalytic activities of the as-prepared $ZnCo_xMn_{2-x}O_4$ toward oxygen reduction were examined in alkaline solution using a rotating disk electrode (RDE). Prior to the ORR tests, the catalysts were cycled within a potential window of 1.0 ~ 0.4 V (vs. RHE) in Ar-saturated 0.1M KOH for the background subtraction. Oxygen reduction was then performed in O_2-saturated electrolyte at a scan rate of 10 mV s^{-1} by applying rotating speed varying from 100 rpm to 2500 rpm. The background CV and ORR polarization curves of $ZnCo_{1.4}Mn_{0.6}O_4$ electrode are displayed in Figure 5.4 a, as a representative. The polarization curves show a kinetic-controlled region within the potential ~0.85-0.93 V, a diffusion-controlled region with potential negative than ~0.63 V and a diffusion-kinetic combined region in between. For comparison, the polarization curves of all the investigated spinel catalysts at a rotating rate of 1600 rpm were mapped out in Figure 5.4 b. The diffusion limiting currents range between ~4-6 mA cm^{-2}, which are similar to those reported in Mn and/or Co-based spinel oxides.[18] It is noted that the ORR onset potential (@1 mA cm^{-2}_{disk}, Table 5.1) shifts positively with incorporation of Co, and especially a significant reduction in overpotential (~200 mV) can be found with moderate Co substitution (composition x=0.6, x=1.0 and x=1.4) compared with Co-free catalysts. The Koutecky-Levich plots for each catalyst at an applied potential of 0.4 V (vs. RHE) in the diffusion-controlled region are displayed in the inset of Figure 5.4 b. The linearity of the Koutecky-Levich plots demonstrates that the surface electron transfer process is fast enough to catch up the diffusion-convection rate.[19] As the slope of the fitting line is a reflection of the electron transfer path in oxygen reduction process, the electron transfer number was calculated to be ~4 from the Koutecky-Levich plots. The electron transfer number shows a slight decrease in the sequence (x=1.4/x=1.0, x=0.6/x=1.8, x=0.2 and x=2.0) generally mirrors that of the shift in ORR onset potential.

Table 5.1 ORR onset potentials of $ZnCo_xMn_{2-x}O_4$ oxides (defined as the potential to drive a current density of 1 mA cm^{-2}_{disk}).

	x=0	x=0.2	x=0.6	x=1.0	x=1.4	x=1.8	x=2.0
ORR onset potential (@1 mA cm^{-2}_{disk})	0.69	0.79	0.86	0.87	0.88	0.80	0.68

Figure 5.4 c is the corresponding Tafel plots showing normalized current densities in the kinetic-controlled potential region after capacitance-, mass transportation- and iR-correction.[18] Specifically, the current densities were normalized by the BET surface area

of the $ZnCo_xMn_{2-x}O_4$ particles in order to make a fair comparison of their intrinsic activity and additionally the Tafel plots of Pt/C and $LaMnO_{3+\delta}$ were added for the purpose of comparison.[20] As illustrated in Figure 5.4 c, the catalyst with Co content of x=1.6 has a Tafel slope of 67 mV dec^{-1}, similar to that of Pt/C (66 mV dec^{-1}) in the investigated low-overpotential region and it possesses the highest activity amongst all the Co-substituted spinel catalysts. This demonstrates that the incorporation of Co has successfully narrowed the activity gap of as-prepared spin catalysts with the best noble Pt/C and afforded a decent ORR activity approaches that of $LaMnO_{3+\delta}$, with only ~50 mV overpotential difference. Apparently, introducing Co produces activity enhancement in different degree, depending on the amount of Co incorporated. For composition x=0.6, x=1.0, x=1.8 and x=0.2, relatively large Tafel slopes of 80, 74, 103, and 143 mV dec^{-1} are observed, respectively. However, with Tafel slope down to ~70 mV dec^{-1} for both $ZnMn_2O_4$ and $ZnCo_2O_4$, ORR can only be triggered at the relatively high overpotential. Based on the Tafel plot results, the catalytic activity was further evaluated by the potentials required to afford a given specific current density of 25 $\mu A\ cm^{-2}_{ox}$ (Figure 5.4 d). The specific current can be reached at potentials of 0.69, 0.86 and 0.73 V (vs. RHE) for $ZnMn_2O_4$, $ZnCo_{1.0}Mn_{1.0}O_4$, and $ZnCo_2O_4$, respectively. As a higher potential signifies a better ORR activity for a given oxide, the highest activity was found in the substituted $ZnCo_{1.4}Mn_{0.6}O_4$ of cubic spinel phase. The ORR activity of the best-performing $ZnCo_{1.4}Mn_{0.6}O_4$ catalyst is compared with the various Mn-Co based spinel oxide reported (Table 5.2). The comparisons made are in consideration of situations that conductive carbon is physically mixed with oxide catalyst in electrode preparation. This is because, for the hybrid structure, it is difficult to differentiate the actual contribution from the oxide part. It is known that NPs/C hybrid fabricated by certain in situ approaches delivers significantly promoted catalytic activity comparing with the physical mixture of NPs and conductive carbon owing to the positive coupling between the oxide and carbon.[6, 21] Considering that the $ZnCo_{1.4}Mn_{0.6}O_4$ catalyst gives surprising ORR intrinsic activity which is comparable to, or surpasses, that of the $Mn_xCo_{3-x}O_4$ reported elsewhere[2, 6-7, 18, 22] (as shown in Table 5.2), it is suggested that the octahedra instead of tetrahedra contributes mostly to the ORR activity in spinel oxide.

Table 5.2 ORR activities of $ZnCo_{1.4}Mn_{0.6}O_4$ and various Co-Mn based spinel catalysts reported in literature (Co-Mn spinel oxide are physically mixed with conductive additive)

Catalysts	E_{half} (RHE)	I_d (m A cm^{-2})	I (m A cm^{-2}) @ 0.85V	n	BET (m^2 g^{-1})	Electrolyte
$ZnCo_{1.6}Mn_{0.4}O_4$ (This work)	0.81	~5.74	1.72	~4	25	0.1M KOH
[2]c-$CoMn_2$	0.75	~4.25	0.70	3.91	84	0.1M KOH
[7]$Mn_{0.4}Co_{2.6}O_4$	0.79	~5.5	0.51	~4.0		0.1M KOH
[22]$Mn_2Co_1O_4$-NP	0.81	~2.5	0.75	~3.3	91	1 M NaOH
[6]$MnCo_2O_4$	0.82	~2.75	0.64			1.0M KOH
[18]$MnCo_2O_4$-900°C	0.70	~5.7	0.17	~4.0	2	0.1M KOH

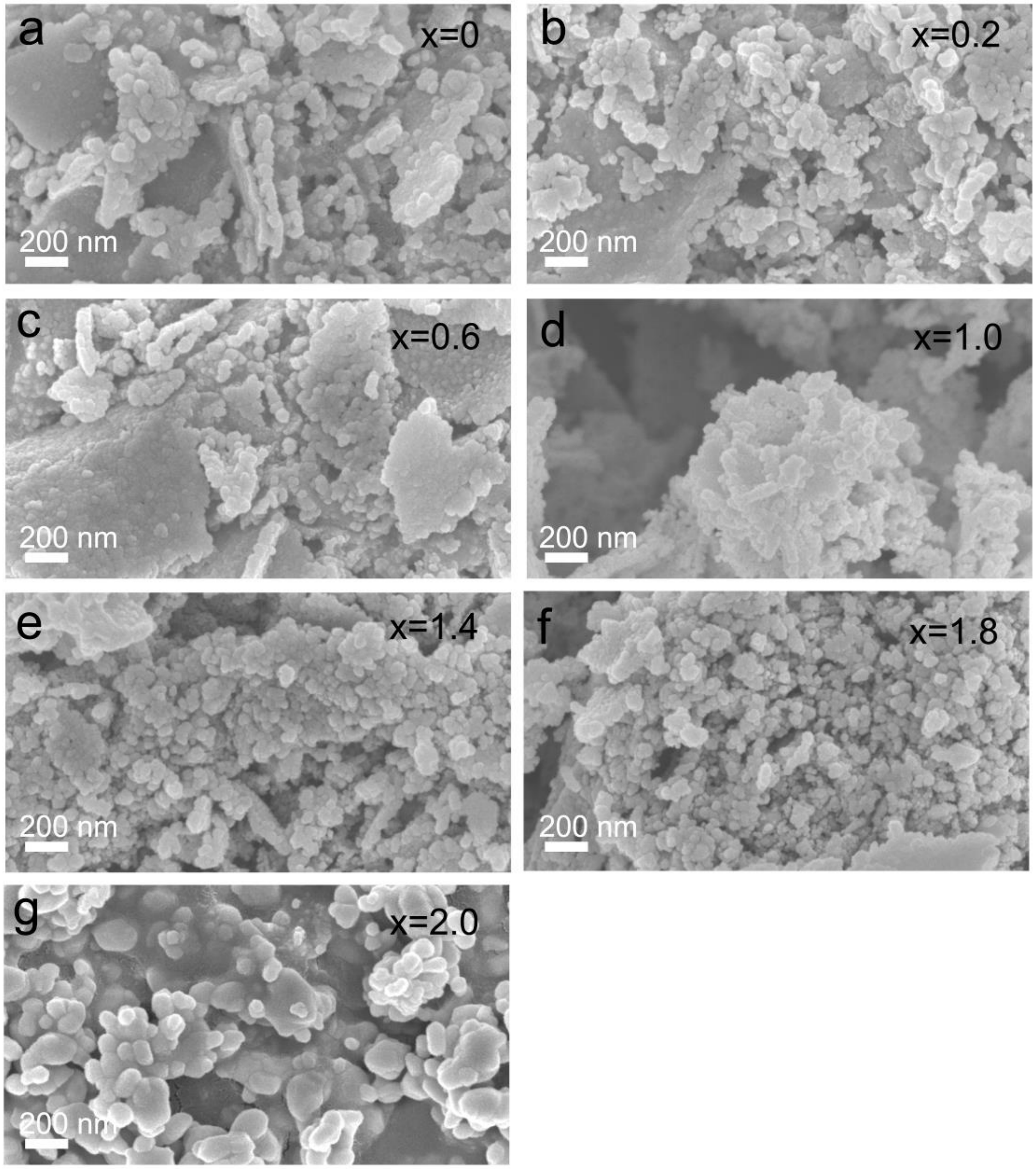

Figure 5.5 SEM images of $ZnCo_xMn_{2-x}O_4$ oxides with a Co substitution amount of (a) 0, (b) 0.2, (c) 0.6, (d) 1.0, (e) 1.4, (f) 1.8, and (g) 2.0.

The SEM images of the various $ZnCo_xMn_{2-x}O_4$ oxide powders are displayed in Figure 5.5. As can be observed (Figure 5.5), the series of oxides are made up of irregular-shaped particles and the morphology evolution is not significant with compositional changes. Therefore, the morphology is not considered as critical in interpreting the distinctive ORR given by the various $ZnCo_xMn_{2-x}O_4$ oxide catalysts. To understand the ORR properties given by Co substitution, the relationship between cation valence and ORR activity was first inspected since oxidation state was one of the most influential factors reported.[23] Specific ORR activity was correlated to Mn and Co oxidation state obtained from XAS analysis. To be specific, potentials required to drive a given specific current density was plotted as a function of Mn valence (Figure 5.6 a). Interestingly, the intrinsic activity exhibits a volcano shape as a function of Mn oxidation state (Figure 5.6 a). It is believed that the ORR descriptor can be identified from the Mn side in the designed $ZnCo_xMn_{2-x}O_4$ oxides, as it has been disclosed in earlier studies that Mn species were far more active than Co species in catalyzing ORR and researchers have claimed that Mn were the only active sites in the Mn-Co based oxides systems.[18, 23] As determined experimentally, a mixed Mn^{3+}/Mn^{4+} is essential for high ORR activities (Figure 5.6 a) in the Co-substituted spinel. This observation is qualitatively consistent with previous findings in Mn-Co based oxides.[18, 23] The critical role of Mn valence can be rationalized by how the electronic structure interact with the adsorbed oxygen according to early studies.[20] Enlightened by previous proposal that the e_g electron of octahedral-coordinated metal cations reveals the bonding strength between octahedral-site cations and oxygen,[20] the relationship between the intrinsic ORR activity and the Mn e_g electron (Figure 5.6 b) was further shown. It is well known that spinel and perovskites all share octahedron geometry that arranges in the form of edge-sharing and corner-sharing, respectively. Potential connections between the edge-sharing octahedra (spinel) and corner-sharing octahedra (perovskite) in catalyzing ORR are thus expected, and consequently, the volcano map (dash line in Figure 5.6 b) established in perovskites[20] are added for the purpose of comparison. Surprisingly, the relationship between Mn e_g electron and potentials (@25 $\mu A\ cm^{-2}{}_{ox}$) of spinel $ZnCo_xMn_{2-x}O_4$ generally fits with the inserted volcano map. Perfect match was found in spinel $ZnCo_xMn_{2-x}O_4$ with Co content increasing from 0.6 to 1.8. In contrast, the tetragonal counterparts subjected to severe Jahn-Teller distortion exhibit significant deviations from the volcano map, specifically, a much lower ORR activities were observed than that predicted from the e_g theory. Note that the volcano map developed in perovskites are mainly based on the series of transition metal-based cubic octahedron, the deviations can be ascribed to an elongated/compressed MnO_6 induced by Jahn-Teller distortion. To be specific, the $e_g{}^1$ electrons of Mn^{3+} tend to get stabilized in the tetragonal phase and disfavor the reductive coordination to O_2 as per the catalytic mechanism proposed by Yang's group, thus produce depressed ORR activities.[3]

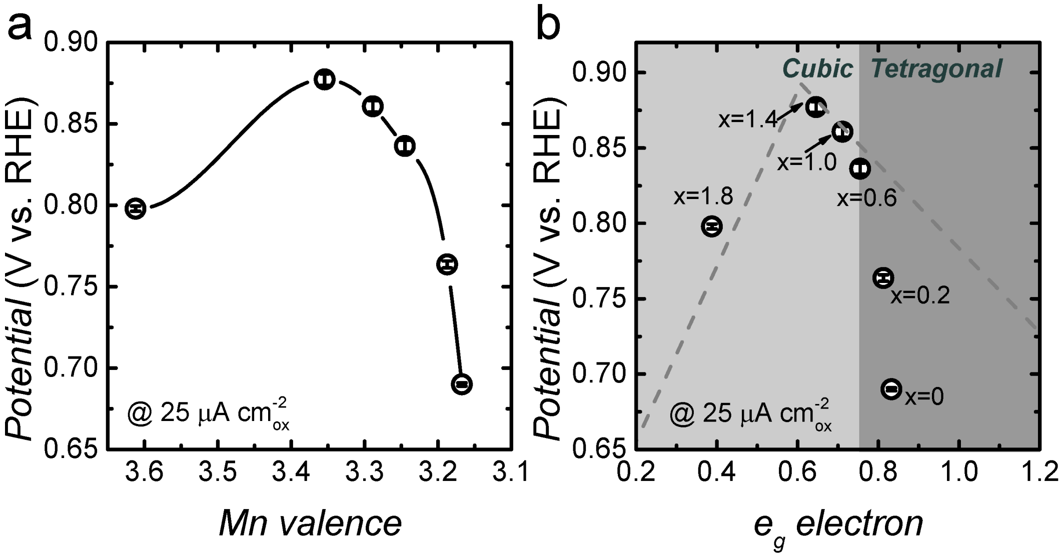

Figure 5.6 (a) Correlation between Mn valence state and ORR potentials at 25 μA cm^{-2}_{ox}. (b) ORR potentials at 25 μA cm^{-2}_{ox} as a function of e_g electron in $ZnCo_xMn_{2-x}O_4$. Dash line is the established volcano map (e_g theory) in Yang's work[20] regarding perovskite group.

5.4 Conclusion

As inactive Zn favors a tetrahedral bonding to oxygen atom, our design of spinel $ZnCo_xMn_{2-x}O_4$ create an ideal case where the catalytic activities of edge-sharing $[Co_xMn_{1-x}O_6]$ octahedra in spinel structure were exclusively inspected. Changes in the structure and cation valence were observed as Co gradually replaces Mn in the spinel oxides. The Mn-rich samples present as tetragonal spinel due to the Jahn-Teller distortion of Mn^{3+}, and the structure transit to cubic phase with an enhanced Co concentration. As Co progressively substituting into the spinel oxides, the Mn cations undergo oxidation to a mixed Mn^{3+}/Mn^{4+}. Notable enhancement in ORR activity was observed with the presence of both Mn and Co in octahedral sites. The highest ORR was achieved with a Co content (x) of 1.6 and approaches that of $LaMnO_{3+\delta}$. In addition to their superior ORR performance, the descriptor for electrocatalytic properties of $[Co_xMn_{1-x}O_6]$ octahedra was also identified. It is the e_g occupancy of active Mn cation which determines the catalysts' effective interaction to oxygen that dominates the activity of [$Co_xMn_{1-x}O_6$]. The e_g-ORR relationship established in this study match perfectly with the volcano map developed in perovskite from earlier studies in terms of the cubic $ZnCo_xMn_{2-x}O_4$ oxides. In contrast, the tetragonal counterparts show much lower ORR activities that are deviating from the volcano map. This could be due to the degenerated e_g orbitals of Mn^{3+}, where its e_g^1 electrons are stabilized and disfavor the reductive coordination to O_2. This work confirms the predominant role of spinel octahedra in contributing to oxygen reduction. Success in identify the descriptor for [$Co_xMn_{1-x}O_6$] activity bridges the linkage between edge-sharing and corner-sharing octahedra in different crystal structures and illustrate the applicability of e_g theory in [TMO_6]. These findings provide knowledge-guided design of efficient octahedron-containing oxide catalysts towards oxygen reduction and it opens new vision in fundamentally interpret the electrocatalysis by spinel family.

References

[1] I. Katsounaros, S. Cherevko, A. R. Zeradjanin, K. J. Mayrhofer, *Angew Chem Int Ed Engl* **2014**, 53, 102-121.
[2] C. Li, X. Han, F. Cheng, Y. Hu, C. Chen, J. Chen, *Nat. Commun.* **2015**, 6, 7345.
[3] F. Cheng, J. Shen, B. Peng, Y. Pan, Z. Tao, J. Chen, *Nat. Chem.* **2011**, 3, 79-84.
[4] J. Du, C. Chen, F. Cheng, J. Chen, *Inorg Chem* **2015**, 54, 5467-5474.
[5] H. Yang, F. Hu, Y. Zhang, L. Shi, Q. Wang, *Nano Res.* **2016**, 9, 207-213.
[6] Y. Liang, H. Wang, J. Zhou, Y. Li, J. Wang, T. Regier, H. Dai, *J. Am. Chem. Soc.* **2012**, 134, 3517-3523.
[7] E. Lee, J.-H. Jang, Y.-U. Kwon, *J. Power Sources* **2015**, 273, 735-741.
[8] A. Restovic, E. Rıos, S. Barbato, J. Ortiz, J. Gautier, *J Electroanal. Chem.* **2002**, 522, 141-151.
[9] A. Sutka, G. Mezinskis, *Front Mater. Sci.* **2012**, 1-14.
[10] H. Dau, P. Liebisch, M. Haumann, *Anal Bioanal Chem* **2003**, 376, 562-583.
[11] J.-H. Park, S. Cheong, C. Chen, *Phys. Rev. B* **1997**, 55, 11072.
[12] S. Malkhandi, P. Trinh, A. K. Manohar, A. Manivannan, M. Balasubramanian, G. S. Prakash, S. Narayanan, *J. Phys. Chem. C* **2015**, 119, 8004-8013.

[13] D. Makovec, A. Kodre, I. Arčon, M. Drofenik, *J Nanopart. Res.* **2009**, 11, 1145-1158.

[14] M. Sikora, Cz. Kapusta, K. Knížek, Z. Jirák, C. Autret, M. Borowiec, C. J. Oates, V. Procházka, D. Rybicki, D. Zajac, *Phys. Rev. B*, **2006**, 73, 094426.

[15] S. Calvin, E. Carpenter, B. Ravel, V. Harris, S. Morrison, *Phys. Rev. B* **2002**, 66, 224405.

[16] Y. Du, J.-o. Wang, L. Jiang, L. S. Borgna, Y. Wang, Y. Zheng, T. Hu, *J. Synchrotron Radiat.* **2014**, 21, 756-761.

[17] H. Y. Wang, S. F. Hung, H. Y. Chen, T. S. Chan, H. M. Chen, B. Liu, *J. Am. Chem. Soc.* **2015**, 138, 36-39.

[18] C. Wei, Z. Feng, G. G. Scherer, J. Barber, Y. Shao-Horn, Z. J. Xu, *Adv. Mater.* **2017**.

[19] C. Du, Q. Tan, G. Yin, J. Zhang, *Rotating Electrode Methods and Oxygen Reduction Electrocatalysts*, Elsevier, **2014**.

[20] J. Suntivich, H. A. Gasteiger, N. Yabuuchi, H. Nakanishi, J. B. Goodenough, Y. Shao-Horn, *Nat Chem* **2011**, 3, 546-550.

[21] Y. Liang, Y. Li, H. Wang, J. Zhou, J. Wang, T. Regier, H. Dai, *Nat. Mater.* **2011**, 10, 780-786.

[22] H. Liu, X. Zhu, M. Li, Q. Tang, G. Sun, W. Yang, *Electrochim. Acta* **2014**, 144, 31-41.

[23] K. A. Stoerzinger, M. Risch, B. Han, Y. Shao-Horn, *ACS Catal.* **2015**, 5, 6021-6031.

Chapter 6

Nano-size spinel ferrite oxides towards oxygen reduction reaction: Revealing the importance of surface chemistry

Significant progress has been made on oxide materials (e.g. perovskites, spinels, layered-oxides, and etc) towards ORR in recent years. While a nice correlation usually can be made between the ORR activity of oxides and their bulk thermochemistry, there are some contrary conclusions when using bulk chemistry to interpret the ORR of nano-size oxide catalysts. Using spinel $Mn_xFe_{3-x}O_4$ *oxides (5~12 nm) as model materials, it is found that the surface chemistry is indeed dominant in the ORR. The high surface/bulk ratio of nanoparticles gives a totally different surface composition. The near-surface Mn density revealed from an electrochemical approach strongly correlates to the distinctive ORR activity given by the various ferrite oxide catalysts. The interplay between the surface Mn density and Mn valence state co-determines the ORR performance of spinel* $Mn_xFe_{3-x}O_4$ *catalysts.*

---

*This chapter published substantially as Y. Zhou, S. Xi, J. Wang, S. Sun, C. Wei, Z. Feng, Y. Du, Z. J. Xu. *ACS Catal.* 8, 673−677 (2017).

6.1 Introduction

Oxygen reduction is a sluggish reaction limiting the efficiency of clean energy devices like the fuel cells, metal-air batteries.[1] The research on ORR catalyst development has been hot. In recent years, transition metal oxides have been one of hottest ORR electrocatalyst materials.[2-4] Significant progress has been made on perovskites, spinels, layered-oxides, and etc.[2, 5-6]

To facilitate efficient design of highly active oxide catalyst, great efforts have been devoted to the mechanism understanding and descriptor studies.[6-7] One interesting phenomenon is that a nice correlation usually can be made between the ORR activity of oxides and their bulk thermochemistry.[5, 7-8] For example, e_g electrons, O p-band center and crystal structures can be used to describe the ORR activity.[2, 8-10] However, the ORR is an electrochemical process, which occurs at the surface of oxide catalysts, instead of the region inside the bulk. A scaling relationship between the surface and bulk energetics has been built in perovskite oxides AMO_3 (A represents La or Sr, M represents metal from Sc to Ge) by researchers, consolidating the theory that the bulk thermochemistry is a good descriptor for the electrocatalytic activity of transition metal oxides.[11] It is known that the perovskite oxides are generally of micro-scale size, while ultra-small (< 10 nm) spinel oxide particles can be prepared by versatile approaches. For ultra-small size nanoparticles, the surface might be totally different with respect to their bulk and the scaling relationship between the surface and the bulk might no longer exist. Therefore, it is intriguing to study nano-size spinel oxides as ORR electrocatalysts.

In this chapter, a systematic study is presented to answer the question above: which chemistry should be given with more attention to nanosized oxides, bulk or surface chemistry? The manganese ferrite nanoparticles with various substitution ratio were taken as model materials and the bulk chemistry of $Mn_xFe_{3-x}O_4$ particles was carefully revealed by bulk-sensitive tools: XRD, XANES, and EXAFS. In addition, the classical surface chemistry tool, XPS, was employed to probe the surface chemistry. Interestingly, XPS gives similar information as those bulk chemistry tools did and it cannot provide a real surface information (due to the nanoparticles sizes (<10 nm) are within the probing depth of XPS technique). A pure electrochemical approach to probe the surface chemistry of these oxide nanoparticles is presented in this chapter. It is found that this “in-situ” approach revealed the real surface chemistry, which directly interprets the ORR activities of these oxide nanoparticles. The story presented here gives readers an overview on how important the surface chemistry is for the interpretation of transition metal oxides’ ORR. It concludes that surface chemistry is indeed dominant in determining the electrochemical process, a surface chemical process. This work is helping to solve the puzzle of oxide catalysts and it will encourage more attention and effort onto the surface of oxide nanoparticles.

6.2 Experimental details

Synthesis of $Mn_xFe_{3-x}O_4$ nanoparticles. Manganese ferrite nanoparticles were prepared according to an established facile wet chemical method.[12] Specifically, the synthesis started with dissolving $Mn(acac)_2$ and $Fe(acac)_3$ with a molar ratio of x: (3-x) in oleylamine. Then the mixture was dehydrated at 110°C for 1 hour, and then quickly heated to 300°C (heating rate: ~13°C min^{-1}) and aged at this temperature for an additional 1 hour under vigorous stirring in Argon atmosphere. After cooling, the resulting nanoparticles were first precipitated by centrifugation with addition of isopropanol. And then re-dispersed in hexane and repeated centrifugation by adding isopropanol. The as-prepared nanoparticles were finally kept in hexane for further usage.

Electrode preparation. The synthesized $Mn_xFe_{3-x}O_4$ nanoparticles were loaded onto Vulcan carbon (C) with a weight ratio of ~6:4 (NPs/C) through sonication of $Mn_xFe_{3-x}O_4$ nanoparticle dispersion and C in hexane for several hours in ice bath. The subsequent loading of $Mn_xFe_{3-x}O_4$ on C aims to prevent the aggregation of $Mn_xFe_{3-x}O_4$ nanoparticles. After the C-$Mn_xFe_{3-x}O_4$ were collected, they were annealed at 250°C for 2 hours (heating rate: 10°C min^{-1}) to remove the surfactant. The loading ratio of NPs/C is further confirmed by Thermogravimetric analysis (TGA) and Inductively coupled plasma-optical emission spectrometry (ICP-OES) tests. The C-$Mn_xFe_{3-x}O_4$ catalyst were dispersed in a mixture solution containing DI water, isopropanol (Volume ratio 4:1) and Nafion® perfluorinated resin solution (5 wt. % in lower aliphatic alcohols and water, contains 15-20% water, Sigma-Aldrich) to obtain a homogeneous ink with a concentration of 2 mg/ml. Then 10 µl ink was dropped onto the rotating disk electrode surface to yield a mass loading of 61.2 μg_{Ox} cm^{-2}_{disk}. After dry in air, the electrode was ready for electrochemical tests.

Electrochemical measurement. All electrochemical measurements were conducted with PINE Wave Driver 20 bi-potentiostat in a three-electrode glass cell where Pt wire acts as counter electrode, sample modified ring disk electrode (RDE) or rotating ring-disk electrode (RRDE) as working electrode and saturated calomel electrode (SCE) as reference electrode. Electrolyte used was 0.1 M KOH and potentials were calibrated to reversible hydrogen electrode (RHE). Prior to the ORR, the working electrode is scanned in Ar-saturated 0.1 M KOH (1.0~0.4 V vs. RHE) for the background current collection. During RRDE tests, the disk electrode was scanned cathodically from 1.0 to 0.4 V vs. RHE in O_2-saturated electrolyte, while the ring potential was hold constant at 1.3V vs. RHE to quickly oxidize the escaped hydroxide. Different rotating speed (100 rpm, 400 rpm, 900 rpm, 1600 rpm) were employed during the RRDE tests. The RRDE used is glassy carbon disk with gold ring. The collection efficiency of the RRDE calibrated is ~0.357.

6.3 Results and discussion

Manganese ferrite nanoparticles ($Mn_xFe_{3-x}O_4$) were prepared by a facile chemical method. To avoid the aggregation of the nanoparticles, the ferrite nanoparticles were subsequently loaded onto the Vulcan carbon support. Figure 6.1 shows the TEM images of the various $Mn_xFe_{3-x}O_4$/C. It can be seen that the nanoparticles are uniformly distributed on the Vulcan carbon.

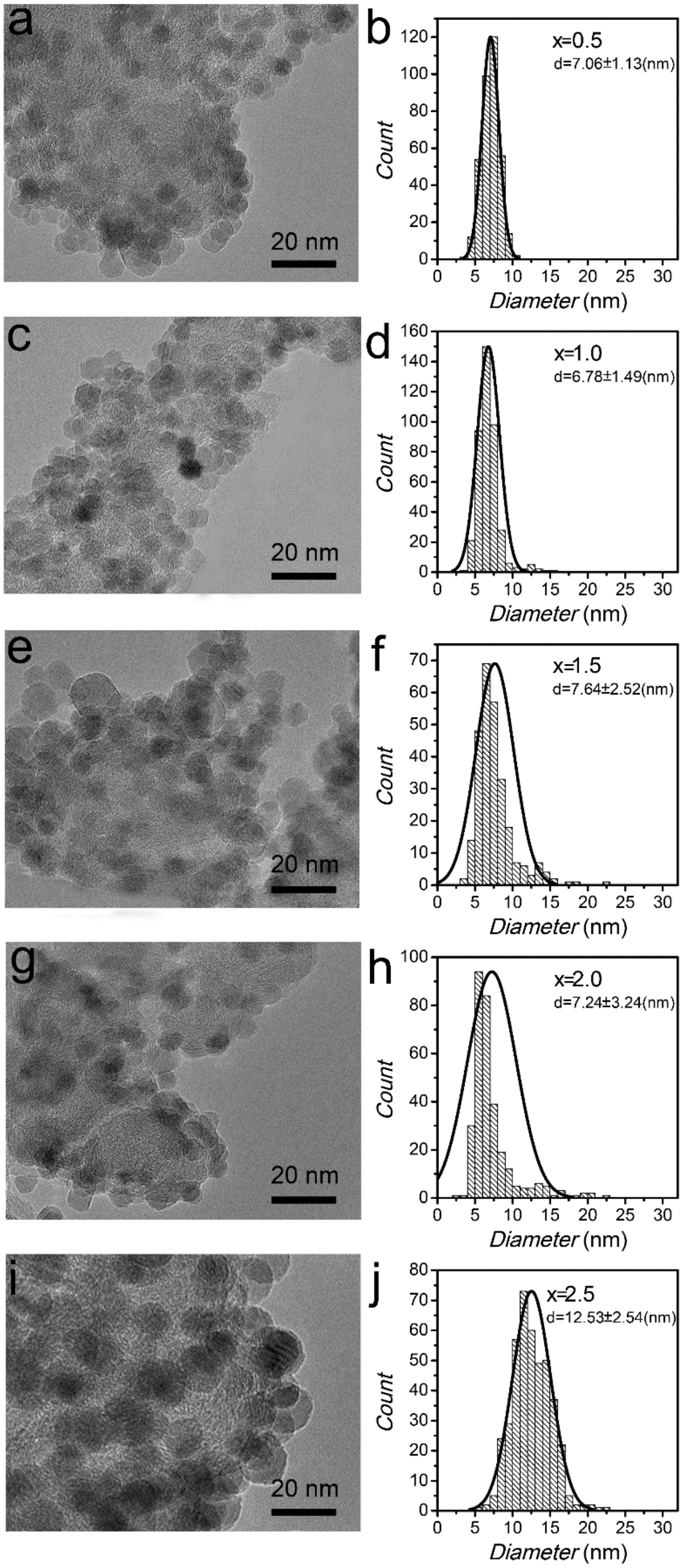

Figure 6.1 TEM images of $Mn_xFe_{3-x}O_4$/C and corresponding size distribution of $Mn_xFe_{3-x}O_4$ with a Mn fraction (x) of (a, b) 0.5, (c, d) 1.0, (e, f) 1.5, (g, h) 2.0 and (i, j) 2.5.

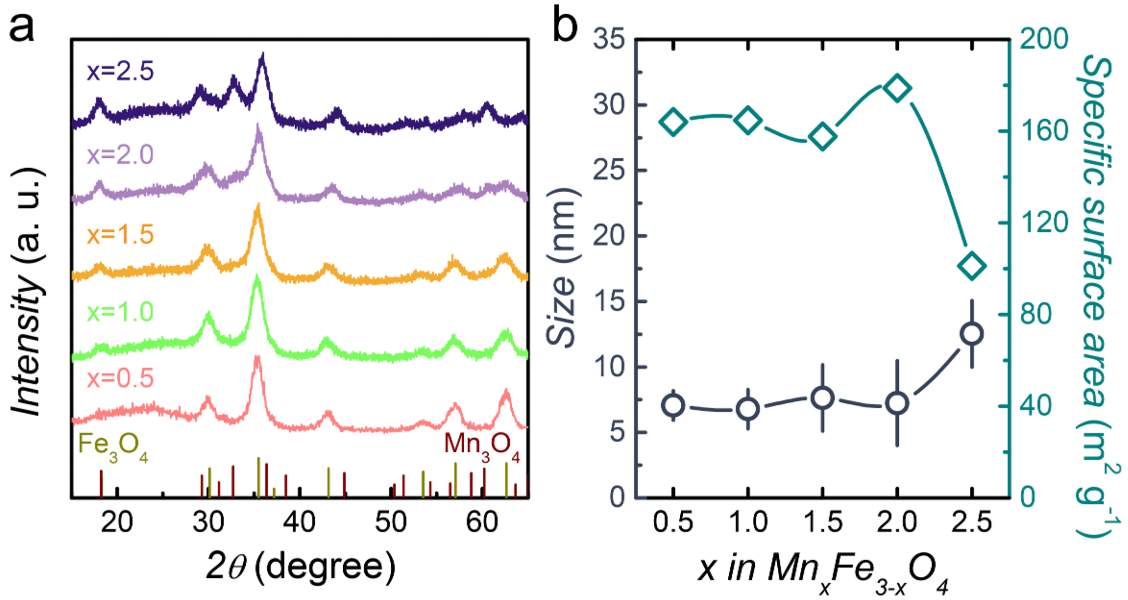

Figure 6.2 (a) XRD patterns of the $Mn_xFe_{3-x}O_4$ (x=0.5~2.5) catalyst. (b) The size distribution and specific surface area of $Mn_xFe_{3-x}O_4$ (x=0.5~2.5) oxides.

The crystal structure was first confirmed by XRD characterization. As displayed in Figure 6.2 a, Fe-rich manganese ferrite (x=0.5, x=1.0, x=1.5) possesses a single cubic spinel phase. In contrast, their Mn-rich counterparts (x=2.0 and x=2.5) are of a tetragonal phase due to Jahn-Teller distortion of MnO_6 at a relatively high Mn concentration.[13] According to literature findings, the cubic-tetragonal transition in $Mn_xFe_{3-x}O_4$ becomes prominent when Mn fraction (x) is beyond 1.74~1.84.[13] The cubic-to-tetragonal transition threshold (a Mn fraction of 1.5~2.0) observed in the as-prepared ferrites is consistent with the literature reports. The synthesized $Mn_xFe_{3-x}O_4$ particles are relatively uniform in size and remain within a range of 6~13 nm (Figure 6.2 b). This size information is obtained by counting the diameters of at least 200 nanoparticles from the TEM images (Figure 6.1). Given the particle size (d) and the ferrite theoretical densities (ρ) (shown in Table 6.1), the surface areas of the ferrite particles were obtained according to the following equation, assuming that the particles are spherical and without internal porosity.[14]

$$Surface\ area = \frac{6 \times 10^3}{\rho * d}$$

The surface area results are given in Figure 6.2 b.

Table 6.1 Theoretical density (ρ), mean ferrite particle diameters (d) obtained from TEM images and calculated surface area of the various $Mn_xFe_{3-x}O_4$ nanoparticles.

Mn fraction (x)	Density ρ (g/cm^3)	Reference link	Average diameter (nm)	Surface area (m^2/g)
x=0.5	5.18	http://materials.springer.com.ezlibproxy1.ntu.edu.sg/isp/crystallographic/docs/sd_0306168	7.06	164.07
x=1.0	5.368	http://s.b5z.net/i/u/10091461/f/MSDS-NANOPOWDERS/US3910.pdf	6.78	164.86
x=1.5	4.98	http://materials.springer.com/isp/crystallographic/docs/sd_0383249	7.64	157.70
x=2.0	4.67	https://materialsproject.org/materials/mp-770096/	7.24	177.46
x=2.5	4.87	http://materials.springer.com.ezlibproxy1.ntu.edu.sg/isp/crystallographic/docs/sd_0305722	12.53	98.33

The cation valence states were examined by surface-sensitive XPS and bulk-sensitive XANES. The XPS spectrum of Mn $2p^{3/2}$ signal was deconvoluted and shown in Figure 6.3 a. The two sub-peaks with binding energies at ~641. 89 eV and 640.78 eV can be assigned to Mn^{3+} and Mn^{2+}, respectively,[15] and the peak area ratio helps quantify the average Mn oxidation state. It is interesting to note that the average Mn oxidation state in x=1.0 is of the lowest (~2.6+) and an enhanced presence of Mn^{3+} could be observed in the other compositions. As for Fe, it possesses a valence state of ~3+ in all of the compositions because the Fe $2p^{3/2}$ peaks were consistently observed at ~711.3 eV[16] (Figure 6.3 b). The XANES spectra of $Mn_xFe_{3-x}O_4$ at Mn and Fe K edge are displayed in Figure 6.3 c and 6.3 d. The adsorption edge energies act as a strong indicator of the valence state of metal elements. For Fe spectra, the adsorption edges almost overlap with that of the reference Fe_2O_3, indicating the presence of Fe^{3+} in all the ferrite samples. In contrast, the Mn K edge spectra exhibits certain shifts in edge position. An integral method was employed to determine the edge position energies for the Mn spectra. As shown in the inset of Figure 6.3 c, the Mn edge position in x=1.0 is of lowest compared with the rest four. It indicates that the sample x=1.0 has a relatively lower Mn oxidation state, which is, in fact, consistent with the XPS results. Thus it is convinced that the cation valence states information probed by surface and bulk sensitive characterization technique is qualitatively consistent.

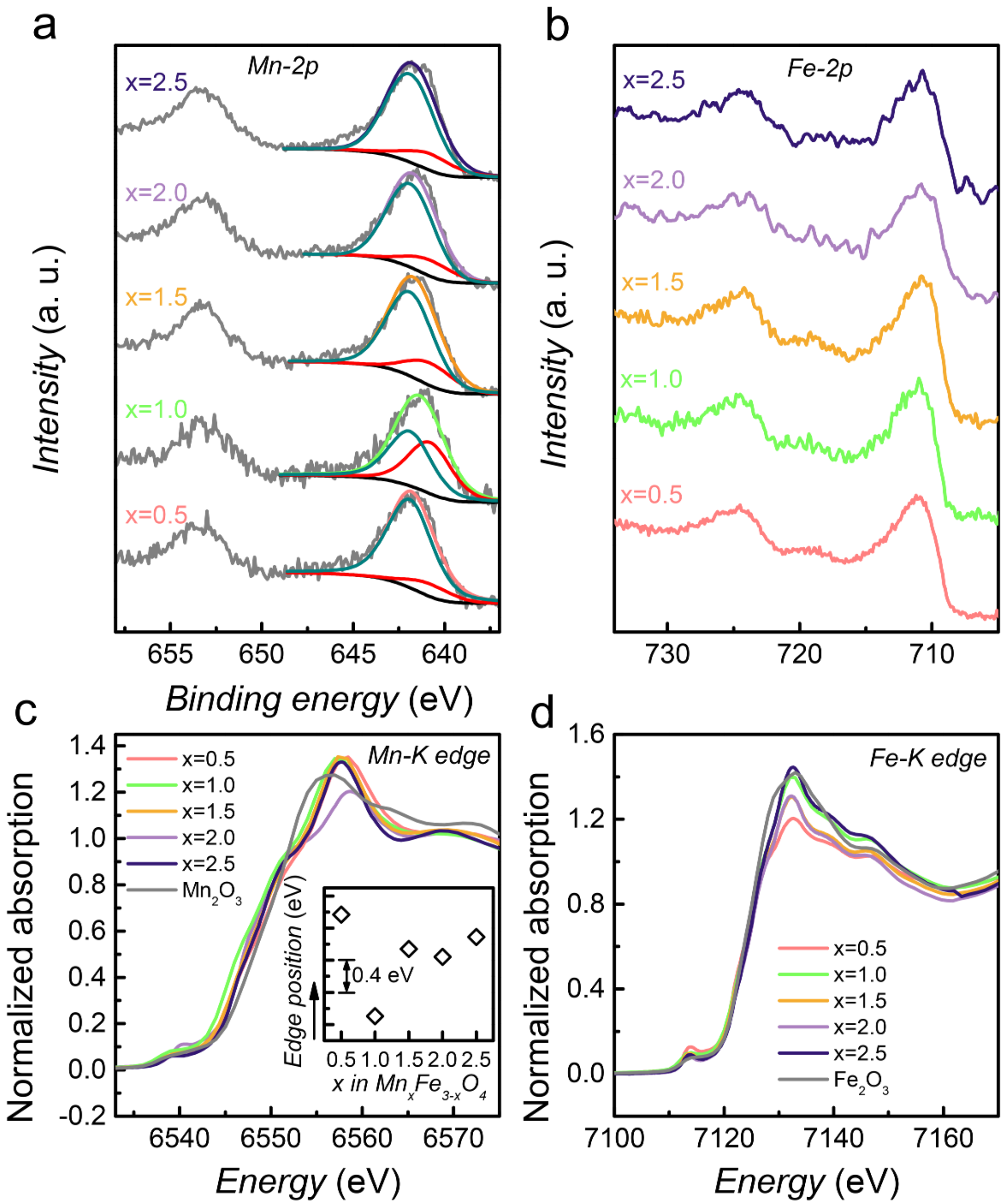

Figure 6.3 (a) Mn 2p XPS spectra (fitted) and (b) Fe 2p XPS spectra. (c) Normalized XANES spectra for $Mn_xFe_{3-x}O_4$ (c) Mn K-edge and (d) Fe K-edge. The inset in (c) shows the Mn edge positions determined by an integral method.

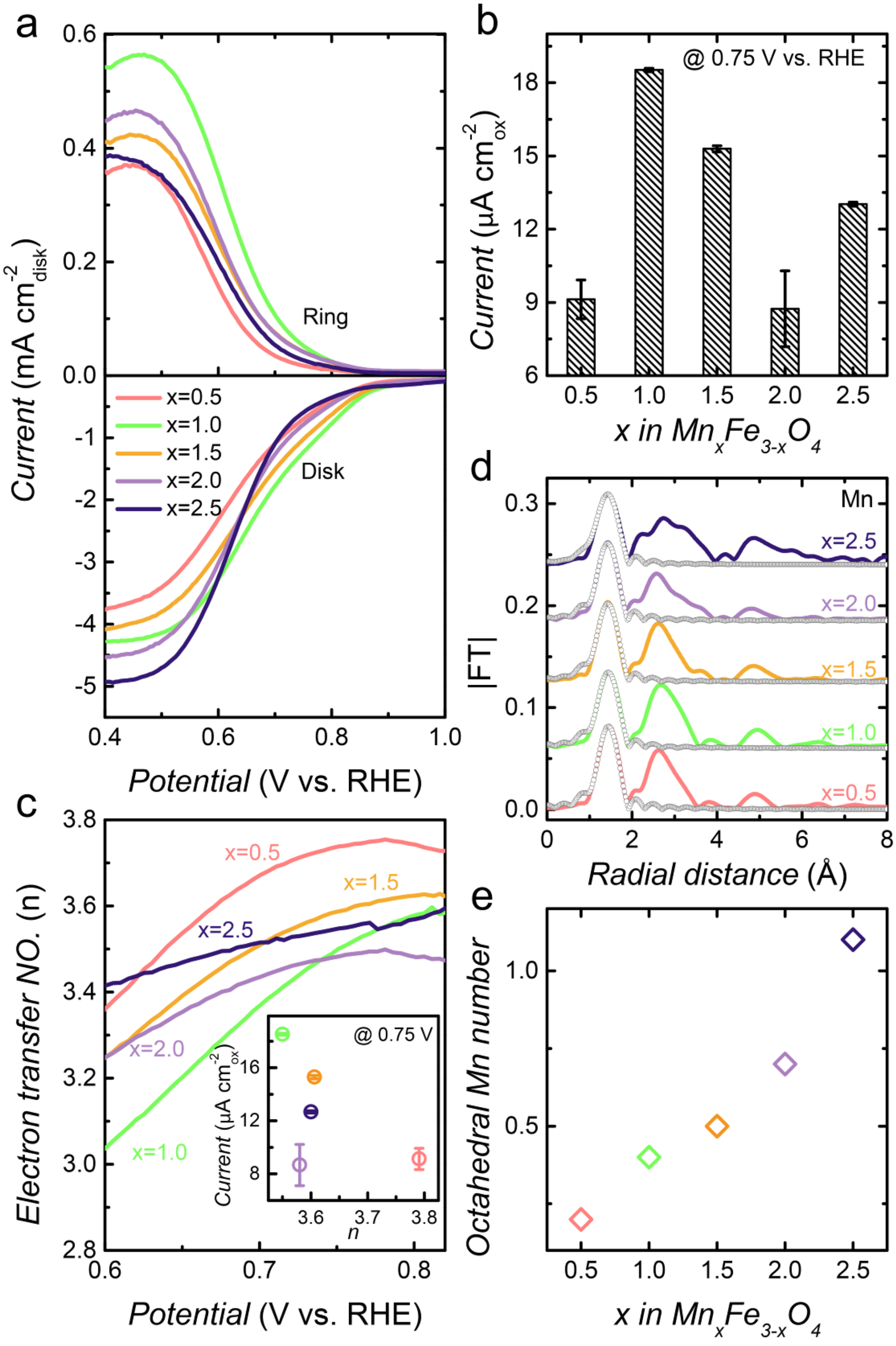

Figure 6.4 (a) ORR polarization curves (disk and ring current) of $Mn_xFe_{3-x}O_4$ catalysts at a

rotating speed of 1600 rpm. (b) ORR specific activity displayed as current densities at a fixed potential of 0.75V vs. RHE. (c) Calculated electron transfer number as a function of potential, inset is the ORR specific current as a function of the electron transfer number at a potential of 0.75V vs. RHE. (d) Fourier transformed EXAFS spectra at Mn K-edge (colored curves) and corresponding fitting curves (grey curves). (e) The octahedral Mn number determined by the EXAFS fitting.

The ORR performance of $Mn_xFe_{3-x}O_4$ were investigated by rotating ring-disk electrode (RRDE) technique. The RRDE measurements can determine the reaction kinetics and at the same time probe the peroxide intermediate formation during ORR from which the electron transfer number (n) in oxygen reduction process can be obtained. The representative ORR curves in 0.1 M KOH at a rotating speed of 1600 rpm are shown in Figure 6.4 a. The ORR specific activity was first determined from the collected disk currents. Specifically, the specific current densities (current normalized by the oxide surface area after background, mass transport and iR correction) at a fixed potential of 0.75 V vs. RHE were plotted in Figure 6.4 b. As illustrated, the investigated ferrite catalysts with a Mn fraction (x) of 1.0 affords the highest current, which is double the current density given by x=0.5. It is worth noting that the Mn is widely considered as the active element in oxides towards ORR because it is redox active within the ORR potential region. As shown in Figure 6.4 b, an increased Mn concentration beyond x = 1.0 does not further promote the ORR activity. Instead, the overall trend displays a non-linear tendency resembling the letter of "N". To understand the ORR trend in Figure 6.4 b, the ring currents recorded at a constant voltage of 1.3 V vs. RHE was analyzed. The ring current is an indication of the liberation of intermediate peroxide during the ORR process.[17] It is notable that the catalyst x=1.0 produces the highest ring current rising at a more positive potential than the rest ferrite oxides. The electron transfer numbers within the ORR potential region can be obtained by the following equation:[17]

$$n = \frac{4I_dN}{I_dN + I_r}$$

N is the collection efficiency of the rotating ring disk electrode, I_r is the ring current and I_d is the disk current. As indicated by the above equation, the n should be independent of catalyst loading or surface active site density and reflects the intrinsic activity of a given catalyst. The extracted potential dependent electron transfer numbers for the various ferrite catalysts are plotted in Figure 6.4 c. The $Mn_xFe_{3-x}O_4$ catalysts exhibits a combined $2e^-$ and $4e^-$ transfer in oxygen reduction, as indicated by the electron transfer numbers which range between 3 ~ 4. Since an efficient ORR generally means a $4e^-$ transfer, it is convinced that the $Mn_xFe_{3-x}O_4$ with a Mn fraction (x) of 0.5 has the highest Mn intrinsic activity (if consider the Mn as the major contributor of ORR). In contrast, the Mn intrinsic activity in composition x=1.0 is considered low because catalyst $MnFe_2O_4$ possesses the lowest overall electron transfer number. The tetragonal spinel ferrite oxides (x=2.0 and x=2.5) have similar electron transfer numbers that are higher than that of x=1.0. From the electron transfer number analysis, it is convinced that the intrinsic activity of Mn in the $Mn_xFe_{3-x}O_4$ oxides exhibit substantial differences (consider Mn as the major ORR contributor in $Mn_xFe_{3-x}O_4$ oxides). If such a difference can entirely account for the ferrite oxides' distinctive ORR, a positively linear correlation between electron transfer number and ORR activities are expected. The ORR specific current densities plotted as a function of the electron transfer numbers at a potential of 0.75 V vs. RHE are provided in the inset of Figure 6.4 c. Intriguing discrepancies are observed. To be specific, catalyst x=1.0 produced the highest specific current but it has the lowest electron transfer number. On the contrary, catalyst x=0.5 affords a much lower current on proceeding through a higher electron transfer pathway. Therefore, the activity difference could be due to an interplay between several factors.

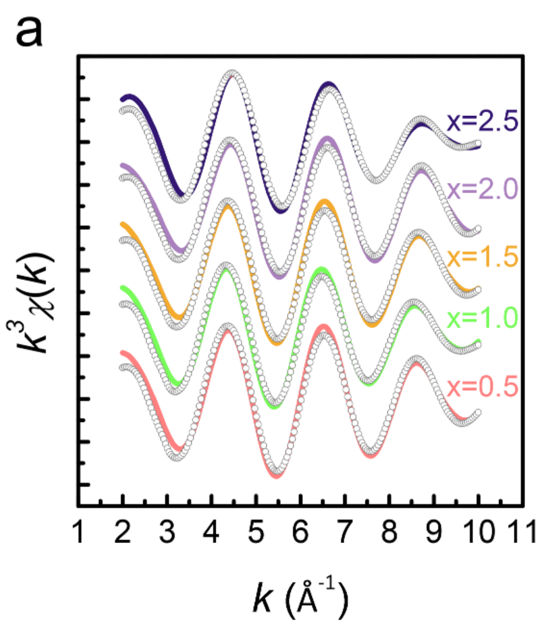

Figure 6.5 (a) Filtered EXAFS data by inverse FT from the FT data (1.0 – 1.9Å) along with the fitting curves obtained for spinel $Mn_xFe_{3-x}O_4$. (b) Reconstructed atom distribution function (ADF).

Since *n* reflects the intrinsic activity of a given catalyst or the major activity contributor, i.e. the Mn in the investigated $Mn_xFe_{3-x}O_4$ oxides, and are independent of the active species concentration, a change in the Mn concentration in $Mn_xFe_{3-x}O_4$ was proposed to be the catalytically critical factor that was underestimated. As spinel have two geometric sites (i.e. tetrahedral and octahedral), it is possible that the Mn gives totally different activity in different coordination environment. This is supported by the recent findings of geometric site-dependent ORR/OER in various oxide families, including perovskites and spinel.[18-20] Therefore, the cation distribution of Mn in $Mn_xFe_{3-x}O_4$ was probed by the curve fitting of EXAFS. A new EXAFS data analysis method, atom distribution function (ADF), which has three-time higher spatial resolution than conventional methods,[21] was applied to resolve the first Mn-O peak around 1.45 Å. As shown in Figure. 6.5, two kinds of Mn-O bond length were resolved. The shorter one is contributed by Mn-O_4 tetrahedral and the longer one is contributed by Mn-O_6 octahedral. The detailed structural information is listed in Table 6.2. Based on the parameters obtained from ADF method, a further fitting using Winxas were performed in R space and the fitting curves together with the FT data are shown in Figure. 6.4 d. Based on the coordination numbers, the ratio of Mn-O_6 in each sample can be estimated by the following equation:[21]

$$R_{Mn} = \frac{4 \times N\ (MnO_6)}{6 \times N\ (MnO_4) + 4 \times N\ (MnO_6)}$$

where N (Mn-O_6) is the coordination number of Mn-O_6 octahedral and N (Mn-O_4) is the coordination number of Mn-O_4 tetrahedral. The Mn occupancy (x_{Mn}) in $Mn_xFe_{3-x}O_4$ can be subsequently given by the following equation:

$$x_{Mn} = x \times R_{Mn}$$

Table 6.2 Summary of the EXAFS fitting results for $Mn_xFe_{3-x}O_4$ (x=0.5~2.5). Bond length (Mn-O_4 and Mn-O_6), Coordination number (N) and Mn occupancy (x_{Mn}) in tetrahedral site and octahedral site obtained by fitting the experimental EXAFS spectra.

Mn fraction (x)	Bond	N	R (Å)	σ^2 (Å^2)	x_{Mn}
x=0.5	Mn-O_4	2.1 (±0.2)	1.88 (±0.01)	0.0016 (±0.0003)	0.3
	Mn-O_6	2.0 (±0.2)	2.02 (±0.01)	0.0016 (±0.0003)	0.2
x=1.0	Mn-O_4	2.0 (±0.2)	1.88 (±0.01)	0.0016 (±0.0003)	0.6
	Mn-O_6	2.0 (±0.2)	2.03 (±0.01)	0.0016 (±0.0003)	0.4
x=1.5	Mn-O_4	2.1 (±0.2)	1.88 (±0.01)	0.0016 (±0.0003)	1.0
	Mn-O_6	1.7 (±0.2)	2.03 (±0.01)	0.0016 (±0.0003)	0.5
x=2.0	Mn-O_4	2.0(±0.2)	1.87(±0.01)	0.0016 (±0.0003)	1.3
	Mn-O_6	1.6(±0.2)	2.01(±0.01)	0.0016 (±0.0003)	0.7
x=2.5	Mn-O_4	1.7(±0.2)	1.83(±0.01)	0.0016 (±0.0003)	1.4
	Mn-O_6	2.1(±0.2)	1.97(±0.01)	0.0016 (±0.0003)	1.1

The Mn occupancy in octahedral site is plotted in Figure 6.4 e. In an effort to eliminate the effects of Mn concentration, the ORR current density (μA cm^{-2}_{ox}) was corrected to the bulk Mn fraction (x) in $Mn_xFe_{3-x}O_4$ and to the Mn number in tetrahedral and octahedral site, respectively (shown in Figure 6.6 a). The activity trends are totally different from the observed "N"-shaped trend in Figure 6.4 b. Due to its influencing role metal oxidation state in electrocatalytic reactions,[5, 15] the valence state of Mn was correlated with the bulk Mn number corrected- and Mn site occupancy-corrected ORR activities and the correlations are displayed in Figure 6.6 b-6.6 d. The random distribution of ORR activity versus Mn oxidation state indicates the elusive origin of the distinctive activity trend.

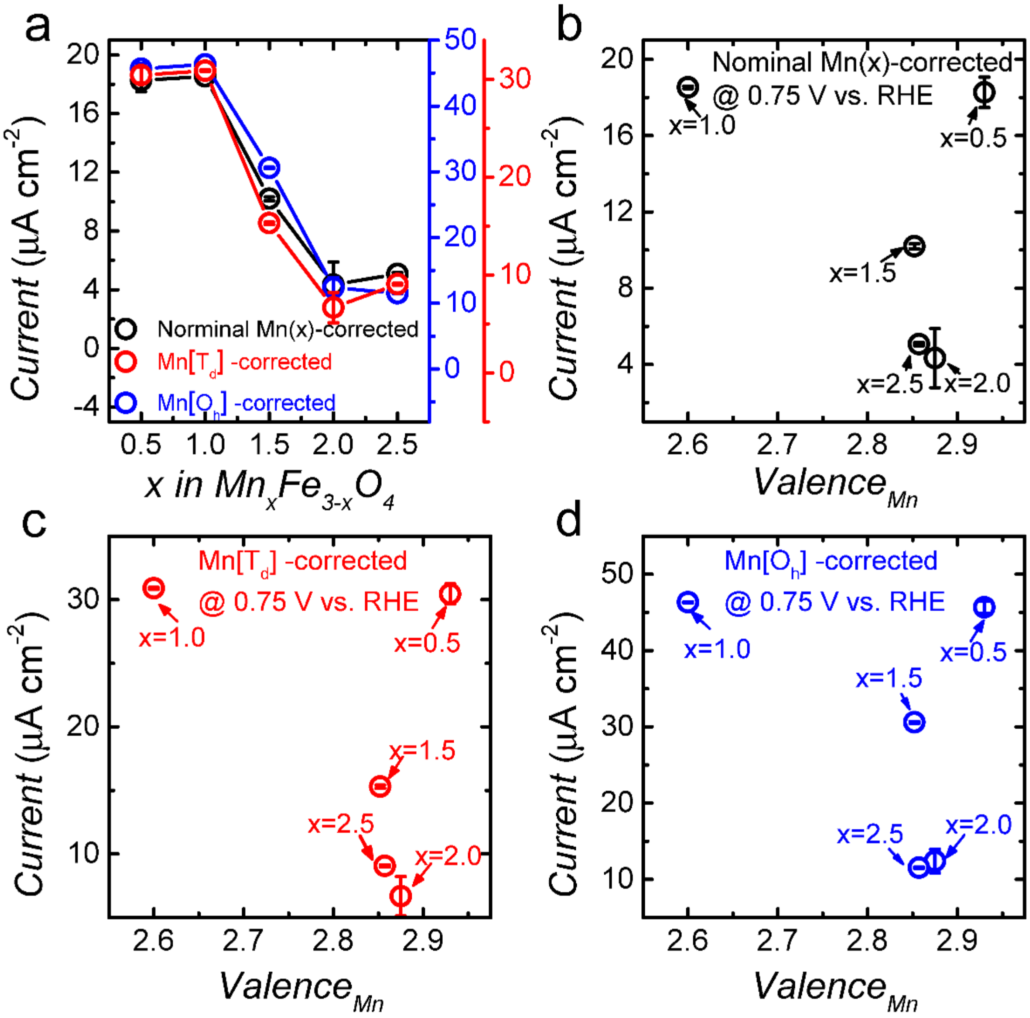

Figure 6.6 (a) Nominal Mn content-corrected, Mn tetrahedral occupancy, and octahedral occupancy corrected ORR activity of spinel $Mn_xFe_{3-x}O_4$; (b) Mn valence as a function of ORR activity corrected by the nominal Mn fraction (x); (c) Mn valence as a function of Mn tetrahedral occupancy corrected ORR activity in $Mn_xFe_{3-x}O_4$; (d) Mn valence as a function of Mn octahedral occupancy corrected ORR activity in $Mn_xFe_{3-x}O_4$. The ORR activity was presented as the current densities at a fixed potential of 0.75 V vs. RHE.

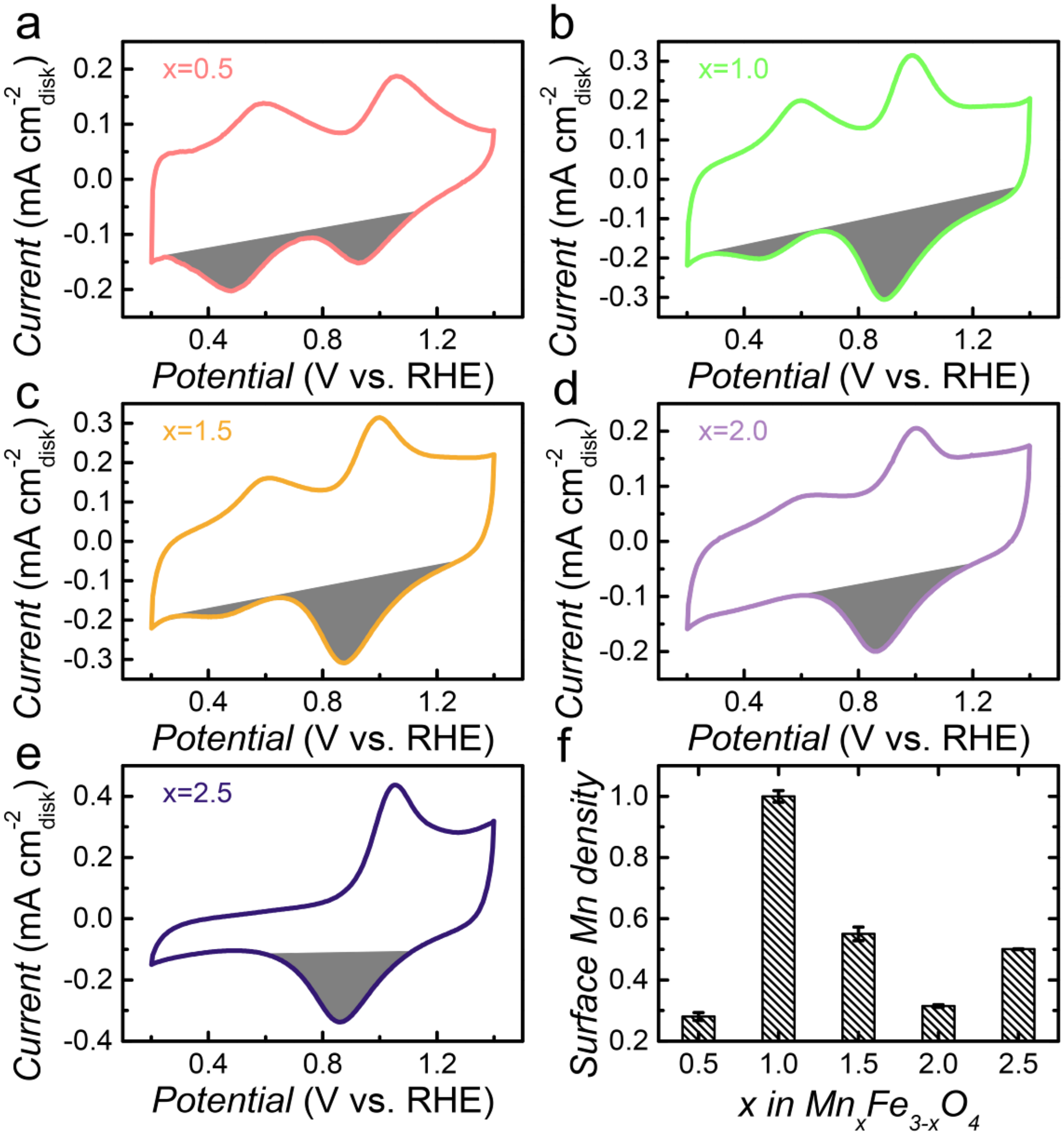

Figure 6.7 Cyclic voltammetry of $Mn_xFe_{3-x}O_4$ catalysts with a Mn concentration (x) of (a) 0.5, (b) 1.0, (c) 1.5, (d) 2.0 and (e) 2.5 at a scan rate of 10 mV s^{-1} in Ar-saturated 0.1 M KOH. (f) The surface Mn density calculated for the various $Mn_xFe_{3-x}O_4$ catalysts.

In alkaline electrolyte, the well-defined redox signals of transition metal species can be collected by electrochemical CV scan, giving sufficient information about the dynamics of redox-active species at the oxide surface.[22-23] The CV of curves of spinel $Mn_xFe_{3-x}O_4$ were recorded in Ar-saturated 0.1 M KOH within a potential region of 0.2 V to 1.4 V (vs. RHE). As shown in Figure 6.7 a-e, the various ferrite catalysts show prominent redox peaks associated with the reduction and oxidation of Mn. More interestingly, the redox peak current varies along with the compositional change, suggesting that the electrochemically exposed Mn site density is different. Since the redox of Fe in oxide occurs at more negative potentials than the potential window applied,[24] negligible contributions from Fe to the redox current are assumed. An integration method was employed to quantitatively determine the surface Mn density on the oxide near-surface.[23] To be specific, the cathodic response reflecting the evolution of Mn from its original oxidation state (obtained from XPS) to Mn^{2+} was integrated to extrapolate the near-surface Mn density. The effective Mn density can be calculated by the following equation:[23]

$$Mn\ density = \frac{Q}{(V_{Mn} - 2) * F}$$

where Q is the cathodic faradaic charge, V_{Mn} is the initial Mn oxidation state, F is the Faraday constant.

Table 6.3 Mn oxidation state obtained from XPS, faradaic charge associated with the reduction of surface Mn, determined effective Mn density at the oxide surface.

Mn fraction (x)	Mn valence (XPS results)	Charge Q (C)	Surface Mn density (relative)
x=0.5	2.89	(6.33 ± 0.252)E-4	0.281 ± 0.013
x=1.0	2.53	(12.80 ± 0.241)E-4	1.000 ± 0.0188
x=1.5	2.80	(10.70 ± 0.168)E-4	0.551 ± 0.0224
x=2.0	2.84	(6.41 ± 0.084)E-4	0.315 ± 0.0045
x=2.5	2.82	(10.00 ± 0.024)E-4	0.500 ± 0.0013

The cathodic redox response was presented by the grey filling area (Figure 6.7) through a linear background subtraction based on the David's work.[23] The filling area in Figure 6.7 a-e was integrated as the cathodic charge Q. Note that the the open circuit potentials of oxides are generally positive than the onset of the first reduction wave of $Mn_xFe_{3-x}O_4$ observed at ~0.9 V (vs. RHE),[23] the characterized Mn oxidation state by XPS was considered as the initial oxidation state in the potential range inspected. The integrated reduction charges and the determined surface Mn density are summarized in Table 6.3. The surface Mn density plotted in Figure 6.7 f indicates that the electrochemically accessible Mn number significantly differs from the nominal Mn concentration. The actual composition is also confirmed by the XPS and ICP. As shown in Figure 6.8, the ICP results are consistent with the nominal composition because ICP technique is bulk-sensitive. In contrast, the Mn/Fe atomic ratios obtained by XPS show some deviations. To be specific, the Mn/Fe ratio (XPS) in spinel $Mn_xFe_{3-x}O_4$ (x= 0.5 and 1.0) is slightly higher than the Mn/Fe bulk ratio. On the contrary, the other $Mn_xFe_{3-x}O_4$ oxides (x=1.5, 2.0, 2.5) show a Mn/Fe ratio that is lower than that in the bulk. Comparing the composition results obtained from the surface-sensitive XPS and from the CV analysis, significant differences can still be observed. It is convinced that the XPS techniques exhibit limitations in probing the outermost surface information of ultra-small nanoparticles. The nanoparticle size of the various $Mn_xFe_{3-x}O_4$ oxides are within the average depth (5~10 nm) from which the XPS signals are collected. Thus, it is very likely that XPS signals are mainly from the bulk region of the $Mn_xFe_{3-x}O_4$ oxides. This is also supported by the fact that the valence state information extracted from the surface-sensitive XPS and bulk-sensitive XANES is quite consistent.

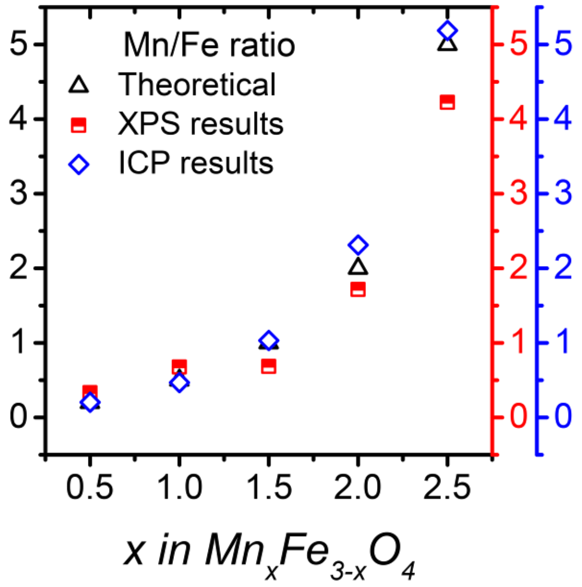

Figure 6.8 Atomic ratio of Mn/Fe obtained from ICP test and XPS in comparison with the nominal Mn/Fe ratio.

It is important at this stage to uncover the interplay between surface Mn density and their distinctive ORR. First, the specific ORR activity was corrected to the relative surface Mn density obtained from the CVs. As displayed in Figure 6.9 a, the rationalized activity exhibits a totally different trend compared with the oxide activity (Figure 6.4 b), where the former acts as a strong indicator of Mn intrinsic activity. As can be observed, the Mn-density corrected-activity, reflecting the intrinsic activity of Mn, decreases in the sequence: x=0.5, x=1.5, x=2.0, x=2.5 and x=1.0. In fact, these observations are in good agreement with the RRDE electron transfer number analysis. To probe the relationship between Mn valence state and the rationalized activity, Figure 6.9 b was further plotted. It is clear that increasing Mn oxidation state positively affects the Mn-density-corrected ORR activity (as indicated by the dash line), demonstrating that Mn^{3+} is more active than Mn^{2+} because the high spin Mn^{3+} fulfills a moderate e_g filling.[25]

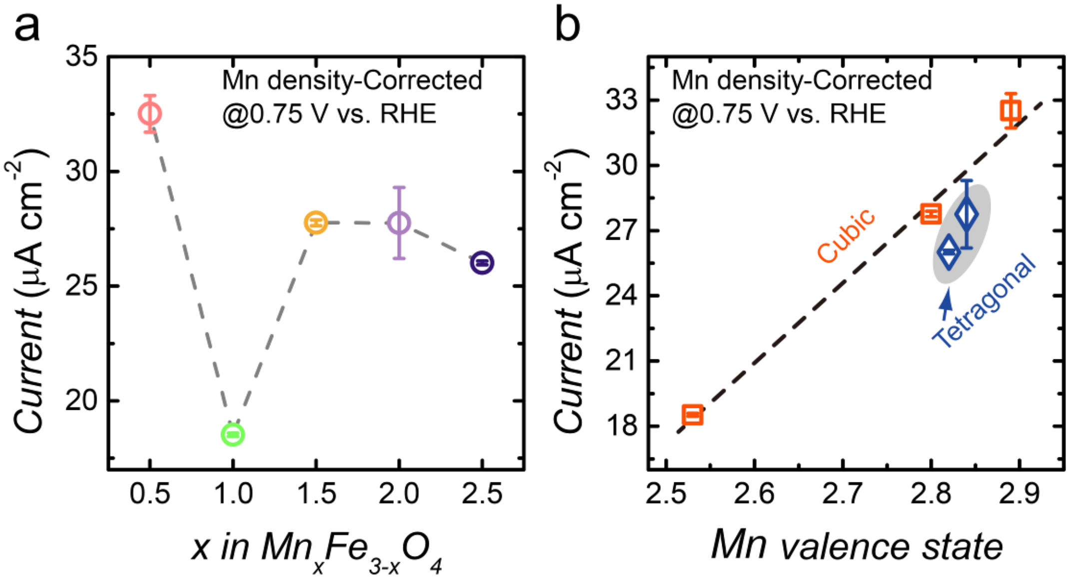

Figure 6.9 (a) ORR specific activity corrected by relative Mn density. (b) Correlation between Mn valence state and corrected specific activity.

The tetragonal spinel oxides (x=2.0 and 2.5) exhibit a slightly down-shifted ORR activity from the dash line. This is because the tetragonal spinel oxides have a weaker oxygen adsorption ability than the cubic counterparts[26] which is supported by the O 1s XPS spectrum. The deconvolution of the O 1s spectrum for the various $Mn_xFe_{3-x}O_4$ spinel catalysts are shown in Figure 6.10. The O1s spectra was deconvoluted into two peaks centered at ~529.9 and ~531.7, corresponding to lattice oxygen and surface adsorbed oxygen species, respectively.[26] The strong signal given by the surface adsorbed oxygen species in the cubic phase indicates that the cubic $Mn_xFe_{3-x}O_4$ oxides (x=0.5, 1.0 and 1.5) have a stronger oxygen adsorption ability than the tetragonal ferrites (x=2.0 and 2.5).

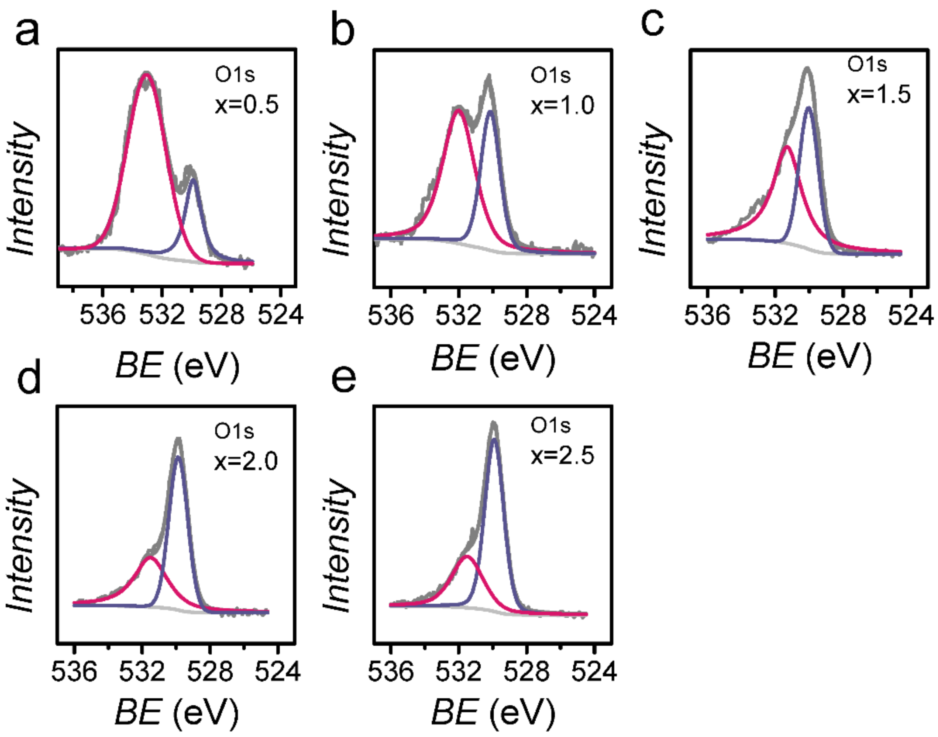

Figure 6.10 O1s spectra of spinel $Mn_xFe_{3-x}O_4$ oxide with a Mn fraction (x) of (a) 0.5, (b) 1.0, (c) 1.5, (d) 2.0 and (e) 2.5.

6.4 Conclusion

In summary, nano-size spinel $Mn_xFe_{3-x}O_4$ (x=0.5~2.5) oxides were examined as ORR electrocatalysts. A fundamental understanding of the composition-dependent ORR was revealed from the interplay between surface Mn density and Mn valence state. Owing to the mismatch between nanoparticle surface and bulk, the near-surface Mn density in $Mn_xFe_{3-x}O_4$ nanoparticles was found to be significantly different from the bulk composition. The near-surface Mn density was extracted by integrating the electrochemical Faradaic charges of Mn triggered in alkaline solution. While surface-sensitive XPS technique exhibits certain limitations for particles with sizes ranging between 5~10 nm, the integration method acts as an effective way to examine the surface information of ultra-small oxide nanoparticles. The surface Mn density has been identified as one dominating parameter towards ORR. The significant surface-bulk mismatch makes the surface chemistry more catalytically critical to oxide nanoparticles towards electrocatalysis.

References

[1] F. Cheng, J. Chen, *Chem. Soc. Rev.* **2012**, 41, 2172-2192.

[2] W. T. Hong, M. Risch, K. A. Stoerzinger, A. Grimaud, J. Suntivichb, Y. Shao-Horn, *Energy Environ. Sci* **2015**, 8, 1404-1427.

[3] C. C. McCrory, S. Jung, J. C. Peters, T. F. Jaramillo, *J. Am. Chem. Soc.* **2013**, 135, 16977-16987.

[4] R. Othman, A. L. Dicks, Z. Zhu, *Int. J. Hydrogen Energy* **2012**, 37, 357-372.

[5] K. A. Stoerzinger, M. Risch, B. Han, Y. Shao-Horn, *ACS Catal.* **2015**, 5, 6021-6031.

[6] J. Suntivich, H. A. Gasteiger, N. Yabuuchi, H. Nakanishi, J. B. Goodenough, Y. Shao-Horn, *Nat Chem* **2011**, 3, 546-550.

[7] F. Calle-Vallejo, N. G. Inoglu, H.-Y. Su, J. I. Martínez, I. C. Man, M. T. Koper, J. R. Kitchin, J. Rossmeisl, *Chemical Science* **2013**, 4, 1245-1249.

[8] Y.-L. Lee, J. Kleis, J. Rossmeisl, Y. Shao-Horn, D. Morgan, *Energy & Environmental Science* **2011**, 4, 3966-3970.

[9] J. Suntivich, H. A. Gasteiger, N. Yabuuchi, H. Nakanishi, J. B. Goodenough, Y. Shao-Horn, *Nat. Chem.* **2011**, 3, 546-550.

[10] A. Grimaud, K. J. May, C. E. Carlton, Y. L. Lee, M. Risch, W. T. Hong, J. Zhou, Y. Shao-Horn, *Nat Commun* **2013**, 4, 2439.

[11] F. Calle-Vallejo, O. A. Díaz-Morales, M. J. Kolb, M. T. M. Koper, *ACS Catal.* **2015**, 5, 869-873.

[12] C. Wei, Z. Feng, M. Baisariyev, L. Yu, L. Zeng, T. Wu, H. Zhao, Y. Huang, M. J. Bedzyk, T. Sritharan, Z. J. Xu, *Chem. Mater.* **2016**, 28, 4129-4133.

[13] V. Brabers, *J. Phys. Chem. Solids* **1971**, 32, 2181-2191.

[14] P. Ferreira, Y. Shao-Horn, D. Morgan, R. Makharia, S. Kocha, H. Gasteiger, *J. Electrochem. Soc.* **2005**, 152, A2256-A2271.

[15] Q. Tang, L. Jiang, J. Liu, S. Wang, G. Sun, *ACS Catal.* **2014**, 4, 457-463.

[16] G. Huang, E. He, Z. Wang, H. Fan, J. Shangguan, E. Croiset, Z. Chen, *Ind. Eng. Chem. Res.* **2015**, 54, 8469-8478.

[17] C. Du, Q. Tan, G. Yin, J. Zhang, *Rotating Electrode Methods and Oxygen Reduction Electrocatalysts*, Elsevier, **2014**.

[18] C. P. Jijil, S. N. Bhange, S. Kurungot, R. N. Devi, *ACS Appl Mater Interfaces* **2015**, 7, 3041-3049.

[19] A. Grimaud, C. E. Carlton, M. Risch, W. T. Hong, K. J. May, Y. Shao-Horn, *J. Phys. Chem. C* **2013**, 117, 25926-25932.

[20] P. W. Menezes, A. Indra, A. Bergmann, P. Chernev, C. Walter, H. Dau, P. Strasser, M. Driess, *J. Mater. Chem. A* **2016**, 4, 10014-10022.

[21] Y. Du, J.-o. Wang, L. Jiang, L. S. Borgna, Y. Wang, Y. Zheng, T. Hu, *J. Synchrotron Radiat.* **2014**, 21, 756-761.

[22] J. Y. C. Chen, J. T. Miller, J. B. Gerken, S. S. Stahl, *Energy & Environmental Science* **2014**, 7, 1382.

[23] V. Celorrio, L. Calvillo, E. Dann, G. Granozzi, A. Aguadero, D. Kramer, A. E. Russell, D. J. Fermín, *Catal. Sci. Technol.* **2016**, 6, 7231-7238.

[24] E. Vago, E. Calvo, *J. Electroanal. Chem.* **1992**, 339, 41-67.

[25] C. Wei, Z. Feng, G. G. Scherer, J. Barber, Y. Shao-Horn, Z. J. Xu, *Adv. Mater.* **2017**.

[26] F. Cheng, J. Shen, BoPeng, Y. Pan, Z. Tao, J. Chen, *Nat. Chem.* **2011**, 3, 79-84.

Chapter 7

Substituted Co spinel oxides towards oxygen evolution reaction: Revealing the role of metal-oxygen covalency and non-concerted proton-electron transfer in OER

Co-containing spinel oxides are promising oxygen evolution reaction (OER) electrocatalysts offering high activity and excellent stability. While substituting Co with other foreign metal elements presents as a feasible way to tune the OER properties, fundamental origin of the substitution effects on OER remains untouched. The new OER mechanism understanding has been most studied in oxygen-deficient perovskites, however, some of the spinel oxides tend to have cation deficiency. This chapter aims to deepen the understanding of OER on substituted spinel oxide by examining the OER of $ZnFe_xCo_{2-x}O_4$ *oxides* $(x=0\sim2.0)$*. It is revealed that the Co-O covalency dominates the distinctive OER of* $ZnFe_xCo_{2-x}O_4$ *and an enlarged Co-O covalency by 10 ~ 30 at% Fe substitution gives rise to the promotion in activity. Due to the cation-deficient nature of spinel oxides, the lattice oxygen-mediated OER is not considered as a favorable route for the best-performing* $ZnFe_{0.4}Co_{1.6}O_4$ *catalyst which exhibits pH-dependent OER activity.*

---

*This chapter published substantially as Y. Zhou, S. Sun, J. Song, S. Xi, B. Chen, Y. Du, A. Fisher, F. Cheng, X. Wang, H. Zhang, Z. J. Xu. *Adv. Mater*. 1802912 (2018).

7.1 Introduction

The dominating consumption of fossil fuels has created daunting environmental issues across the globe and there is a desperate need for clean energy resources to alleviate this crisis. Hydrogen is a fantastic clean energy resource because it is greenhouse gas-free and can be harnessed from water.[1] As one of the ways to generate hydrogen, water splitting is most challenged by the sluggish oxygen evolution reaction (OER) at the anode.[2-4] Some precious OER catalysts, e.g. IrO_2 and RuO_2, could offer decent catalytic efficiency but are not sustainable choices.[2] Transition metal oxides, with their tunable electronic structures by versatile strategies, have emerging as promising alternatives.[4-6] Co-containing spinel oxides have been intensively studied as OER electrocatalyst because they give efficient catalytic activity and high stability.[7-10] Substituting foreign transition metals elements for Co in spinel oxide is an effective approach in tuning the OER. Substituted cobaltites (e.g. $Zn_xCo_{3-x}O_4$,[11] $Ni_xCo_{3-x}O_4$[8]) have shown promoted OER activities relative to that of pure Co_3O_4. The activity enhancement has been attributed to markedly changed morphologies with large roughness factor and high active site density.[8, 11] More fundamental understanding of the intrinsic origins remains limited.

As perovskite and spinel family all share octahedra TMO_6 unit, it is expected that the knowledge developed in perovskite towards electrocatalysis can bring insights into the understanding of OER by spinel oxide electrocatalysts. According to literature findings, the interaction between the transition metal B-site and oxygen remains the key in interpreting the OER of perovskite materials.[4, 6] More specifically, the e_g electron of B-site cation, the B-site metal-oxygen covalency have been identified as the catalytical-critical parameter in understanding the OER performance or reaction mechanisms.[4] The groundbreaking vision that lattice oxygen could also act as active centers in oxygen-deficient perovskite oxides has been supported as researchers recently found incontrovertible evidence of lattice oxygen oxidation during OER by in-situ mass spectrometry.[12] The increased covalency of TM-O bond has been considered critical in triggering the lattice oxygen participation.[12-13] However, most existing mechanism studies touching the lattice oxygen involvement have been focus on oxygen deficient perovskite oxides, e.g. BSCF82, $Pr_{0.5}Ba_{0.5}CoO_{3-\delta}$, $La_{1-x}Sr_xCoO_{3-\delta}$, and etc.[12-14] It is worth noting that most of the spinel oxides tend to have cation deficiencies (an oxygen-excess nonstoichiometry) and exhibit p-type conductivity.[6, 15] This could actually make a difference to the mechanistic understanding of OER by spinel materials.

In this chapter, a series of Fe substituted Co spinel oxides ($ZnFe_xCo_{2-x}O_4$ oxides (x=0~2.0)) were investigated as OER catalysts. As octahedral Co play a dominating role towards OER, exclusive attention was given to the octahedra TMO_6 unit by introducing Zn to block the tetrahedral sites. The experimental results show that the Fe substitute (with appropriate substitution level) acts as a promoter for the OER performance of octahedra [CoO_6] in the investigated spinel oxides. The altering of the Co electronic state induced by the substitutes was explicitly examined by XAS and DFT calculation. It is revealed that the covalency of Co-O bond, indicating by the parameter N-V (N– the number of unpaired electrons of Co atom, V– bulk valence state of Co cation),[13] describes the distinctive OER activities afforded by the Fe-substituted Co spinel oxides. The best-performing $ZnFe_{0.4}Co_{1.6}O_4$ catalyst exhibits pH-dependent OER activity, indicating the existence of non-concerted proton-electron transfer during OER. However, unlike the oxygen-deficient perovskite oxides, the lattice oxygen-mediated OER is not considered as a favorable route for the best-performing $ZnFe_{0.4}Co_{1.6}O_4$ catalyst owing to its cation-deficient nature (give a wide energy gap between the O p-band and Fermi level).

7.2 Experimental details

Synthesis of $ZnFe_xCo_{2-x}O_4$ oxides (x=0~2.0). Metal acetates/nitrides ($Zn(CH_3COO)_2 \cdot 2H_2O$, $Fe(NO_3)_3 \cdot 9H_2O$ and $Co(CH_3COO)_2 \cdot 4H_2O$) with a specific molar ratio were first mixed in diluted nitric acid solution through vigorous stirring. Take the synthesis of $ZnFe_{1.4}Co_{0.6}O_4$ as an illustrative example. 2.5 mmol of $Zn(CH_3COO)_2 \cdot 2H_2O$, 1.5 mmol $Co(CH_3COO)_2 \cdot 4H_2O$ and 3.5 mmol $Fe(NO_3)_3 \cdot 9H_2O$ were mixed in diluted nitric acid solution (30 ml deionized water + 2 ml nitric acid) by vigorous stirring. Citric acid (15 mmol) acting as chelating agent, was then added in the mixture. Under constant stirring at 90℃ for several hours, the mixture solution converts into viscous gel. The gel was then decomposed in air at 170℃ (a heating rate of 10℃ min^{-1} to 170℃) for 12 hours to remove the remaining water and ground thoroughly. After applying a further heat treatment in air at 600℃ (a heating rate of 5℃ min^{-1} to 600℃) for 6 hours, phase pure spinel oxide particles were obtained.

Electrode preparation. Oxide electrode was fabricated by drop-casting catalysts onto a rotating disk electrode (RDE). Catalysts ink were prepared by ultra-sonicating the $ZnFe_xCo_{2-x}O_4$ powders, acid-treated acetylene black (AB), Nafion® perfluorinated resin solution (5 wt% in water) in mixture solution containing water and isopropanol (volume ratio of Nafion® perfluorinated resin solution /water/isopropanol=0.05/4/1). The ink concentrations are 5 mg $m^{-1}{}_{ox}$ and 1mg $ml^{-1}{}_{AB}$. 10 μl of the ink was dropped on the RDE, yielding a final mass loading of 255 μg_{ox} $cm^{-2}{}_{disk}$ and 51μg_{AB} $cm^{-2}{}_{disk}$. As control experiments, the electrode preparation for commercial IrO_2 follows the same procedure described above. The IrO_2 (99.9% trace metals basis, Sigma-Aldrich) powder was mixed with acetylene black (AB) with a weight ratio of 5:1 and dispersed in a mixture solution containing water, ethanol, and Nafion perfluorinated resin solution. The final mass loading of IrO_2 on the rotating disk electrode is 255 μg_{ox} $cm^{-2}{}_{disk}$. The pure carbon (AB) electrode was prepared by dispersing the AB powder in a solvent mixture containing water, ethanol and Nafion perfluorinated resin solution ($V_{water}/V_{ethonal}/V_{Nafion}$ = 4:1:0.125). The ink concentration produced was 1 mg_{AB} ml^{-1}. 10 μl of the ink was dropped on the rotating disk electrode (RDE) to yield a final mass loading of 51 μg_{AB} $cm^{-2}{}_{disk}$.

Electrochemical measurements. The OER activity of the prepared catalysts was tested in O_2-saturated KOH solution using a three-electrode cell. The working electrode is catalyst decorated glassy carbon electrode. A Pt spiral wire and saturated calomel electrode (SCE) were used as the counter and reference electrode, respectively. The electrochemical experiments were performed using a WaveDriver Potentiostat and RDE bundle controlled by aftermath software package. A rotating speed of 1600 rpm was applied during the OER test and at least three independent measurements were performed for each catalyst. The KOH electrolyte concentration of 0.1 M was used to investigate the activity differences of the various $ZnFe_xCo_{2-x}O_4$ oxide catalysts and the cycling stability. Different KOH concentrations (0.03 M, 0.1 M, 0.5 M and 1.0 M) were used to examine the pH dependence of the investigated spinel catalyst towards OER. The electrolyte (KOH) resistance was measured right after each OER measurement.

7.3 Results and discussion

Figure 7.1 a shows the structure of spinel oxides. The transition metal elements either occupy the four oxygen-coordinated tetrahedral site or the six oxygen-coordinated octahedral site. The synthesis of $ZnFe_xCo_{2-x}O_4$ oxide aims to give a normal spinel structure, where the catalytically inactive Zn occupies all the tetrahedral sites.

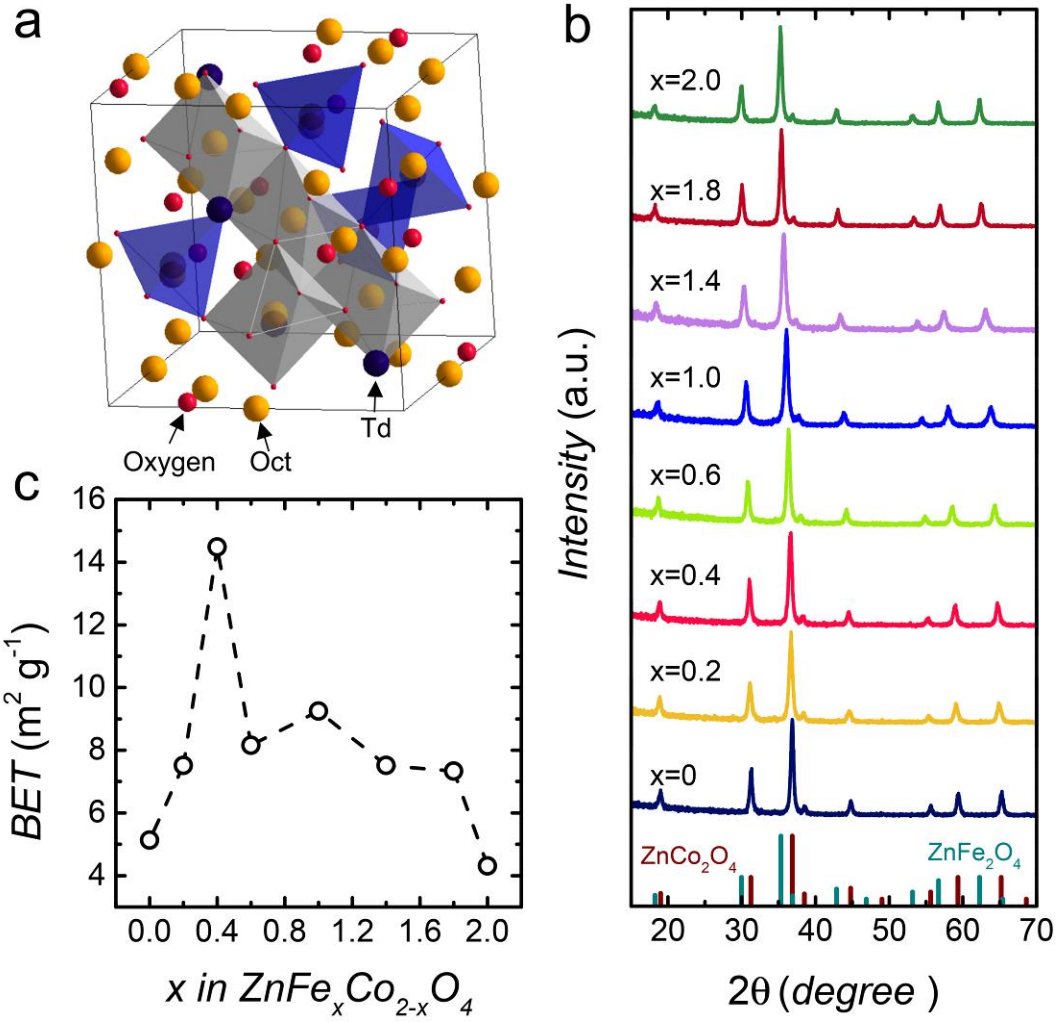

Figure 7.1 (a) Spinel crystal structure. (b) XRD patterns of $ZnFe_xCo_{2-x}O_4$ (x=0~2.0) oxides. (c) BET surface area of $ZnFe_xCo_{2-x}O_4$ (x=0~2.0) oxides.

The crystal structure of the as-prepared $ZnFe_xCo_{2-x}O_4$ oxides was confirmed by XRD. As shown in Figure 7.1 b, the diffraction peaks of $ZnFe_xCo_{2-x}O_4$ (x=0~2) agree well with the standard spinel patterns, indicating the phase purity of synthesized oxides. The BET surface area of $ZnFe_xCo_{2-x}O_4$ oxides is also determined and the results are shown in Figure 7.1 c.

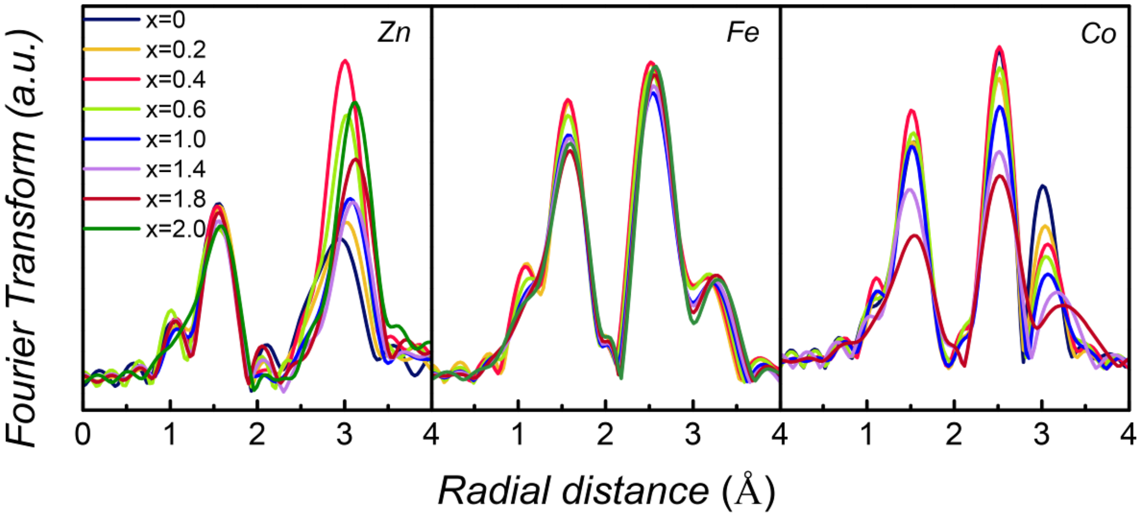

Figure 7.2 EXAFS k^3 $\chi(R)$ spectra at Zn, Fe and Co K-edge for $ZnFe_xCo_{2-x}O_4$ oxides.

X-ray absorption fine structure (XAFS) technique was performed to probe the structure and cation valence states information of $ZnFe_xCo_{2-x}O_4$ spinel oxides. The normal spinel structure of $ZnFe_xCo_{2-x}O_4$ oxides is confirmed by the EXAFS data. As displayed in Figure 7.2, the Zn K-edge EXAFS spectra show only one metal-metal distance at ~3.0 Å. In remarkable contrast, the Fe and Co K-edge show two metal-metal distances at ~ 2.5 Å and ~3.0 Å. According to literature findings, the metal ion of interest, if located at octahedral site, possess two metal-metal distances ($Atom_{[Oh]}$-$Atom_{[Oh]}$ at ~2.5 Å, and $Atom_{[Oh]}$-$Atom_{[Td]}$ at ~3.0 Å) in the FT EXAFS spectra.[16] In contrast, only one metal-metal distance ($Atom_{[Td]}$-$Atom_{[Oh]}$ at ~3.0 Å) exists for the absorbing metal ions located at tetrahedral site. Therefore, the exclusive occupation of Zn in tetrahedral site is confirmed and the edge-sharing octahedral $[Fe_xCo_{1-x}O_6]$ units should be the major catalytic contributor.

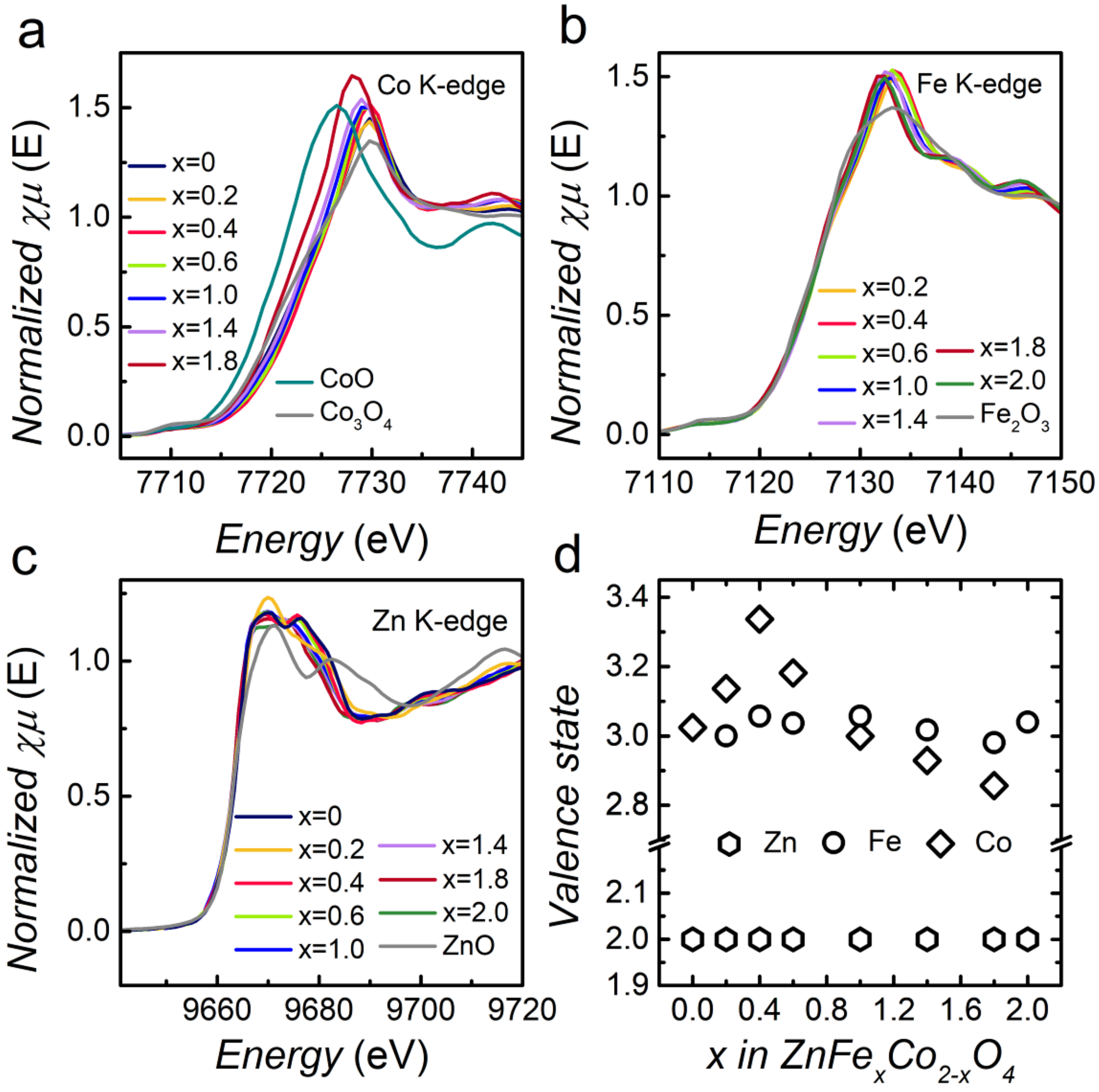

Figure 7.3 XANES spectra of $ZnFe_xCo_{2-x}O_4$ at (a) Co, (b) Fe and (c) Zn K-edge. (d) Determined Co, Fe and Zn valence states as a function of composition x in $ZnFe_xCo_{2-x}O_4$ oxides.

As shown in Figure 7.3 a and 7.3 b, the absorption edges of Co exhibit significance shifts along with Co/Fe ratio change while the edge energies of Fe almost remain unchanged. The edge positions of all the Zn K-edge spectra (Figure 7.3 c) overlaps with that of the reference ZnO. The quantified valence states (Figure 7.3 d) by an integral method[17] show that Co valence state ranges from ~+2.85 to +3.35 and Fe and Zn valence state remains at around +3 and +2, respectively. The approximated chemical formula $ZnFe_xCo_{2-x}O_{4+\delta}$ (δ ranges from 0 to 0.27) indicates the existence of oxygen non-stoichiometry.

Table 7.1 The defect formation enthalpies ΔH_f under oxygen rich chemical potentials (μ_0 = 0 eV). As a result of oxygen rich condition (μ_0 = 0 eV), μ_{Zn} = -3.754 eV.

	Calculated energy (eV)	$\boldsymbol{\Delta H_f}$ (eV)
Zn_V ($ZnCo_2O_4$)	-301.753	1.515
O_i ($ZnCo_2O_4$)	-308.219	3.973
Zn_V (Fe-$ZnCo_2O_4$)	-304.100	1.376
O_i (Fe-$ZnCo_2O_4$)	-310.641	3.758

As the various spinel oxides are non-stoichiometric, the formation of defects in the spinel lattice was first examined. Crystal models of $ZnCo_2O_4$ (Figure 7.4 a) and Fe-$ZnCo_2O_4$ were built. The Fe-$ZnCo_2O_4$ represent Fe-substituted $ZnCo_2O_4$. The Fe-$ZnCo_2O_4$ is built by replacing one of the 16 octahedral Co atoms with Fe and the chemical formula of Fe-$ZnCo_2O_4$ crystal model can be approximately as $ZnFe_{0.125}Co_{1.875}O_4$. To maintain charge neutrality, either positive cation vacancies are created or excess oxygen is inserted into the spinel lattice. Using density functional theory (DFT), we examined the formation energy of point defects (oxygen interstitial: O_i, Zn vacancy: Zn_V) in the spinel lattice. The modeling of point defects follows the methodology by Wei[18] and the formation enthalpy was calculated from the following equation:[18]

$$\Delta H_f = E_{defect} - E_{bulk} + nE_i + n_i\mu_i$$

where E_{defect} and E_{bulk} are the total energy of the defective cell and bulk host lattice, respectively. E_i represents the elemental energies calculated from the constituent elements in their standard states using an equivalent basis set. μ_i represent the chemical potentials of each constituent species which depends on specific equilibrium growth conditions.

The calculated defect formation enthalpies are summarized in Table 7.1. The formation energy of Zn_V in $ZnCo_2O_4$ (1.515 eV) and Fe-$ZnCo_2O_4$ (1.376 eV) is much less than the formation energy of O_i (~3.8 eV). This means, thermodynamically, the formation of oxygen interstitial is quite unlikely in the spinel lattice. In contrast, it is the formation of Zn vacancy that compensate for oxygen-excess nonstoichiometry. It is also note that the formation enthalpies of Zn vacancy in Fe-$ZnCo_2O_4$ (1.376 eV) is relatively lower than the vacancy formation energy in $ZnCo_2O_4$ (1.515 eV), demonstrating that the Fe substitution has promoted defects formation in the spinel lattice. The existence of Zn vacancies was also experimentally confirmed in the most non-stoichiometric compositions (x=0.4 and x=0.6). As shown in Table 7.2, the atomic ratios of Zn/(Fe+Co) are 0.950 : 2 and 0.886 : 2 in $ZnFe_{0.4}Co_{1.6}O_4$ and $ZnFe_{0.6}Co_{1.4}O_4$, respectively.

Table 7.2 ICP-OES (Inductively coupled plasma-optical emission spectrometry) analysis results of spinel $ZnFe_{0.4}Co_{1.6}O_4$ and $ZnFe_{0.6}Co_{1.4}O_4$.

	Weight (g)	Solution volume (mL)	Elements	Element concentration (mg/L, ppm)	Atomic ratio of Zn: (Fe+Co)	Atomic ratio of Fe: Co
$ZnFe_{0.4}Co_{1.6}O_4$	0.0148	25	Co	24.31	0.950 : 2	1 : 4.258
			Zn	15.80		
			Fe	5.41		
$ZnFe_{0.6}Co_{1.4}O_4$	0.0035	25	Co	5.43	0.886 : 2	1 : 2.404
			Zn	3.78		
			Fe	2.14		

With the modeling of Zn vacancies, Bader charge analysis[19-21] was further conducted to examine the changes in Co electronic structure with Fe substitution in the spinel lattice. As illustrated in Figure 7.4, two crystal models ($ZnCo_2O_4$ and V_{Zn}-Fe-$ZnCo_2O_4$) were built for the Bader charge analysis. Specifically, Zn vacancies were introduced into the Fe-substituted spinel oxide, but not into the $ZnCo_2O_4$. This aims to achieve theoretical and experimental consistency because the XANES results show that the substituted spinel oxide (with trace amount of Fe, x ranges from 0.2~0.6) is far from stoichiometric than that of $ZnCo_2O_4$ and the defect formation calculation also support the above clarification. The substituted crystal model (V_{Zn}-Fe-$ZnCo_2O_4$) is built by replacing one of the 16 octahedral Co atoms with Fe.

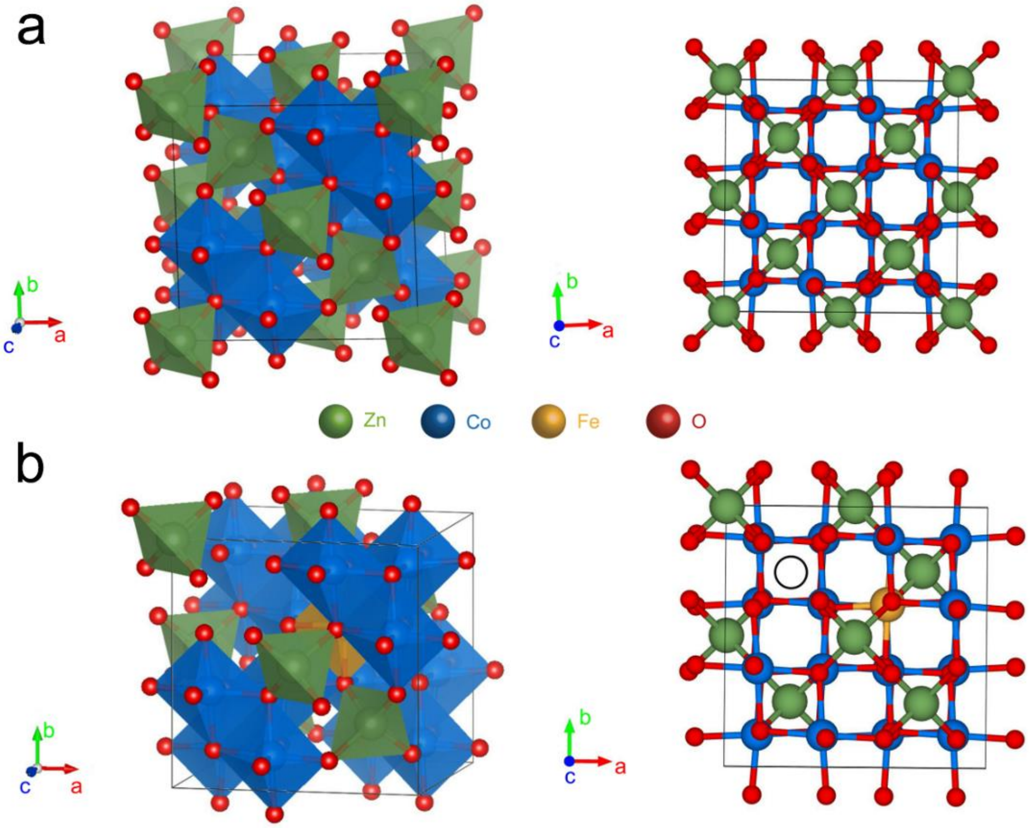

Figure 7.4 Crystal models of (a) $ZnCo_2O_4$ and (b) V_{Zn}-Fe-$ZnCo_2O_4$ built for DFT calculations.

The Bader charge results are shown in Table 7.3. As can be seen, the average charge of Co atoms in $ZnCo_2O_4$ model is 7.6532. In contrast, the average charge of Co drops to 7.6517 in V_{Zn}-Fe-$ZnCo_2O_4$. The Bader charge and magnetic moment of Fe are 6.27 and 3.97 μB, respectively, indicating the very presence of Fe^{3+} and the difficulty of Fe^{3+} to be oxidized in V_{Zn}-Fe-$ZnCo_2O_4$ system.[18, 22] It is proposed that the electron-deficient Zn vacancies could withdraw electron density away from Co, resulting in the drop of Co average charge (i.e. the increase of Co valence state). Therefore, the observed Co oxidation states higher than +3 by trace amount of Fe substitution (Figure 7.3 d) is understandable. From the DFT analysis, the altering of Co electronic state due to the presence of Fe substitutes (trace amount) has been illuminated and a level of consistency has been achieved comparing the XANES and computational results.

Table 7.3 Computing results of the Bader charge analysis.

$ZnCo_2O_4$			V_{Zn}-Fe-$ZnCo_2O_4$		
Atom	Charge	Magnetic moment	Atom	Charge	Magnetic moment
Zn1	10.7512	0.000	Zn1	10.7111	-0.002
Zn2	10.7511	0.000	Zn2	10.7144	-0.001
Zn3	10.7512	0.000	Zn3	10.7013	0.002
Zn4	10.7511	0.000	Zn4	10.7013	0.002
Zn5	10.7513	0.000	Zn5	10.7127	0.002
Zn6	10.7512	0.000	Zn6	10.7349	0
Zn7	10.7513	0.000	Zn7	10.7127	0.002
Zn8	10.7512	0.000	Fe8	6.2709	3.966
Co9	7.6532	0.000	Co9	7.6578	-0.019
Co10	7.6532	0.000	Co10	7.6498	-0.001
Co11	7.6532	0.000	Co11	7.6487	-0.093
Co12	7.6532	0.000	Co12	7.6498	-0.001
Co13	7.6532	0.000	Co13	7.6578	-0.017
Co14	7.6532	0.000	Co14	7.6487	-0.095
Co15	7.6532	0.000	Co15	7.6586	0.006
Co16	7.6532	0.000	Co16	7.6504	-0.024
Co17	7.6532	0.000	Co17	7.6432	-0.086
Co18	7.6532	0.000	Co18	7.6432	-0.084
Co19	7.6532	0.000	Co19	7.6504	-0.032
Co20	7.6532	0.000	Co20	7.6531	-0.077
Co21	7.6532	0.000	Co21	7.65	-0.015
Co22	7.6532	0.000	Co22	7.6609	-0.038
Co23	7.6532	0.000	Co23	7.6531	-0.076
Co24	7.6532	0.000	O24	7.003	0.001
O25	6.9879	0.000	O25	6.9919	-0.002
O26	6.9833	0.000	O26	6.7538	-0.188
O27	6.9848	0.000	O27	6.9876	0.001
O28	6.9864	0.000	O28	6.9757	-0.015
O29	6.9879	0.000	O29	6.9827	-0.003

O30	6.9833	0.000	O30	6.9892	0
O31	6.9864	0.000	O31	6.9796	0
O32	6.9848	0.000	O32	6.9892	-0.002
O33	6.9879	0.000	O33	6.9757	-0.012
O34	6.9863	0.000	O34	6.9796	-0.002
O35	6.9848	0.000	O35	6.7538	-0.184
O36	6.9833	0.000	O36	6.9919	0.001
O37	6.9848	0.000	O37	6.9876	0.001
O38	6.9864	0.000	O38	6.8201	-0.038
O39	6.9879	0.000	O39	7.0349	0.067
O40	6.9833	0.000	O40	6.9814	0.001
O41	6.9848	0.000	O41	6.978	-0.012
O42	6.9879	0.000	O42	6.9971	0
O43	6.9833	0.000	O43	7.0232	0.051
O44	6.9863	0.000	O44	7.0232	0.05
O45	6.9879	0.000	O45	6.978	-0.016
O46	6.9864	0.000	O46	6.9814	0.001
O47	6.9833	0.000	O47	7.0349	0.066
O48	6.9848	0.000	O48	6.9895	0.002
O49	6.9879	0.000	O49	6.8171	-0.09
O50	6.9864	0.000	O50	6.9868	-0.005
O51	6.9833	0.000	O51	7.0012	-0.001
O52	6.9848	0.000	O52	7.0087	0.02
O53	6.9848	0.000	O53	6.9922	-0.001
O54	6.9864	0.000	O54	6.9895	0.002
O55	6.9879	0.000	O55	6.9868	-0.002
O56	6.9833	0.000			

The OER of the various $ZnFe_xCo_{2-x}O_4$ were examined in alkaline solution. Figure 7.5 a displays the representative OER cyclic voltammetry curves and the capacitance and iR-corrected linear sweep voltammetry (LSV) curves of the investigated spinel oxides recorded within a potential window of 1.0~1.8V (vs. RHE) in O_2-saturated 0.1M KOH. Since the electrocatalytic OER is a surface-engaged process, the OER kinetic currents are presented as currents normalized by the BET surface area of the spinel oxides to allow a fair comparison of catalysts' intrinsic activity. As displayed in Figure 7.5 b, the iR-corrected potentials are plotted as a function of oxide surface area-normalized kinetic currents. As can be observed, the OER activities of various $ZnFe_xCo_{2-x}O_4$ (x=0~2) span across a potential window of ~130 mV. Considering the $ZnCo_2O_4$ as benchmark, substituting Fe for Co either produces a positive or negative effect on the OER performance, depending greatly on the substitution level. The potentials needed to afford a current density of 25 µA cm^{-2}_{ox} are further plotted as a function of Fe content (x) in Figure 7.5 c. The OER activity is promoted by replacing Co with a relatively small amount of Fe (x=0.2~0.8), as indicated by the reduced overpotentials (of ~35 mV in maximum) compared with $ZnCo_2O_4$. On the contrary, activity deteriorations are detected when the Fe substitution reaches a threshold of x=1.0 from which the OER performance drops dramatically at progressively higher Fe substitution (x=1.0) up to a full replacement of Co. The best-performing catalyst appears to be the $ZnFe_{0.4}Co_{1.6}O_4$ oxide. To evaluate its activity, the commercial IrO_2 was tested for OER following a consistent procedure described for the various spinel catalysts. The LSV curve of IrO_2 and $ZnFe_{0.4}Co_{1.6}O_4$ are displayed in Figure 7.5 d for comparison purpose. The $ZnFe_{0.4}Co_{1.6}O_4$ catalyst requires lower overpotential than IrO_2 to drive a geometric current density of 10 mA cm^{-2}_{disk}, demonstrating the capability of spinel $ZnFe_{0.4}Co_{1.6}O_4$ catalyst in replacing commercial IrO_2. To allow a fair comparison, the specific activity is also compared in the following section.

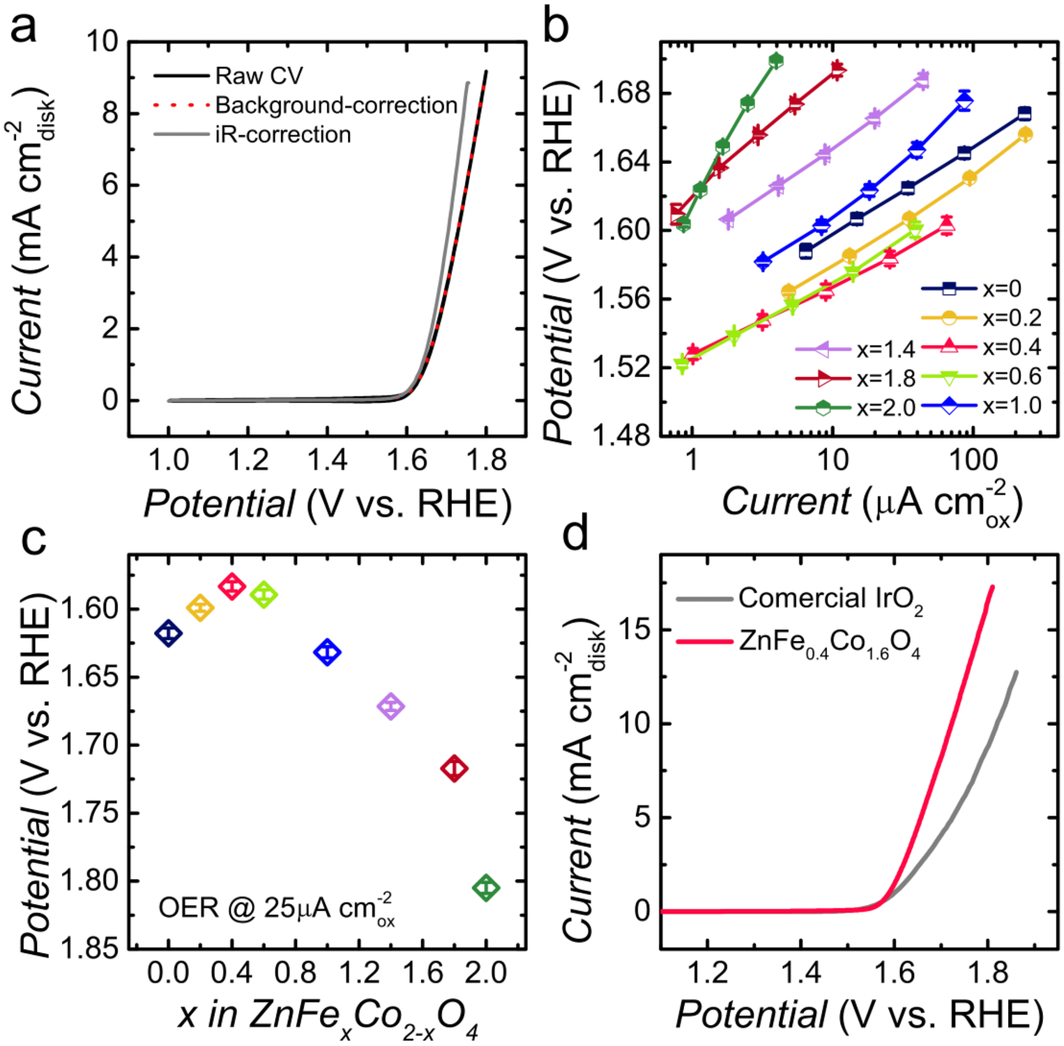

Figure 7.5 (a) The background correction and iR correction of OER CV curves on $ZnCo_2O_4$ in O_2-saturated 0.1 M KOH (scan rate: 10 mV s^{-1}). (b) OER specific activities obtained after background and iR correction. (c) Potentials required to drive a current density of 25 μA cm^{-2}_{ox} as a function of Fe content. (d) OER polarization curves of $ZnFe_{0.4}Co_{1.6}O_4$ and commercial IrO_2 in O_2-saturated 0.1 M KOH. Error bars represent at least three independent measurements.

A fundamental understanding of the distinctive OER brought by Co/Fe compositional change is a key component to the knowledge-guided design of efficient OER electrocatalyst. The morphology of the various $ZnFe_xCo_{2-x}O_4$ oxides were first examined by TEM. As shown in Figure 7.6, the oxides are made up of irregular-shaped particles without preferred orientations. The morphology is therefore not considered as an influencing factor altering the OER performance.

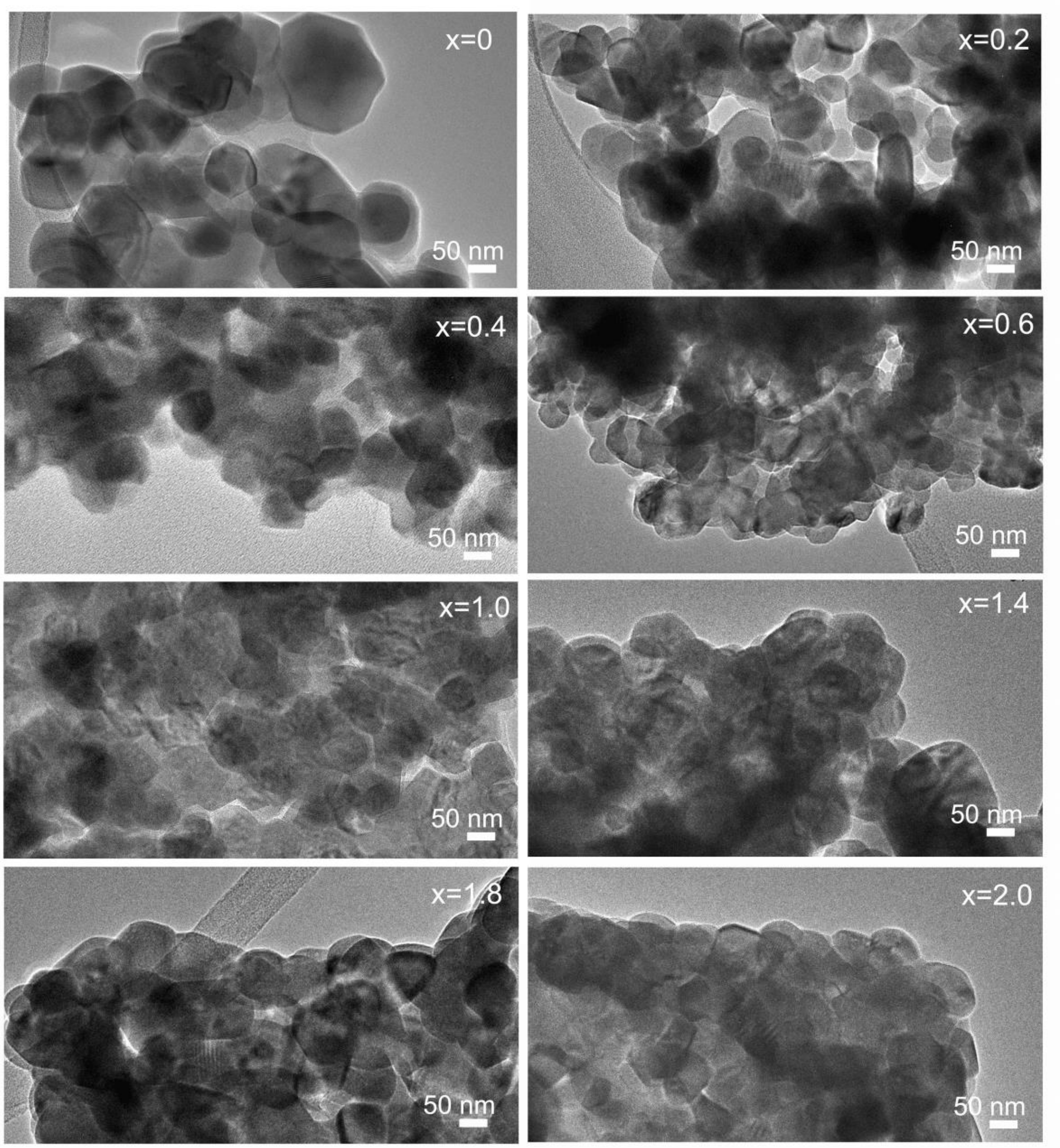

Figure 7.6 TEM images of the various $ZnFe_xCo_{2-x}O_4$ (x= 0~2) oxides.

Since the Fe in the various $ZnFe_xCo_{2-x}O_4$ are of a valence state of 3+, the Fe substitute is not considered as the major active site because the Fe^{3+} ($t_{2g}^3e_g^2$) binds the oxygen too weakly and fail to activate the reactant.[23-24] It is proposed that the Co plays a leading role in OER. The molecular orbital diagrams of Co^{3+}-OH and Co^{4+}-OH were plotted in Figure 7.7 a since the start-up step of OER in alkaline solution is the adsorption of OH*.[25] The OER specific activity of $ZnFe_xCo_{2-x}O_4$ oxides were then discussed as a function of *N*-*V*, which indicates the Co-O covalency.[13] To be specific, *N* denotes the number of unpaired electrons of Co atom ($4s^23d^7$), and *V* is the nominal valence state of Co. *N*-*V* is indicative of the net ability of Co to donate electrons, and specifically, the higher the *N*-*V* value, the greater the ability to donate electrons.[13] As displayed (Figure 7.7 b), the parameter *N*-*V* well describes the OER activity trend of the various substituted Co spinel oxides. To be specific, a decreased *N*-*V* gives a higher OER activity and vice versa. This linear correlation can be explained by the role of Co-O covalency (the covalent character of Co-O bond). The parameter *N*-*V* which indicates the capability of transition metal to donate electrons actually reflects the covalency of the TM-O bond.[13] In a pure ionic picture, the oxygen can get the electrons very easily from the metal and forming an ionic TM-O bond. The covalency describes the covalent character of such TM-O bond. For example, if the transition metal is less capable of donating electrons to the oxygen in a TM-O bond, the electronic density might slightly shift away from the oxygen atom and giving to a higher TM-O covalency. That means a low *N*-*V* value corresponds to a high TM-O covalency. An enlarged Co-O covalency facilitate fast electron transfer between the Co and oxygen adsorbates (e.g. O_2^{2-}, O^{2-}), and produces high OER efficiency.[26]

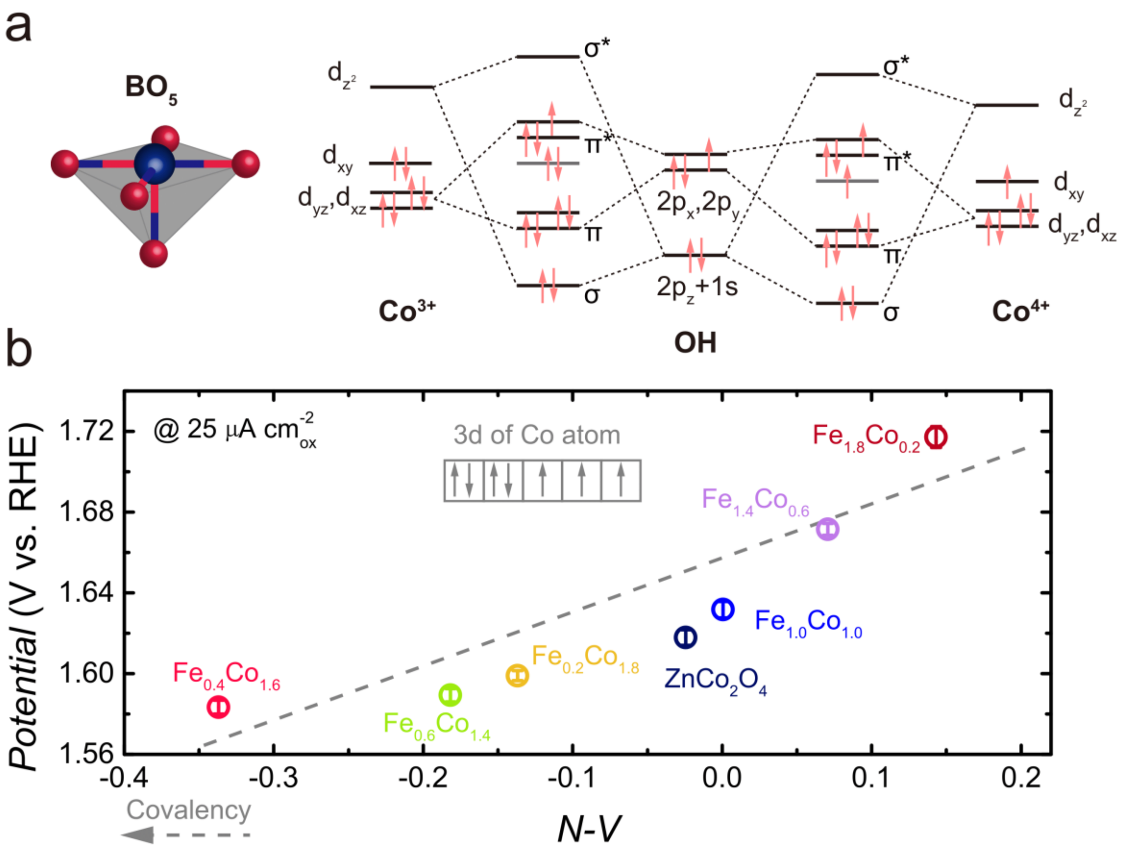

Figure 7.7 (a) The molecular orbital diagram of Co^{3+}-OH and Co^{4+}-OH at spinel surface. (b) OER specific activity versus N-V (an indicator of Co-O covalency).

To further confirm that the Co-O covalency is tuned by Fe substitution, electron density of states (DOS) for ZnCo$_2$O$_4$ and V$_{Zn}$-Fe-ZnCo$_2$O$_4$ were computed to give accurate determination. The partial density of state (pDOS) of Co 3d and O 2p for the two computation models are shown in Figure 7.8. The lowest conduction band and a valence band spreading over ~ 8 eV energy range are specifically displayed.

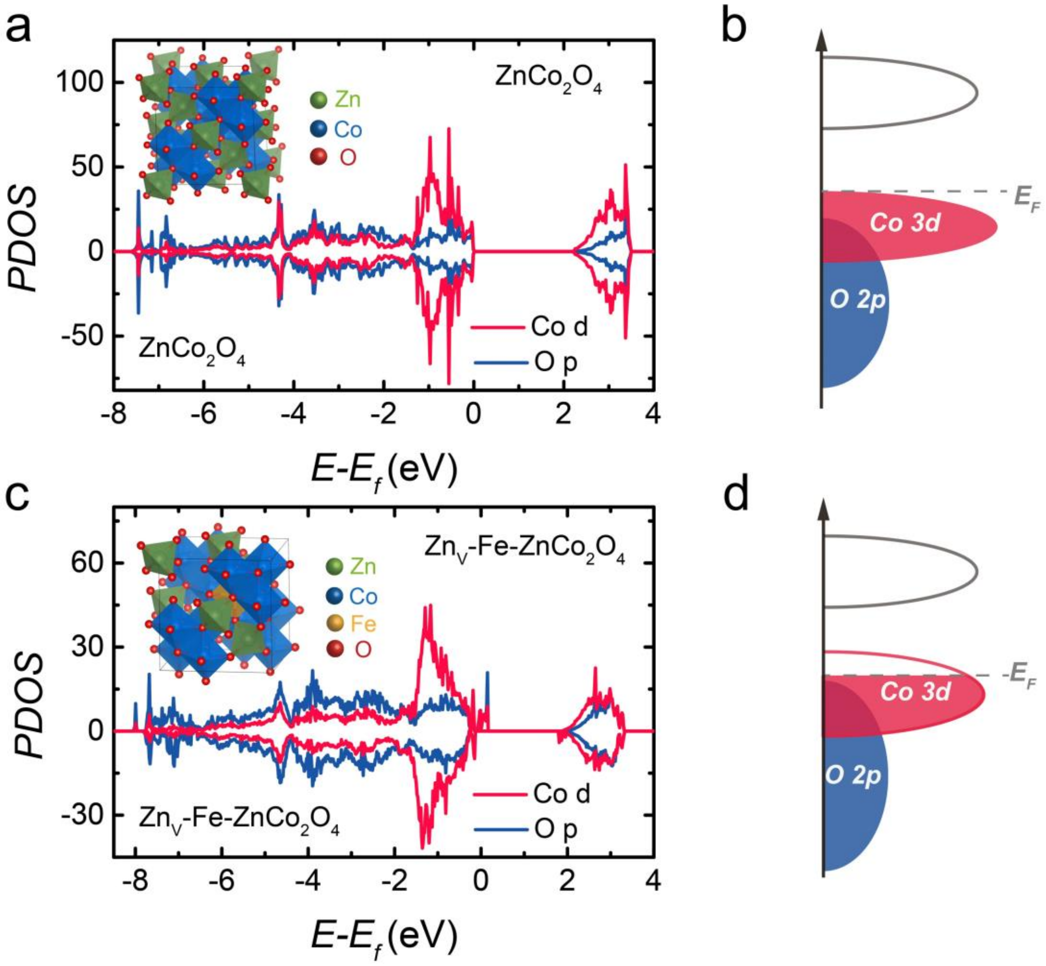

Figure 7.8 Computed partial electronic density of states (PDOS) and schematic representation of Co 3d-O 2p hybridization of (a, b) $ZnCo_2O_4$ and (c, d) Zn_V-Fe-$ZnCo_2O_4$. Inset of (a, c) are the corresponding crystal models built for the DFT calculation.

To evaluate the metal-oxygen covalency, the band center for Co 3d and O 2p states were determined and shown in Table 7.4. The band center distance (Co d to O p band) gives quantitative information about the Co-O covalency. The narrower the energy gap between Co d and O p, the larger the Co-O covalency.[26] As can be observed in Table 7.4, the energy gap of Co d center to O p center in Zn_V-Fe-$ZnCo_2O_4$ (0.75 eV) is smaller than the energy gap in $ZnCo_2O_4$ (0.81 eV), demonstrating the enlarged Co-O covalency by trace amount of Fe substitution.

Table 7.4 The determined Co d, O p band center, Co-O band center distance and Fermi level energy from the DOS calculation.

	Co d center	O p center	Co d – O p	Fermi
$ZnCo_2O_4$	-0.5323	-1.34119	0.80889	4.3761
Zn_V -Fe -$ZnCo_2O_4$	-1.31539	-2.06641	0.75102	4.3332

According to recent findings, the metal-oxygen covalency also act as an indicator of the OER reaction mechanism (e.g. evolution of adsorbates evolution mechanism to lattice-oxygen participated mechanism with increasing metal-oxygen covalency) in perovskite oxide electrocatalyst.[13] The OER of the best-performing spinel $ZnFe_{0.4}Co_{1.6}O_4$ catalyst was examined in KOH solution with different pH ranging from 12.5 to 14. Independent OER measurements were conducted under different pH. As KOH electrolyte with different concentration/pH has different resistivity, the iR-corrected OER polarization curves are shown in Figure 7.9 b. Apparently, the OER activity of spinel $ZnFe_{0.4}Co_{1.6}O_4$ exhibits strong pH dependence and pH 14 produces the highest OER activity within the investigated pH range. One one hand, it substantiates the necessity of searching optimum catalyst at an optimum pH. As displayed in Figure 7.9 c, the overpotential and Tafel slope of $ZnFe_{0.4}Co_{1.6}O_4$ at pH 14 outperforms the various Co-based oxides, benchmark IrO_2 and RuO_2 reported in literatures.[6, 27-28] The spinel $ZnFe_{0.4}Co_{1.6}O_4$ appears to be one of the best candidates in replacing commercial IrO_2. On the other hand, the pH-dependence indicates the existence of non-concerted proton-electron OER in spinel $ZnFe_{0.4}Co_{1.6}O_4$.[29] The traditional understanding of OER assumes concerted proton-electron transfer during OER,[4, 6] as illustrated in Figure 7.10 a. For illustrative purpose, alternative non-concerted proton-electron transfers are shown in Figure 7.10 b.

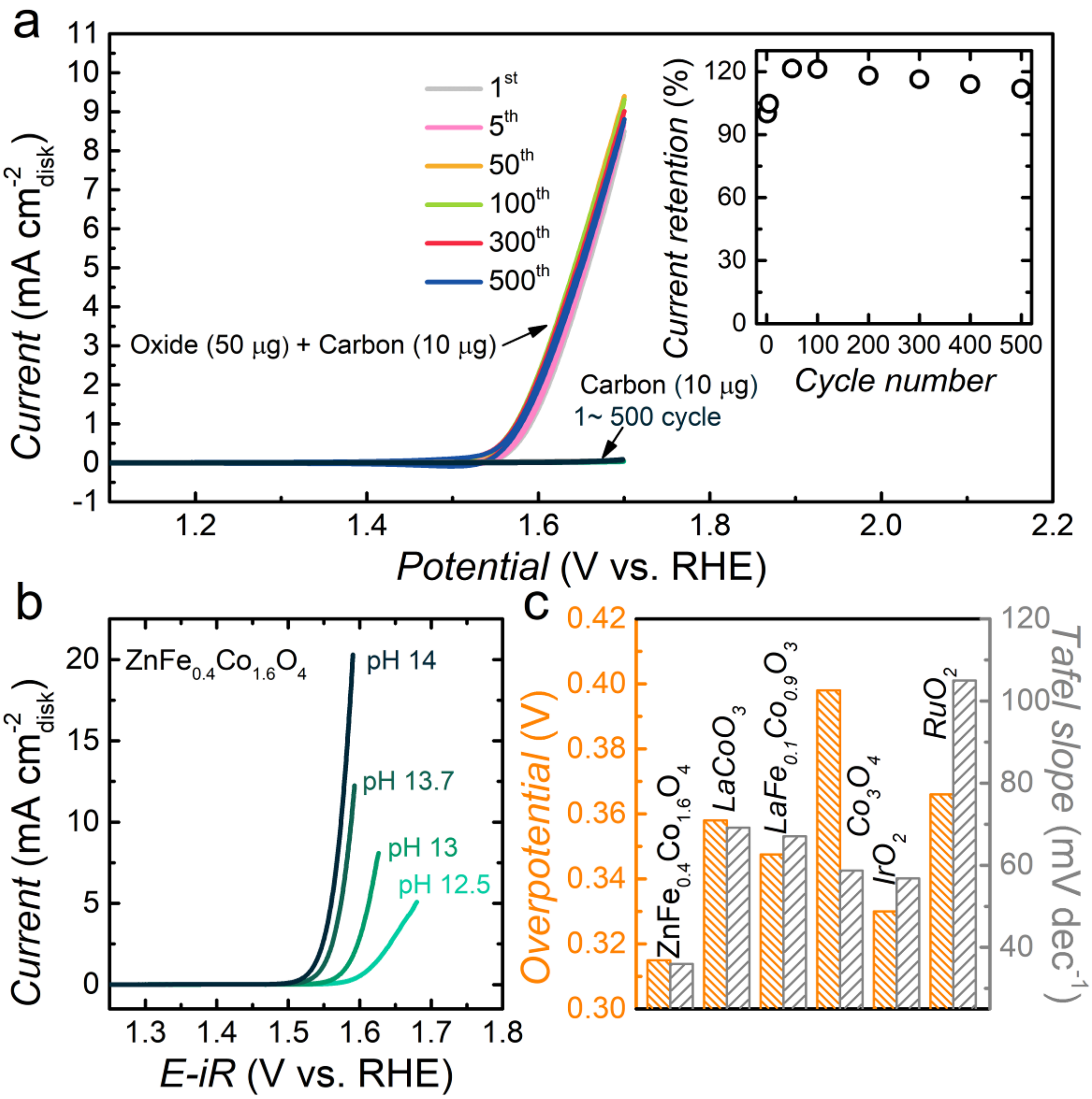

Figure 7.9 (a) OER CV curve of $ZnFe_{0.4}Co_{1.6}O_4$ catalyst and pure carbon over 500 cycles in 0.1 M KOH at a scan rate of 10 mV s^{-1}, inset is the current retention of $ZnFe_{0.4}Co_{1.6}O_4$ catalysts over 500 cycles. (b) The background and iR-corrected OER curves of $ZnFe_{0.4}Co_{1.6}O_4$ catalysts at different pH. (c) The overpotentials and Tafel slope of $ZnFe_{0.4}Co_{1.6}O_4$ catalyst, various Co-based oxides, benchmark IrO_2 and RuO_2, overpotential is defined as the overpotential required to achieve a specific current density of 50 μA cm$^{-2}_{ox}$.

In fact, the lattice oxygen participated OER presents as one of the possible decoupled proton-electron transfer in OER and the involvement of lattice oxygen has been recently substantiated in some oxygen-deficient perovskite OER electrocatalysts.[12, 30] The redox activity of lattice oxygen in oxygen electrochemical reactions has generated heated discussions.[31-32] It is thus inspiring to see whether the lattice oxygen is active or not in spinel oxides towards OER. Since the identified lattice oxygen-active OER catalyst generally shows drastic instability behavior over cycling,[12-14] the long-term stability of the $ZnFe_{0.4}Co_{1.6}O_4$ catalyst was first studied. To confirm that the carbon additive does not contribute to the OER activity, CV curves of pure carbon electrode over 500 cycles were provided in Figure 7.9 a. For the $ZnFe_{0.4}Co_{1.6}O_4$ catalyst, it displays excellent cycling stability which is different from the identified oxygen-active perovskite oxide catalysts.[5] The slight current increase over the first 50 cycles could be due to the leaching of the Zn (small amount).[33]

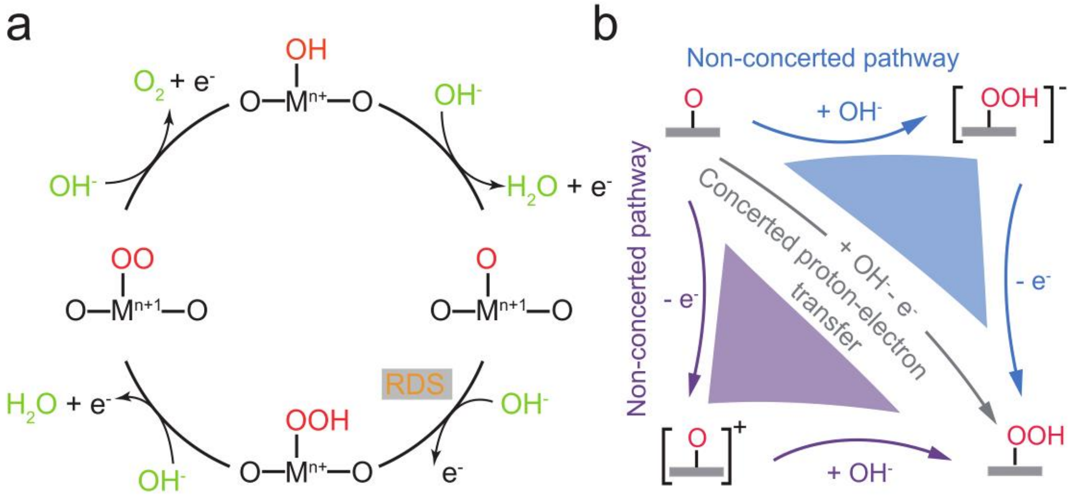

Figure 7.10 (a) Concerted proton-electron transfer OER mechanism on metal oxides. (b) Schematic illustration of concerted and non-concerted proton-electron transfer pathway of an exemplary OER rate-determining step (RDS), the alternative non-concerted proton-electron transfer pathways occurs along the edges of the square and traditional concerted proton-electron transfer occurs along the diagonal.

Note that the oxygen-active perovskite oxides also experience surface amorphization over cycling (especially for the first 50 cycles in 0.1 M KOH at a scan rate of 10 mV s^{-1}),[5, 14] TEM images of the $ZnFe_{0.4}Co_{1.6}O_4$ electrode before and after OER cycling were compared in Figure 7.11 b. It is interesting to find that the surface of the $ZnFe_{0.4}Co_{1.6}O_4$ catalyst does not undergo any significant amorphization during OER cycling. The index lattice planes in the FFT agrees well with the bulk spinel structure. The XRD patterns of the cycled

$ZnFe_{0.4}Co_{1.6}O_4$ catalyst shown in Figure 7.11 a also confirm the crystal structure remains unchanged after OER cycling.

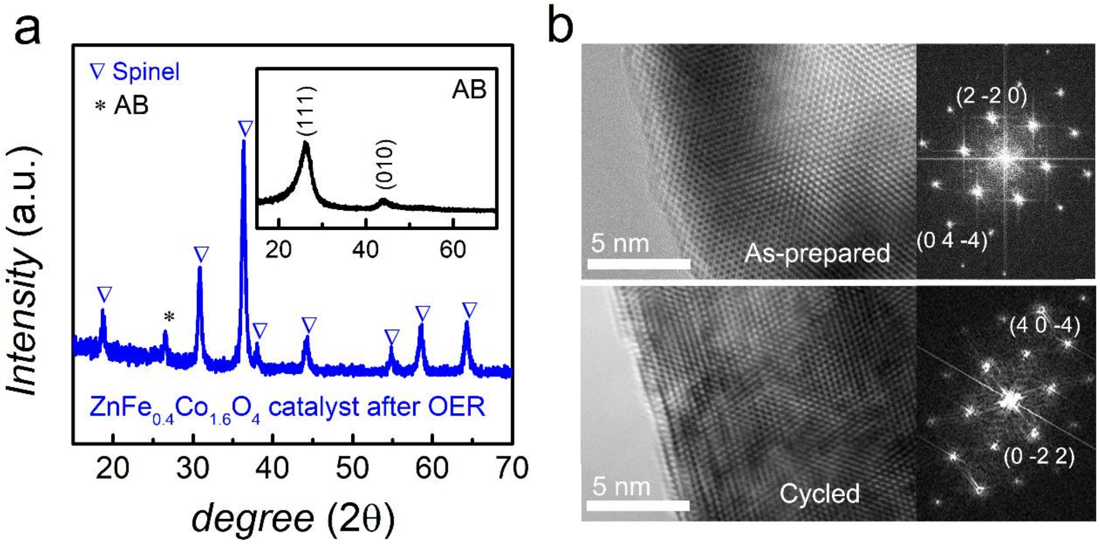

Figure 7.11 (a) XRD patterns of $ZnFe_{0.4}Co_{1.6}O_4$ catalyst after 50 OER cycles, inset is the pure carbon (acetylene black) XRD profile. (b) TEM and FFT images of as-prepared $ZnFe_{0.4}Co_{1.6}O_4$ catalyst and $ZnFe_{0.4}Co_{1.6}O_4$ catalyst after 50 OER cycles.

It is worth mentioning that the additional peak at around 27° is attributed to the signal from the carbon additive, because the spinel catalyst electrodes were prepared by mixing the spinel oxide with acetylene black (AB). It is confirmed that the spinel $ZnFe_{0.4}Co_{1.6}O_4$ catalyst does not show any distinctive features (i.e. instability and dramatic surface amorphization[5, 12, 14]) reported for the oxygen-active electrocatalysts. Thus, it is not likely that the lattice oxygen will be involved during OER in spinel $ZnFe_{0.4}Co_{1.6}O_4$ catalyst. The low probability of lattice oxygen involvement in spinel oxides can be rationalized by their cation-deficient nature. It is known that the lattice oxygen-mediated OER eventually leads to the formation of surface oxygen vacancies. The identified oxygen active perovskites (e.g. $La_{0.5}Sr_{0.5}CoO_{3-\delta}$, $Pr_{0.5}Ba_{0.5}CoO_{3-\delta}$, $SrCoO_{3-\delta}$) generally have an oxygen-deficient composition, and the formation energy of oxygen vacancy is low and a domination O 2p states near the Fermi level can be usually observed from the computed pDOS.[12-13] It might be due to the p-type conductivity of spinel oxides, the pDOS of spinel Zn_V-Fe-$ZnCo_2O_4$ (Figure 7.8) exhibits substantial metal 3d character, instead of O 2p, near the Fermi level. The investigated spinel oxide's O p-band center relative to the Fermi level is ~6.0 eV (Table 7.4), which is far more negative than the O p-band center observed in the identified oxygen-active perovskite catalysts (~ -2.0 eV).[12-13] Thus, the lattice oxygen might not be that active and the lattice oxygen participated OER might not be a favorable route in the cation-deficient spinel $ZnFe_{0.4}Co_{1.6}O_4$ catalyst.

7.4 Conclusion

To summarize, a series of spinel $ZnFe_xCo_{2-x}O_4$ (x=0.0~2.0) were examined for their OER performance in order to gain an understanding on the substitution effects on Co-containing spinel oxide catalysts. The experimental results show that the spinel oxides by 10 ~ 30 at% Fe substitution displayed enhanced OER activities relative to $ZnCo_2O_4$. The best-performing $ZnFe_{0.4}Co_{1.6}O_4$ oxide serve as a promising low-cost electrocatalyst as it outperforms the benchmark IrO_2 catalyst and exhibits good cycling stability. With changes in the electronic state of TM cations examined by XAS technique and DFT computation, the distinctive OER activity of Fe-substituted spinel oxides is found to be dominated by the Co-O covalency. An enlarged Co 3d and O 2p covalency is responsible for the activity enhancement as it facilitates the injection/extraction of electrons from oxygen. While the pH-dependent OER activity of $ZnFe_{0.4}Co_{1.6}O_4$ indicates decoupled proton-electron transfers during OER, the involvement of lattice oxygen is not considered as a favorable route because of the downshifted O p-band center relative to Fermi level governed by the spinel’s cation deficient nature. This work indicates that the metal-oxygen covalency could bridges the fundamental understanding of OER by oxide catalysts with different defect chemistry. The new perspective from the cation-deficient chemistry enriches the existing mechanistic studies on spinel oxides towards electrocatalysis.

References

[1] D. A. Kuznetsov, B. Han, Y. Yu, R. R. Rao, J. Hwang, Y. Román-Leshkov, Y. Shao-Horn, *Joule* **2017**, 2.

[2] L. C. Seitz, C. F. Dickens, K. Nishio, Y. Hikita, J. Montoya, A. Doyle, C. Kirk, A. Vojvodic, H. Y. Hwang, J. K. Norskov, *Science* **2016**, 353, 1011-1014.

[3] C. W. Cady, G. Gardner, Z. O. Maron, M. Retuerto, Y. B. Go, S. Segan, M. Greenblatt, G. C. Dismukes, *ACS Catal.* **2015**, 5, 3403-3410.

[4] J. Suntivich, K. J. May, H. A.Gasteiger, J. B. Goodenough, Y. Shao-Horn, *Science* **2011**, 334, 1383-1385.

[5] K. J. May, C. E. Carlton, K. A. Stoerzinger, M. Risch, J. Suntivich, Y.-L. Lee, A. Grimaud, Y. Shao-Horn, *J Phys. Chem. Lett.* **2012**, 3, 3264-3270.

[6] C. Wei, Z. Feng, G. G. Scherer, J. Barber, Y. Shao-Horn, Z. J. Xu, *Adv. Mater.* **2017**.

[7] C. Xiao, X. Lu, C. Zhao, *Chem. Commun.* **2014**, 50, 10122-10125.

[8] Y. Li, P. Hasin, Y. Wu, *Adv. Mater.* **2010**, 22, 1926-1929.

[9] C.-C. Lin, C. C. McCrory, *ACS Catal.* **2016**, 7, 443-451.

[10] P. Bothra, S. K. Pati, *ACS Energy Lett.* **2016**, 1, 858-862.

[11] X. Liu, Z. Chang, L. Luo, T. Xu, X. Lei, J. Liu, X. Sun, *Chem. Mater.* **2014**, 26, 1889-1895.

[12] A. Grimaud, O. Diaz-Morales, B. Han, W. T. Hong, Y.-L. Lee, L. Giordano, K. A. Stoerzinger, M. T. Koper, Y. Shao-Horn, *Nat. Chem.* **2017**, 9, 457-465.

[13] X. Rong, J. Parolin, A. M. Kolpak, *ACS Catal.* **2016**, 6, 1153-1158.

[14] C. Yang, A. Grimaud, *Catalysts* **2017**, 7, 149.

[15] M. N. Amini, H. Dixit, R. Saniz, D. Lamoen, B. Partoens, *Phys. Chem. Chem. Phys.* **2014**, 16, 2588-2596.

[16] H. Y. Wang, S. F. Hung, H. Y. Chen, T. S. Chan, H. M. Chen, B. Liu, *J. Am. Chem. Soc.* **2015**, 138, 36-39.

[17] H. Dau, P. Liebisch, M. Haumann, *Anal. Bioanal. Chem.* **2003**, 376, 562-583.

[18] A. Walsh, Y. Yan, M. Al-Jassim, S.-H. Wei, *J. Phys. Chem. C* **2008**, 112, 12044-12050.

[19] J. P. Perdew, K. Burke, M. Ernzerhof, *Phys. Rev. Lett.* **1996**, 77, 3865.

[20] G. Kresse, J. Hafner, *Phys. Rev. B* **1994**, 49, 14251.

[21] G. Kresse, J. Hafner, *Phys. Rev. B* **1993**, 47, 558.

[22] M.-H. Phan, T.-L. Phan, T.-N. Huynh, S.-C. Yu, J. R. Rhee, N. V. Khiem, N. X. Phuc, *J. Appl. Phys.* **2004**, 95, 7531-7533.

[23] S. Trasatti, *J Electroanal Chem Interfacial Electrochem* **1980**, 111, 125-131.

[24] S. Han, S. Liu, S. Yin, L. Chen, Z. He, *Electrochim. Acta* **2016**, 210, 942-949.

[25] J. O. M. Bockris, T. Otagawa, *J. Electrochem. Soc.* **1984**, 131, 290-302.

[26] W. T. Hong, K. A. Stoerzinger, Y.-L. Lee, L. Giordano, A. Grimaud, A. M. Johnson, J. Hwang, E. J. Crumlin, W. Yang, Y. Shao-Horn, *Energy Environ. Sci.* **2017**, 10, 2190-2200.

[27] Y. Lee, J. Suntivich, K. J. May, E. E. Perry, Y. Shao-Horn, *J. Phys. Chem. Lett.* **2012**, 3, 399-404.

[28] Y. Duan, S. Sun, S. Xi, X. Ren, Y. Zhou, G. Zhang, H. Yang, Y. Du, Z. J. Xu, *Chem. Mater.* **2017**, 29, 10534.

[29] M. T. M. Koper, *Chem. Sci.* **2013**, 4, 2710.

[30] J. T. Mefford, X. Rong, A. M. Abakumov, W. G. Hardin, S. Dai, A. M. Kolpak, K. P. Johnston, K. J. Stevenson, *Nat Commun* **2016**, 7, 11053.

[31] C. Yang, O. Fontaine, J.-M. Tarascon, A. Grimaud, *Angew. Chem.* **2017**.

[32] D. N. Mueller, M. L. Machala, H. Bluhm, W. C. Chueh, *Nat Commun* **2015**, 6, 6097.

[33] P. W. Menezes, A. Indra, A. Bergmann, P. Chernev, C. Walter, H. Dau, P. Strasser, M. Driess, *J. Mater. Chem. A* **2016**, 4, 10014-10022.

Chapter 8

Implications and Future Work

Chapter 8 draws together the threads of the thesis. A detailed description about how the hypotheses are fully validated by the experimental design is presented. New questions arise over the origin of the nanoparticles' surface Mn density difference are analyzed and recommended future work is presented. In addition, a systematic study on the correlation between the surface Mn density and the ORR performance of different crystal structured-manganese oxides is recommended.

8.1 Implications

Transition metal spinel oxides (Mn and Co-based) have been studied as oxygen electrocatalysts in this thesis. In particular, fundamental understandings have been developed which enables knowledge-guided design of efficient oxide electrocatalysts.

As spinel oxide contains two geometric sites, i.e. the tetrahedral site (Td) and octahedral site (Oct), it is intriguing to find out which geometric site is critical in oxygen electrocatalysis. The thesis first addresses the geometric role in spinel oxide towards electrocatalysis by designing structure flexible spinel $CoAl_2O_4$ oxide. Note that the distribution of transition metal elements in the two geometric sites strongly depends on the synthesis conditions, a series of spinel $CoAl_2O_4$ oxides were prepared by a sol-gel auto combustion method at different temperatures (400°C, 500°C, 600°C, 800°C). The parameter inversion degree (λ) defines the structure reversal in spinel oxide $(A_{\lambda}B_{1-\lambda})_{Td}[A_{1-\lambda}B_{1+\lambda}]_{Oct}O_4$. Through different temperature synthesis, the inversion degree of $CoAl_2O_4$ is readily tuned from 0.15 to 0.67. The produced $CoAl_2O_4$ structures can be approximated as $(Co_{0.33}Al_{0.67})_{Td}[Co_{0.67}Al_{1.33}]_{Oct}O_4$, $(Co_{0.42}Al_{0.58})_{Td}[Co_{0.58}Al_{1.42}]_{Oct}O_4$, $(Co_{0.81}Al_{0.19})_{Td}[Co_{0.19}Al_{1.81}]_{Oct}O_4$ and $(Co_{0.85}Al_{0.15})_{Td}[Co_{0.15}Al_{1.85}]_{Oct}O_4$ at 400°C, 500°C, 600°C and 800°C, respectively. As Co is the active sites (Al gives no catalytic contribution), the correlations made between the $CoAl_2O_4$ oxides' OER activity and the occupation of Co in the tetrahedral site or octahedral site help identify the catalytically critical geometry. It is found that the OER activity of $CoAl_2O_4$ oxides is positively related to the occupancy of Co in octahedral site. This demonstrate the hypothesis that the geometry plays an influencing role in electrocatalysis and in spinel structure, the octahedral geometry is the major contributor towards oxygen electrocatalysis.

In addition to the geometric factor, the composition-dependent ORR/OER is frequently observed in mixed-metal spinel oxides.[1-5] Changing the composition in spinel oxides has become a popular strategy in engineering the ORR/OER performance. The activity enhancement by compositional engineering has been attributed to markedly changed morphologies with large roughness factor and high active site density.[2, 5] More fundamental understanding of the intrinsic origins remains untouched. It is hypothesized that there exists dominating physical principles governing the composition-dependent ORR/OER. As oxide electrocatalysts that have been identified active for ORR are mainly Mn-based oxides,[6] a series of spinel $ZnCo_xMn_{2-x}O_4$ oxides were prepared and studied as ORR catalysts in order to reveal the underlying origin for the composition-dependent ORR. The synthesis of spinel oxides $ZnCo_xMn_{2-x}O_4$ (x ranging from 0 to 2) facilitate an exclusive examination of the catalytically critical edge-sharing [TMO_6] octahedra in electrocatalysis. To be specific, the introduction of Zn produced a normal spinel structure and hence the edge-sharing [$Co_xMn_{1-x}O_6$] octahedra becomes the major contributor to ORR. It is found the composition-dependent ORR of $ZnCo_xMn_{2-x}O_4$ (x=0~2) is strongly correlated to the e_g electron of active Mn that resulting from the superexchange interactions ($Mn_{[Oh]}$-O-$Co_{[Oh]}$) through the edge-sharing [$Co_xMn_{1-x}O_6$] octahedra. With Co gradually replaces Mn, the e_g state of Mn cations evolves from 0.3 to 0.9. The ORR of Mn-Co based spinel oxides exhibits a volcano shape as a function the e_g occupancy of Mn cations, indicating the influencing role of e_g electron in the composition-dependent ORR. This demonstrate the hypothesis that there exists a dominating parameter governing the composition-dependent ORR of substituted Mn spinel oxides.

The identified ORR descriptor in the $ZnCo_xMn_{2-x}O_4$ (x=0~2) systems, i.e. e_g occupancy, is apparently a bulk descriptor. A scaling relationship between the surface and bulk energetics has been built in perovskite oxides AMO_3 (A represents La or Sr, M represents metal from Sc to Ge) by researchers, consolidating the theory that the bulk thermochemistry act as a good descriptor for the electrocatalytic activity of transition metal oxides.[7] It is known that the perovskite oxides are generally of micro-scale size. In fact, the synthesized $ZnCo_xMn_{2-x}O_4$ (x=0~2) spinel particles by the sol-gel combustion method at 600°C are also of micro-scale size, which might explain why the bulk descriptor (e_g occupancy) is applicable. However, for ultra-small size nanoparticles, the surface might be totally different with respect to their bulk and the scaling relationship between the surface and the bulk might no longer exist. Thus, ultra-small size ferrite $Mn_xFe_{3-x}O_4$ oxides (x=0.5~2.5) particles (5~12 nm) were further prepared by a well-established facile chemical method and studied as ORR catalysts. The bulk chemistry of $Mn_xFe_{3-x}O_4$ particles was carefully revealed by bulk-sensitive tools: XRD, XANES, and EXAFS. In addition, the classical surface chemistry tool, XPS, was employed to probe the surface chemistry. Interestingly, the bulk chemistry fails to interpret the ORR of nano-size $Mn_xFe_{3-x}O_4$ oxide catalysts. It is found that the surface chemistry is indeed dominant the composition-dependent ORR of $Mn_xFe_{3-x}O_4$ oxides. The high surface/bulk ratio of nanoparticles gives a totally different surface composition. The near-surface Mn density revealed from an electrochemical approach strongly correlates to the distinctive ORR activity given by the various $Mn_xFe_{3-x}O_4$ oxide catalysts, demonstrating the hypothesis that the bulk descriptor is not applicable to ultra-small size nanoparticle systems.

Following the fundamental studies on composition-dependent ORR, a series of $ZnFe_xCo_{2-x}O_4$ (x=0~2) oxides were studied as OER catalysts to reveal the underlying origin for the composition dependent OER. The attention was shifted to Co-based spinel oxide mainly because the Co-containing oxides are among the most active OER oxide catalysts reported.[8-10] The introduction of Zn, on one hand, aims to produce normal spinel structures. This is in consideration of the dominating role of octahedral geometry in electrocatalysis. On the other hand, as the Zn spinels are generally categorized as p-type semiconductor, the introduction of Zn could help produce spinel oxides with cation deficiency.[11] The reason for the design of cation deficient spinel oxides is in the following considerations. The traditional OER mechanism understanding—centered on the redox chemistry of the metal cation— has been challenged recently. It is suggested that the anion-redox also plays an important part in oxygen electrocatalysis.[12-14] The groundbreaking vision that lattice oxygen act as active centers in oxygen-deficient perovskite oxides has been supported as researchers recently found incontrovertible evidence of lattice oxygen oxidation during OER by in-situ mass spectrometry.[14] The increased covalency of TM-O bond has been considered critical in triggering the lattice oxygen participation.[14-15] The lattice oxygen-mediated OER reaction pathways has been proposed by different research groups.[14, 16] However, most existing mechanism studies touching the lattice oxygen involvement have been focus on oxygen deficient perovskite oxides, e.g. BSCF82, $Pr_{0.5}Ba_{0.5}CoO_{3-\delta}$, $La_{1-x}Sr_xCoO_{3-\delta}$, and etc.[14, 16] It is worth noting that the oxygen vacancy concentration on the surface could be orders of magnitude higher than that in the bulk. Therefore, the surface defect chemistry might play an influencing role on catalytic reaction pathways. While for spinel oxide, it tends to form cation deficiencies (an oxygen-excess nonstoichiometry)[17] and exhibit p-type conductivity. This could actually make a difference to the mechanistic understanding of OER by spinel materials. Through investigating the $ZnFe_xCo_{2-x}O_4$

(x=0~2) oxides as OER catalysts, it is revealed that the Co-O covalency dominates the distinctive OER of $ZnFe_xCo_{2-x}O_4$ and an enlarged Co-O covalency by 10 ~ 30 at% Fe substitution gives rise to the activity promotion. The good cycling stability, reserved high-crystalline surface after cycling, and the computed downshifted O p-band relative the Fermi level validate the hypothesis that lattice oxygen-mediated OER is not a favorable route for the cation-deficient spinel oxides.

8.2 Recommended future work

In chapter 6, the manganese ferrite nanoparticles were examined as ORR electrocatalysts and the surface Mn density has been revealed as the catalytically critical parameter. Although the hypothesis that the bulk descriptor might not be applicable to the nanoparticle system has been validated through the experimental design in chapter 6, new questions arise over the underlying origin of the surface density difference.

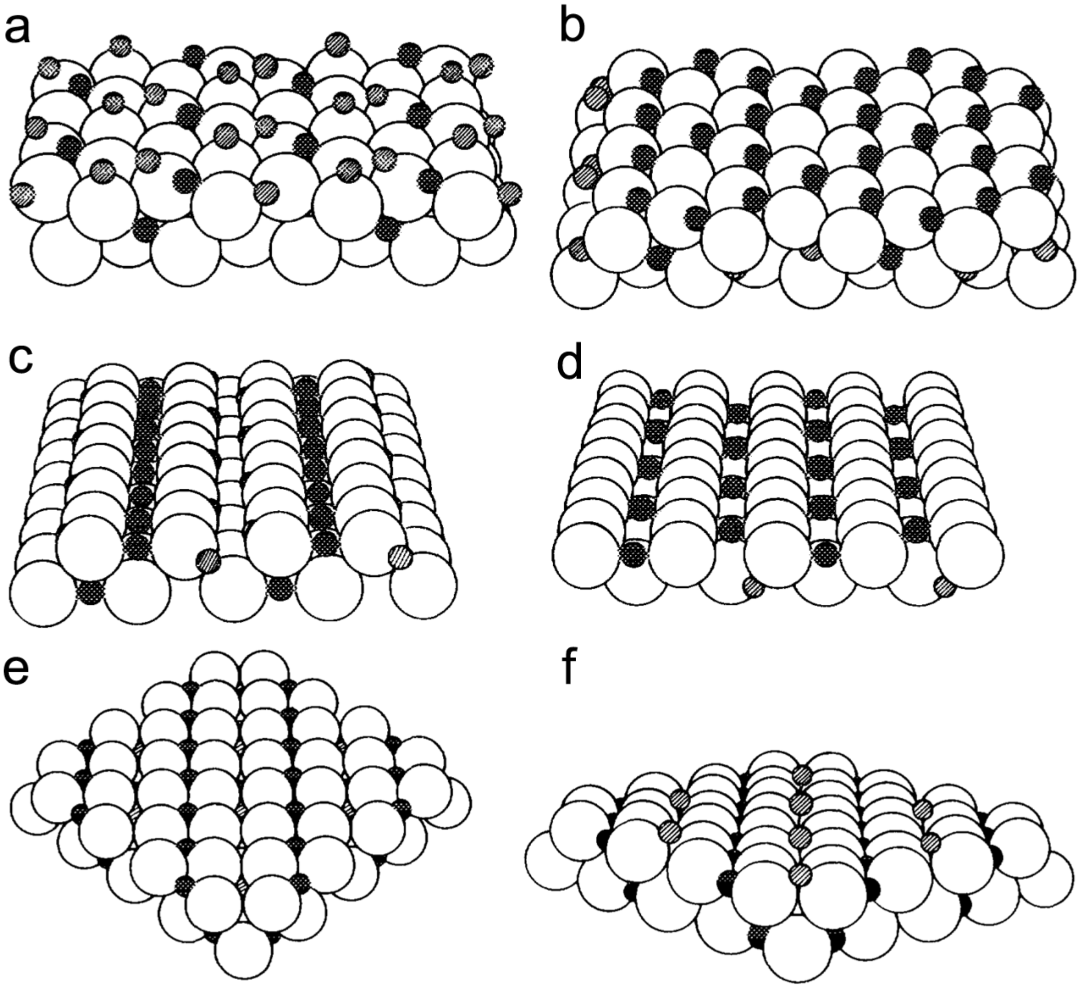

Figure 8.1 Illustration of low-index crystal planes (a) (111) A, (b) (111) B, (c) (110) C, (d) (110) D, (e) (100) E, and (f) (100) F of spinel oxides with a normal structure. The solid spheres represent the octahedral-coordinated cations, the crosshatched spheres represent the tetrahedral-coordinated cations and the open spheres are the oxygen anions.[18]

It is reported that for the normal spinel oxide, the octahedral-coordinated cations are rich in the oxide surface.[18] In contrast, the tetrahedral-coordinated cations are buried underneath the surface and are not electrochemically accessible to the reactants.[18] This is because the exposure of low-index crystal planes that rich in octahedral cations (as displayed in Figure 8.1) is more thermodynamically favorable. [18] Therefore, it is proposed that the Mn density in the spinel ferrites is related to the exposure of different crystal facet. Different crystal planes might have different metal ion density and different reactivity towards electrocatalysis. It is recommended that spinel oxide particles (e.g. $MnFe_2O_4$, $CoAl_2O_4$ and etc.) with preferentially exposed crystal surfaces be synthesized and the facet-dependent catalytic activity be examined. First, by adopting the integration method (integrate the redox responses of transition metal element), the metal ion density on a predominantly exposed crystal plane surfaces can be determined. The intrinsic reactivity of the preferentially exposed surfaces can be therefore revealed through examining the active metal site density-normalized catalytic activity. Such experimental design might help identify the catalytically active crystal planes and the preferred coordination environment of transition metal.

As it is confirmed in chapter 6 that the surface Mn density plays an influencing role in spinel manganese ferrite oxides towards ORR, it is also intriguing to extend the attention to other Mn-based oxide materials. Of notable interest is the manganese oxide, which can form many different crystal structures.[19]

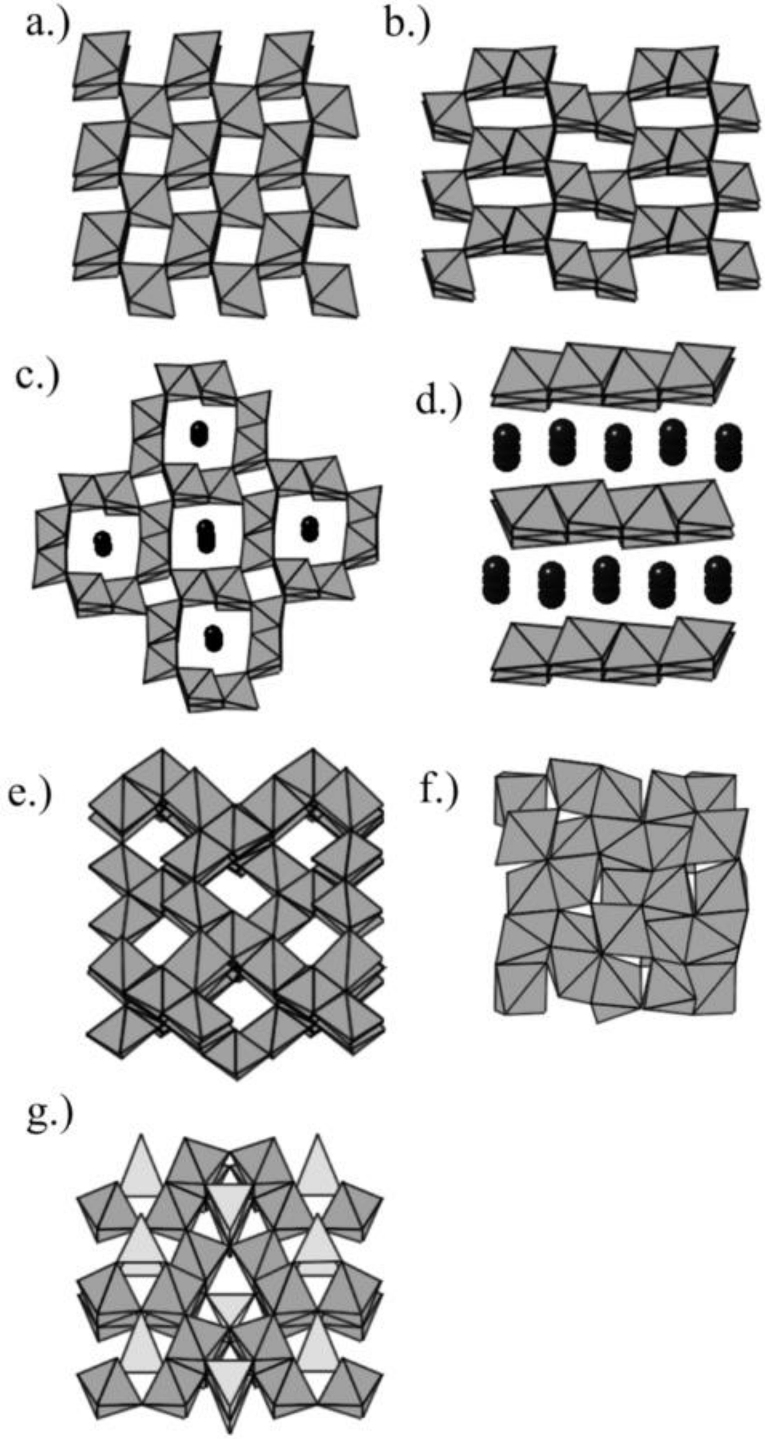

Figure 8.2 Representation of the eight type manganese oxides. (a) β-MnO_2, (b) R-MnO_2, (c) α-MnO_2, (d) δ-MnO_2, (e) λ-MnO_2, (f) Mn_2O_3, and (g) Mn_3O_4.[19]

Figure 8.2 illustrate some of the crystal structures manganese oxide can form. To be specific, the different arrangements of MnO_6 octahedra or MnO_4 tetrahedra units produce distinct crystal structures. Although structure-related oxygen electrocatalysis of manganese oxides have been reported in recent years,[20] few attempts have been made in relating the distinctive ORR of manganese oxides to the surface Mn density. Therefore, it is interesting to see if the surface Mn density can bridge the ORR understanding of the series of manganese oxides with different crystal structures. In addition, since there are no redox contributions from other transition metal elements, integrating the Mn redox responses (from which the Mn density can be determined) in manganese oxides becomes very easy. There are literature evidences indicating the underestimated role of surface Mn density in manganese oxides towards ORR.[20] As can be observed in Figure 8.3 a, the background CV loop (in Ar-saturated 0.1 M KOH electrolyte, dotted line) area of the various investigated manganese oxides increases in the sequence: δ-MnO_2, β-MnO_2, AMO, Ni/α-MnO_2, α-MnO_2-HT, α-MnO_2-SF.[20] The area of the background CV loop, to a large extent, reflects the integrated redox charges of Mn because the Mn redox happens within the investigated potential region. That is to say, roughly, the CV loop area in Figure 8.3 a can be positively related to the surface Mn density. Further observing the ORR polarization curves of the various manganese oxides displayed in Figure 8.3 b, a positive correlation between the ORR onset potential and the background CV loop area can be roughly established. Hence, it is very likely that the surface Mn density acts as an important dominating parameter for the ORR of manganese oxides with different crystal structures.

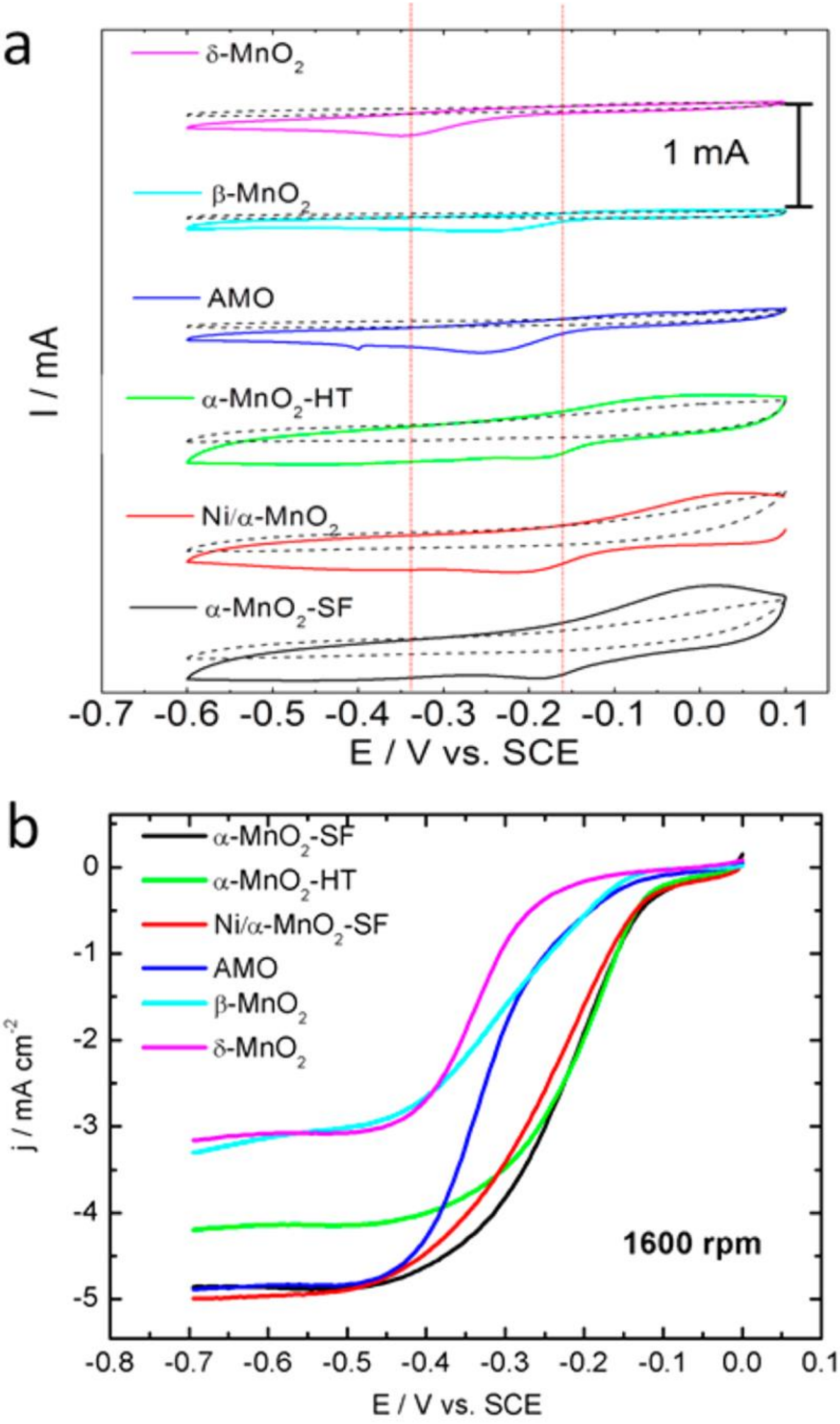

Figure 8.3 (a) CV curves of manganese oxides scanned in Ar-saturated (dotted line) and O_2-saturated (solid line) 0.1 M KOH at a scan rate of 20 mV s^{-1}. (b) ORR polarization curve of manganese oxides in O_2-saturated 0.1 M KOH at a rotating speed of 1600 rpm with a scan rate of 5 mV s^{-1}.[20]

A systematic study on the correlation between the surface Mn density and the ORR performance of different crystal structured-manganese oxides is recommended. The established recipes in literatures[19] could guide the synthesis of different type manganese oxide nanoparticles (e.g. β-MnO_2, R-MnO_2, α-MnO_2, δ-MnO_2, λ-MnO_2 and etc.).

Computational work revealing the reaction mechanism on spinel oxide is also recommended. Several questions remain to be answered. First, will the tetrahedral occupied TM cation changes it coordination to octahedral under OER conditions and actively participate in the OER? What might be the possible reaction pathway? In addition, for mix-metal spinel oxide (e.g. Mn-Co based spinel), will the exchange interaction between the Co and Mn center via the oxygen edges promote the reaction rate of ORR/OER? Is the dual-metal site mediated ORR or OER more thermodynamically favorable than the single metal site mediated mechanism? Our current analysis on the composition dependent ORR/OER by spinel $ZnCo_xMn_{2-x}O_4$, $ZnFe_xCo_{2-x}O_4$ and $Mn_xFe_{3-x}O_4$ nanoparticles consider one of the transition metal species (i.e. Mn or Co) as the leading active site, however, the potential synergy between the two metal centers during ORR/OER has not been investigated. Thus, the theoretical studies could help advance the comprehensive understanding of ORR/OER by spinel-typed oxide electrocatalysts.

The establishment of composition-structure-function correlation requires more extended efforts. The design of binary spinel oxides using combinations of redox inactive TM (Al, Zn, Mg and etc) and redox active TM (e.g. Ni, Co, Mn, Fe) is recommended. It has been reported that the introduction of redox inactive TM in oxide lattice sometimes significantly alters the electronic structure of active TM center.[21] Particularly, the redox position or redox features of oxides can be totally different with the introduction of redox inactive TM. In fact, the redox position is very important in electrocatalysis. This is because, in a single ORR or OER cycle, the TM center undergoes reversible oxidation and reduction. Correlation between the redox position and ORR/OER has also been established.[21] Therefore, it is interesting to see how the redox features of active metal can be tuned by the substitution level of redox inactive TM and how the redox features alters the catalytic activity.

8.3 Conclusion

The hypotheses in this thesis are adequately proven by the experimental design and the following statement explains how the outcomes are reflected in the original hypothesis. The hypothesis regarding the effects of transition metal geometry on oxygen electrocatalysis is proven by the design of spinel $CoAl_2O_4$ oxides electrocatalysts. The Co occupancy in octahedral sites is positively related to the OER activity, demonstrating that the octahedral site is more catalytically critical in spinel oxide. The identified Mn e_g filling and Co-O covalency in spinel $ZnCo_xMn_{2-x}O_4$ and $ZnFe_xCo_{2-x}O_4$ (x=0~2) oxides, respectively validated the hypothesis that there exists dominating physical principles governing the composition-dependent catalytic ORR/OER activity. The revealing of dominating surface chemistry in the ORR of manganese ferrite nanoparticles validate the hypothesis that the bulk descriptor is not applicable to nanoparticle system. The observed excellent cycling stability, well-reserved high-crystalline surface, and the computed downshifted O p-band relative the Fermi level of spinel $ZnFe_{0.4}Co_{1.6}O_4$ catalyst validate the hypothesis that lattice oxygen-mediated OER is not a favorable route for the cation-deficient spinel oxides.

References

[1] E. Lee, J.-H. Jang, Y.-U. Kwon, *J. Power Sources* **2015**, 273, 735-741.

[2] Y. Li, P. Hasin, Y. Wu, *Adv. Mater.* **2010**, 22, 1926-1929.

[3] C. Li, X. Han, F. Cheng, Y. Hu, C. Chen, J. Chen, *Nat. Commun.* **2015**, 6, 7345.

[4] H. Zhu, S. Zhang, Y.-X. Huang, L. Wu, S. Sun, *Nano Lett.* **2013**, 13, 2947-2951.

[5] X. Liu, Z. Chang, L. Luo, T. Xu, X. Lei, J. Liu, X. Sun, *Chem. Mater.* **2014**, 26, 1889-1895.

[6] K. A. Stoerzinger, M. Risch, B. Han, Y. Shao-Horn, *ACS Catal.* **2015**, 5, 6021-6031.

[7] F. Calle-Vallejo, O. A. Díaz-Morales, M. J. Kolb, M. T. M. Koper, *ACS Catal.* **2015**, 5, 869-873.

[8] C. Xiao, X. Lu, C. Zhao, *Chem. Commun.* **2014**, 50, 10122-10125.

[9] P. Bothra, S. K. Pati, *ACS Energy Lett.* **2016**, 1, 858-862.

[10] T. Maiyalagan, K. A. Jarvis, S. Therese, P. J. Ferreira, A. Manthiram, *Nat. Commun.* **2014**, 5, 1.

[11] M. N. Amini, H. Dixit, R. Saniz, D. Lamoen, B. Partoens, *Phys. Chem. Chem. Phys.* **2014**, 16, 2588-2596.

[12] D. N. Mueller, M. L. Machala, H. Bluhm, W. C. Chueh, *Nat Commun* **2015**, 6, 6097.

[13] C. Yang, A. Grimaud, *Catalysts* **2017**, 7, 149.

[14] A. Grimaud, O. Diaz-Morales, B. Han, W. T. Hong, Y.-L. Lee, L. Giordano, K. A. Stoerzinger, M. T. Koper, Y. Shao-Horn, *Nat. Chem.* **2017**, 9, 457-465.

[15] W. T. Hong, K. A. Stoerzinger, Y.-L. Lee, L. Giordano, A. Grimaud, A. M. Johnson, J. Hwang, E. J. Crumlin, W. Yang, Y. Shao-Horn, *Energy Environ. Sci.* **2017**, 10, 2190-2200.

[16] J. T. Mefford, X. Rong, A. M. Abakumov, W. G. Hardin, S. Dai, A. M. Kolpak, K. P. Johnston, K. J. Stevenson, *Nat Commun* **2016**, 7, 11053.

[17] C. Wei, Z. Feng, G. G. Scherer, J. Barber, Y. Shao-Horn, Z. J. Xu, *Adv. Mater.* **2017**.

[18] J.-P. Jacobs, A. Maltha, J. G. Reintjes, J. Drimal, V. Ponec, H. H. Brongersma, *Journal of Catalysis* **1994**, 147, 294-300.

[19] D. M. Robinson, Y. B. Go, M. Mui, G. Gardner, Z. Zhang, D. Mastrogiovanni, E. Garfunkel, J. Li, M. Greenblatt, G. C. Dismukes, *J. Am. Chem. Soc.* **2013**, 135, 3494-3501.

[20] Y. Meng, W. Song, H. Huang, Z. Ren, S.-Y. Chen, S. L. Suib, *J. Am. Chem. Soc.* **2014**, 136, 11452-11464.

[21] D. A. Kuznetsov, B. Han, Y. Yu, R. R. Rao, J. Hwang, Y. Román-Leshkov, Y. Shao-Horn, *Joule*. **2017**, 1-20.